Studies on the dependence of current-voltage characteristics on carrier concentration and granularity in several superconducting systems

Thesis Submitted for the Degree of

Doctor of Philosophy (Science) in Physics

of

Jadavpur University

By

Tasaul Sk

Under the supervision of

Prof. Ajay Kumar Ghosh

Department of Physics

Jadavpur University

Kolkata – 700 032, India

2023

যাদবপুর বিশ্ববিদ্যালয়
কলকাতা-৭০০০৩২, ভারত

* JADAVPUR UNIVERSITY
KOLKATA-700 032, INDIA

FACULTY OF SCIENCE: DEPARTMENT OF PHYSICS

Certificate from the Supervisor

This is to certify that the thesis entitled "**Studies on the dependence of current-voltage characteristics on carrier concentration and granularity in several superconducting systems**" submitted by Shri. **Tasaul Sk** who got his name registered on **20.09.2018** for the award of Ph.D. (Science) degree of Jadavpur University, is absolutely based upon his own work under the supervision of **Prof. Ajay Kumar Ghosh** and that neither this thesis nor any part of it has been submitted for either any degree/diploma or any other academic award anywhere before.

Ajay Kumar Ghosh
(Prof. Ajay Kumar Ghosh)
02/02/2023
Signature of Supervisor
with Date and Official Seal

Professor (Dr.) Ajay Kumar Ghosh
Department of Physics
Jadavpur University
Kolkata - 700032

*Established on and from 24th December, 1955 vide Notification No. 10986-Edn/IU-42/55 dated 6th December, 1955 under Jadavpur University Act, 1955
(West Bengal Act XXXIII of 1955) followed by Jadavpur University Act, 1981 (West Bengal Act XXIV of 1981)

ফোন: ০৩৩-২৪১৪-৬৬৬৬ Ext. ২৭৬১ Website: www.jadavpuruniversity.in
মো: +৯১-৯৮৩০৮৪৮৯২০
Phone: 033-2414-6666 Ext. 2761
M: +91-9830848920
Email: ajayk.ghosh@jadavpuruniversity.in

Acknowledgement

First of all, I would like to express my sincere gratitude with a deep sense of regard and respect to my supervisor ***Prof. Ajay Kumar Ghosh****,* ***Department of Physics****,* ***Jadavpur University*** *for giving me the golden opportunity to study on the field of* ***High-Temperature Superconductivity*** *and most grateful for his patience, motivation, enthusiasm and immense knowledge. His guidance and advice were immensely helpful through all the time of research and writing my thesis.*

I would like to give sincere thanks to the group members: ***Dr. S. Haldar, Dr. I. Mukherjee, Dr. S. Mollah****,* ***D. Rakshit, P. Das*** *and* ***P. Mandal*** *for their excellent co-operation, thoughtful discussions and support during the experiment in the laboratory. I wish to express my indebtedness to the members who accompanied me during the installation and training procedure of the newly installed* ***Vibrating Sample Magnetometer*** *(Cryogenics). I am also thankful to* ***Dr. B. Biswas, S. Roy, Ipsita Mukherjee*** *and* ***R. K. Saha*** *for providing me a friendly environment to work and for all the fun moments that we have had together in the last few years.*

I would also like to acknowledge the ***Council of Scientific & Industrial Research (CSIR) (CSIR File no.- 09/096(0853)/2016-EMR-I****), Govt. of India for awarding me the fellowship to carry out the research work.*

Finally, I wish to express my heartfelt gratitude to my parents, elder brother, sisters and other family members for their love, support, understanding, patience and encouragement in every possible way throughout this journey.

List of publications

Journals:

[1] **T. Sk**, Ajay Kumar Ghosh, J. Low Temp. Phys. **198** (2020) 224.

[2] **T. Sk**, Ajay Kumar Ghosh, AIP Adv. **10** (2020) 065117.

[3] **T. Sk**, D. Rakshit, Ajay Kumar Ghosh, Phys. Scr. **97** (2022) 025704.

[4] **T. Sk**, P. Mandal, D. Rakshit, Ajay Kumar Ghosh, Physica C **603** (2022) 1354152.

[5] **T.Sk,** P. Mandal, S. Haldar, Ajay Kumar Ghosh, Effectiveness of two pinning profiles in controlling magnetic critical current density in YBCO + YCMO composites (minor revision).

[6] I. Mukherjee, S. Mollah, **T. Sk**, S. Haldar, Ajay Kumar Ghosh, Physica C **560** (2019) 67.

[7] D. Rakshit, **T. Sk**, P. Das, S. Haldar, Ajay Kumar Ghosh, Physica C **588** (2021) 1353909.

[8] P. Mandal, D. Rakshit, **T. Sk**, Ajay Kumar Ghosh, J. Supercond. Nov. Magn. **35** (2022) 1079.

[9] P. Mandal, D. Rakshit, I. Mukherjee, **T. Sk**, Ajay Kumar Ghosh, Phys. Lett. A **436** (2022) 128072.

[10] D. Rakshit, P. Mandal, **T. Sk**, Ajay Kumar Ghosh, J. Supercond. Nov. Magn. **35** (2022) 1421.

[11] P. Das, **T. Sk**, Ajay Kumar Ghosh, J. Supercond. Nov. Magn. **35** (2022) 3477.

[12] S. Mollah, P. Mandal, **T. Sk**, S. Haldar, Ajay Kumar Ghosh, AIP Conf. Proc. **2220** (2020) 110044.

[13] P. Mandal, D. Rakshit, **T. Sk**, Ajay Kumar Ghosh, Insulating nanoparticle induced pinning in YBCO superconductor: crossover from collective to strong pinning regimes (submitted).

[14] P. Mandal, S. Mollah, D. Rakshit, I. Mukherjee, **T. Sk**, Ajay Kumar Ghosh, Vortex pinning, equilibrium magnetization, and pairing symmetry in BPBO superconductor (submitted).

[15] **T. Sk**, Ajay Kumar Ghosh, Localization length of a composite system consisting of GBCO and GCMO, Accepted by ICCM-21, October 28, 2021, The Academy of Sciences, Chennai.

Conferences:

[1] **T. Sk**, Shaping the Future of Indian Power Sector Through Renewable Energy, Department of Power Engineering, Jadavpur University, Kolkata 700032, India; September 09-10, 2016.

[2] **T. Sk**, Twists and Turns in Physics Research: Special Emphasis on Condensed Matter and Biophysics (TTPR-2017); Department of Physics, Jadavpur University, Kolkata 700032, India; February 21-22, 2017.

[3] **T. Sk**, Recent Trend in Frontier Research in Physics, Jadavpur University, Kolkata 700032, India; March 06, 2018.

[4] **T. Sk**, Condensed Matter Days-2018, Department of Physics, University of Burdwan, Burdwan-713104, India; August 29-31, 2018.

[5] **T. Sk**, P. Das, S. Haldar, Ajay Kumar Ghosh, 3rd International Conference on Condensed Matter & Applied Physics (ICC 2019), Department of physics, Govt. Engineering College, Bikaner, Rajasthan, India; October 14-15, 2019.

[6] **T. Sk,** Ajay Kumar Ghosh, International Conference on Condensed Matter (ICCM-21), The Academy of Sciences, Chennai, India; October 28-30, 2021 in Virtual mode.

[7] B. Biswas, I. Mukherjee, P. Das, **T. Sk**, L. Ghosh, S. Mollah, S. Haldar, Ajay Kumar Ghosh, Twists and Turns in Physics Research: Special Emphasis on Condensed Matter and Biophysics (TTPR-2017), Department of Physics, Jadavpur University, Kolkata 700032, India; February 21-22, 2017.

[8] S. Mollah, B. Biswas, **T. Sk**, I. Mukherjee, S. Haldar, Ajay Kumar Ghosh, Condensed Matter Days-2017, Department of Physics, Tezpur University, Tezpur 784028, Assam, India; August 29-31, 2017.

[9] I. Mukherjee, **T. Sk**, S. Mollah, Ajay Kumar Ghosh, Condensed Matter Days-2018, Department of Physics, University of Burdwan, Burdwan-713104, India; August 29-31, 2018.

[10] P. Das, S. Haldar, **T. Sk**, Ajay Kumar Ghosh, Third International Conference on Advanced Materials (ICAM-2019), International Unit on Molecular Science and Engineering (IUMSE), Mahatma Gandhi University, Priyadharshini Hills, P.O. Kottayam, Kerala 686560, India; August 09-11, 2019.

[11] P. Mandal, D. Rakshit, I. Mukherjee, **T. Sk**, Ajay Kumar Ghosh, The Twenty-Eighth National Symposium on Cryogenics and Superconductivity (NSCS28); Cryogenics Engineering Centre, Indian Institute of Technology Kharagpur, Kharagpur-721302, India; October 18-21, 2022.

[12] D. Rakshit, P. Mandal, **T. Sk**, Ajay Kumar Ghosh, The Twenty-Eighth National Symposium on Cryogenics and Superconductivity (NSCS28); Cryogenics Engineering Centre, Indian Institute of Technology Kharagpur, Kharagpur-721302, India; October 18-21, 2022.

Contents

Chapter 1

Introduction

1.1 Introduction

Current-voltage (*IV*) method has been very successful for the detection of the vortex phase transitions in high temperature superconductors (HTS) **[1-5]**. A very common complexity in the area of the pinning of vortices is the clear determination of the phase boundary between two different vortex states **[6-8]**. Once we can determine the nature of the vortex state and phase boundary, finding out possible ways of enhancing the critical current density (J_c) and upper critical field (H_{c2}) becomes much easier in the HTS **[9-12]**. Among several states of vortices existing in nature the vortex states suggested by Berezinskii-Kosterlitz-Thousless (BKT) **[13-15]** at zero applied magnetic field condition in several materials including the HTS is well known in the area of the research on vortex states. In addition to that of the Abrikosov vortices observed in the applied field it is really very important to study BKT states comprising of vortex-antivortex pairs and unbinding at higher temperature (T) in several superconducting systems.

Considering the complexity of the exiting problems, several superconducting systems need to be included for the understanding of several aspects of vortex states and enhancing superconducting properties.

The BKT transition is originally formulated within the context of the 2D XY model **[13-16]**. It depends on the fact that in such a system, the interaction energy between vortex-antivortex pairs is a logarithmic function of the separation. According to the BKT theory, there is a thermodynamic instability in which vortex - antivortex pairs that are bound at low temperature unbound at a characteristic temperature, T_{BKT} in two dimensional (2D) neutral superfluid. The associated phase transition is known as the BKT transition. Even though initially the BKT transition was proposed for spin systems, it has been extended to apply for understanding the superconducting systems. The applicability of the BKT theory was first detected in superconducting films **[17, 18]**.

The BKT transitions have been detected experimentally in several systems, such as (i) trapped 2D Bose gases, (ii) liquid helium films, (iii) 2D atomic hydrogen, and (iv) superconducting Josephson junctions **[19-22]**. There are several experimental techniques to detect the signature of this topological phase transition at a temperature, $T = T_{BKT}$ **[23]**. The nonlinear nature of *IV*

characteristics below the superconducting transition temperature, T_c, is used to detect the BKT transition in superconducting systems. The nonlinear to a linear transformation of *IV* of an anisotropic superconducting system can be used to determine the BKT phase transition temperature. Below T_c, the BKT phase transition is detected by using the variation of an exponent η as a function of *T*. Following the equation for the voltage drop as given below,

$$V = aI^{\eta} \qquad (\mathbf{1.1})$$

the determination of η is possible where *a* is constant **[13, 14, 24]**. The exponent η is a measure of the nonlinearity of *IV* curves. An abrupt change in η (*T*) is observed at T_{BKT}. The BKT transition is generally detected with the change in η (*T*) from 3.0 to 1.0 **[25-27]**. At $T = T_{BKT}$, $\eta = 1$ *IV* curves are linear in nature. Within the BKT scenario, the transition of the vortex-antivortex bound pairs to the unbound state is driven by thermal energy **[28]**.

The superfluid density, σ_s is proportional to the squared amplitude of the macroscopic wave function and therefore describes the superconducting charge carrier. It is thus a fundamental parameter whose variation as a function of doping provides important information about the superconducting state. Generally, the σ_s is directly proportional to J_s, the superfluid phase stiffness (SPS) **[29]**. In a conventional 3D superconductor, the SPS goes to zero at T_c. A universal relation is observed between the superconducting transition temperature, $T_{c,}$ and $\sigma_s(0)$,

suggested by Uemera et al. [30-32]. Determining the fluctuation of σ_s as a function of T is achievable by measuring the transport characteristics in a superconducting system [33, 34]. Nonlinear *IV* characteristics are used to extract the exponent η. The determination of the SPS, J_s has been done by using η by following Ambegaokar-Halperin-Nelson-Siggia (AHNS) theory [35-37] and is defined by the equation

$$J_s = (\eta - 1)T/\pi \qquad \textbf{(1.2)}$$

The dependence of the σ_s on the doping level has been studied in several superconducting systems [38-40]. In undoped Bi-2212 systems, σ_s has been studied by using the finest controlling in doping level [41]. A suppression of the SPS has been observed in several cuprate superconducting systems [42-44]. Even though the relation between T_c and σ_s has been investigated widely it is mostly unknown how the SPS can be controlled and how it affects other superconducting properties, including magnetic critical current density (J_{cm}) and vortex pinning in several superconducting systems.

1.2 Superconducting systems for present research

We have chosen several HTS systems, which are mostly layered 2D structure for *IV* measurements and BKT studies. Firstly, we briefly discuss the typical structure of unit cell of the HTS samples used for the present thesis. A typical structure of

unit cell of $YBa_2Cu_3O_{7-\delta}$ (YBCO) is shown in **Figure 1.1**. Two CuO_2 planes separated by Cu-O chains. The typical lattice parameters of an orthorhombic YBCO are a =3.82 Å, b = 3.89 Å and c = 11.68 Å. The unit cell contains a layer

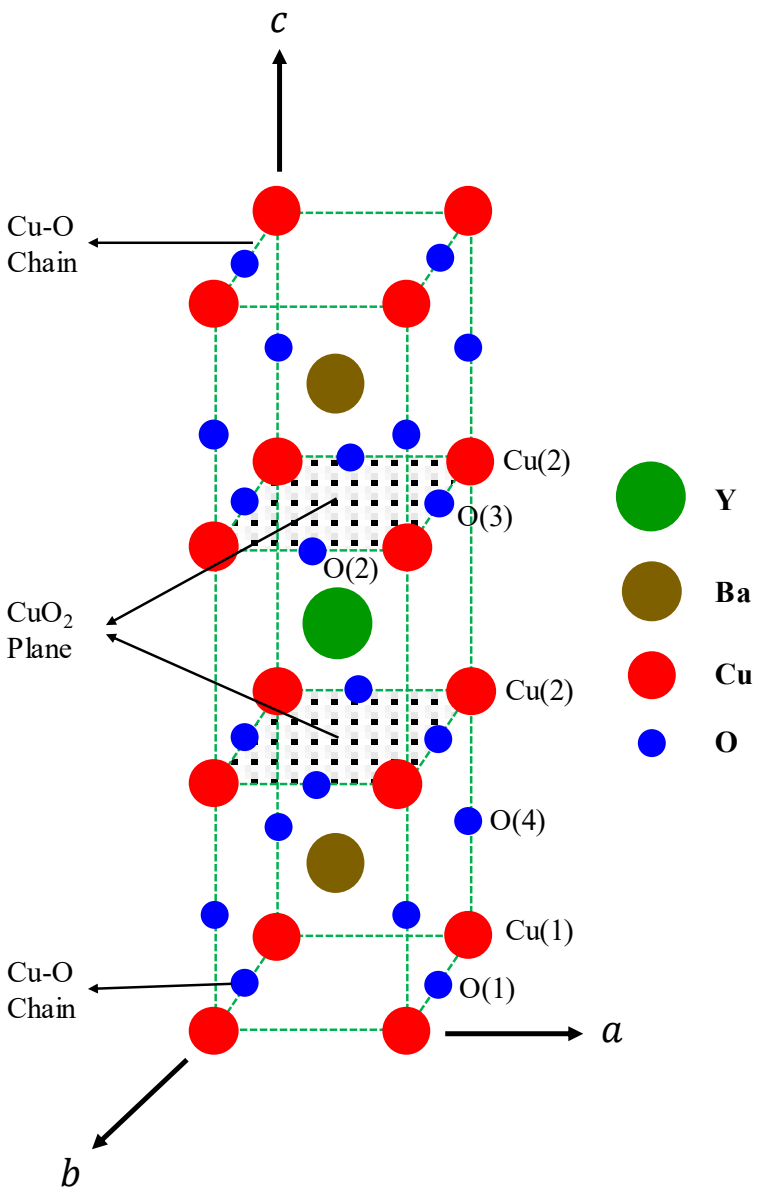

Figure 1.1: Unit cell structure of $YBa_2Cu_3O_{7-\delta}$.

of Cu-O having Cu(1) surrounded by four oxygen ions and a layer of Cu-O, where Cu(2) is surrounded by five oxygen ions forming a polyhedron. Chains of Cu-O

are parallel to the CuO_2 layers with barium atoms located between the planes and chain. In layered structure, the superconducting pairs are formed in CuO_2 layers, and the associated phase angles are important for the formation of the BKT states in HTS. However, other layers participate in coupling between superconducting layers and hence affecting *IV* and other transport properties and magnetic properties. The positions of oxygen O(2) and O(3), are also very important because we know that varying the excess content, δ tuning of the pairing formation, T_c and other superconducting properties can be altered **[45, 46]**.

1.3 Aims and Objectives

The presence of different vortex phases described in the framework of the BKT and Abrikosov (A) affects several properties in different ways and magnitudes in a superconducting system. Vortices generated by thermal fluctuations control both the transport and magnetic properties in superconductors with even strong pinning. Depending on the superconducting system, we may control the *IV* characteristics. We will explore several such superconducting systems in which the vortex phases can be controlled differently. In the present thesis, we have investigated how controlling vortices from two different regions, the *IV* and related features can be altered. The nonlinear variation of *IV* characteristics in superconducting systems is related to the phase transition in vortex configuration.

We shall study controlling vortices both from the lattice sites and inter-granular sites in superconductors. We have chosen several superconducting systems for having several types of vortices below T_c. In the inter-granular sites compound having magnetic control over the vortices has been chosen. In addition, the usual change in carrier doping level has been used. Superconducting samples with a wide range of pinning strengths have been synthesized and characterized. An understanding of the vortex phase (Abrikosov) diagram and how the pinning scenario in superconductors exhibiting nonlinear *IV* at the zero magnetic fields (BKT) affects magnetic critical current density, J_{cm} is an important direction of research to correlate transport and magnetic properties. Enhancing J_{cm} is the most important aspect in the area of HTS. We have also made an attempt to study the J_{cm} of several such systems in which the nonlinear *IV* characteristics have been observed.

We have selected several high T_c superconducting systems in which the SPS vortex phases can be controlled in different ways. We have chosen several systems in which vortices are controlled both from the lattice site by (i) changing carrier concentration and (ii) the inter-granular site by changing granularity and inter-granular linking. Several superconducting systems have been selected as representatives of ways of controlling *IV* as well as vortex pinning. Tuning the nonlinearity in *IV* through changes in the lattice site and to investigate the possibility of BKT phase transition and the nature of variation of the SPS, we

have chosen several Ce substituted $Y_{1-x}Ce_xBa_2Cu_3O_{7-\delta}$ (with x = 0.0 to 0.4) superconductor **[47]**. An important question is how to control nonlinearity in *IV* in such layered superconducting systems. It is also very important to understand how the nonlinear behaviour changes using the inter-granular network. We have used magnetic structure in the inter-granular network region to tune the nonlinearity in *IV* and are interested to understand the behaviour of the superfluid **[48]**. We have selected several pure and composite samples by varying δ. We have used a low concentration of 5% Y_2CoMnO_6 as a magnetic material for making the inter-granular network **[49]**. In the presence of non-magnetic impurity, how the *T* dependence of the SPS is affected is to be investigated by using *IV* at the zero magnetic fields. It will be very important to understand how nonmagnetic dopant affects the pinning of the pancake vortices in Bi-2212 superconductor **[50]**. So, we have selected several bulk Zn-doped $Bi_2Sr_2CaCu_{2-x}Zn_xO_{8+\delta}$ (Bi-2212) superconductors for x = 0.0 to 0.2. Below we have outlined the research done in the present thesis in the aforementioned direction.

1.4 Outline of the thesis

In the present thesis, we have explained several experimental works, including the synthesis and characterization of superconducting samples in **Chapter 2**. In **Chapter 3** we have studied temperature variation of the SPS and the possibility of BKT transition have been explored in several bulk Ce doped YBCO

superconductor samples. How the magnetic structure in the inter-granular network in the bulk sample influences the nonlinear nature of *IV* characteristics and how superfluid behaviour is affected as a result of the inclusion of this component in several bulk YBCO superconducting samples, have been explained in **Chapter 4**. Detection of the BKT transition have also been discussed in this Chapter. Suppression of the SPS in the presence of nonmagnetic Zn replacing Cu in Bi-2212 system have determined using the AHNS theory in **Chapter 5**. A scaling between SPS and critical temperature have also been established in this Chapter. How nonmagnetic dopants (Zn in Cu site) affect the pinning of pancake vortices in Bi-2212 superconductor have explained in **Chapter 6**. In this Chapter, we have analysed J_{cm} by $M(H)$ measurement of nonmagnetic Zn- doped Bi-2212 superconductor to understand the macroscopic nature of vortex pinning. Shifting in the irreversibility line (IL) and change in pinning force density in the doped Bi-2212 sample have also been determined. The impacts of two different types of pinning centres on magnetization and J_{cm} of YBCO superconductors have been discussed in **Chapter 7**.

1.5 References

[1] M. Buchacek, Z. L. Xiao, S. Dutta, E. Y. Andrei, P. Raychaudhuri, V. B. Geshkenbein, G. Blatter, Phys. Rev. B **100** (2019) 224502.

[2] H. J. Jensen, A. Brass, Y. Brechet, A. J. Berlinsky, Phys. Rev. B **38** (1988) 9235.

[3] D. Goldschmidt, Phys. Rev. B **39** (1989) 9139.

[4] M. T. González, S. R. Currás, J. Maza, F. Vidal, Phys. Rev. B **63** (2001) 224511.

[5] G. Balestrino, A. Crisan, D. V. Livanov, E. Milani, M. Montuori, A. A. Varlamov, Phys. Rev. B **51** (1995) 9100.

[6] J. M. Huijbregtse, B. Dam, R. C. F. van der Geest, F. C. Klaassen, R. Elberse, J. H. Rector, R. Griessen, Phys. Rev. B **62** (2000) 1338.

[7] S. B. Field, S. S. James, J. Barentine, V. Metlushko, G. Crabtree, H. Shtrikman, B. Ilic, S. R. J. Brueck, Phys. Rev. Lett. **88** (2002) 067003.

[8] M. Z. Cieplak, Z. Adamus, M. Konczykowski, L.Y. Zhu, X. M. Cheng, C. L. Chien Phys. Rev. B **87** (2013) 014519.

[9] M. Miura, B. Maiorov, S. A. Baily, N. Haberkorn, J. O. Willis, K. Marken, T. Izumi, Y. Shiohara, L. Civale, Phys. Rev. B **83** (2011) 184519.

[10] J.Y. Lin, M. Gurvitch, S. K. Tolpygo, A. Bourdillon, S. Y. Hou and Julia M. Phillips, Phys. Rev. B **54** (1996) 12717 (R).

[11] E. Mezzetti, S. Colombo, R. Gerbaldo, G. Ghigo, L. Gozzelino, B. Minetti, R. Cherubini, Phys. Rev. B **54** (1996) 3633.

[12] B. J. Ramshaw, James Day, Baptiste Vignolle, David LeBoeuf, P. Dosanjh, Cyril Proust, Louis Taillefer, Ruixing Liang, W. N. Hardy, D. A. Bonn, Phys. Rev. B **86** (2012) 174501.

[13] J. M. Kosterlitz, D. J. Thouless, J. Phys. C **6** (1973) 1181.

[14] V. L. Berezinskii, Zh. Eksp. Teor. Fiz **61** (1971) 1144.

[15] J. M. Kosterlitz, D. J. Thouless, J. Phys. C **5** (1972) L124.

[16] I. Maccari, L. Benfatto, C. Castellani, Phys. Rev. B **96** (2017) 060508 (R).

[17] M. R. Beasley, J. E. Mooji, T. P. Orlando, Phys. Rev. lett. **42** (1979) 1165.

[18] D. H. Kim, A. M. Goldman, J. H. Kang, R. T. Kampwirth, Phys. Rev. B **40** (1989) 8834.

[19] D. J. Bishop, J. D. Reppy, Phys. Rev. Lett. **40** (1978) 1727.

[20] D. J. Resnick, J. C. Garland, J. T. Boyd, S. Shoemaker, R. S. Newrock, Phys. Rev. Lett. **47** (1981) 1542.

[21] A. I. Safonov, S. A. Vasilyev, I. S. Yasnikov, I. I. Lukashevich, S. Jaakkola, Phys. Rev. Lett. **81** (1998) 4545.

[22] T. V. Sukhareva, V. A. Finkel, Low Temp. Phys. **44** (2018) 194.

[23] P. Minnhagen, Rev. Mod. Phys. **59** (1987) 1001.

[24] L. Benfatto, C. Castellani, T. Giamarchi, Phys. Rev. B **80** (2009) 214506.

[25] B. I. Halperin, D. R. Nelson, J. Low Temp. Phys. **36** (1979) 599.

[26] V. I. Nizhankovskiy, K. Rogacki, Phys. Rev. B **100** (2019) 104510.

[27] L. Miu, D. Miu, G. Jakob, H. Adrian, Phys. Rev. B **73** (2006) 224526.

[28] D. R. Nelson and J. M. Kosterlitz, Phys. Rev. Lett. **39** (1977) 1201.

[29] J. L. Tallon, J. W. Loram, J. R. Cooper, C. Panagopoulos, C. Bernhard, Phys. Rev. B **68** (2003) 180501(R).

[30] Y. J. Uemura, G. M. Luke, B. J. Sternlieb, J. H. Brewer, J. F. Carolan, W. N. Hardy, R. Kadono, J. R. Kempton, R. F. Kiefl, S. R. Kreitzman, P. Mulhern, T. M. Riseman, D. Ll. Williams, B. X. Yang, S. Uchida, H. Takagi, J. Gopalakrishnan, A. W. Sleight, M. A. Subramanian, C. L. Chien, M. Z. Cieplak, G. Xiao, V. Y. Lee, B. W. Statt, C. E. Stronach, W. J. Kossler and X. H. Yu, Phys. Rev. Lett. **62** (1989) 2317.

[31] Y. J. Uemura, A. Keren, L. P. Le, G. M. Luke, W. D. Wu, Y. Kubo, T. Manako, Y. Shimakawa, M. Subramanian, J. L. Cobb, and J. T. Markert, Nature **364** (1993) 605.

[32] Y. Zuev, M. S. Kim, T. R. Lemberger, Phys. Rev. Lett. **95** (2005) 137002.

[33] I. Božović, X. He, J. Wu, A. T. Bollinger, Nature **536** (2016) 309.

[34] I. Hetel, T. R. Lemberger, M. Randeria, Nature **3** (2007) 400.

[35] V. Ambegaokar, H. Halperin, D. Nelson, E. Siggia, Phys. Rev. Lett. **40** (1978) 783.

[36] V. Ambegaokar, H. Halperin, D. Nelson, E. Siggia, Phys. Rev. B **21** (1980) 1806.

[37] P. Das, Studies of superfluid stiffness in anisotropic superconductors and randomness in the coupling of superconducting planes, Thesis submitted for Ph.D. (Sc.), Jadavpur University (2022).

[38] S. Steers,T. R. Lemberger, J. Draskovic, Phys. Rev. B **94** (2016) 094525.

[39] C. Panagopoulos, B. D. Rainford, J. R. Cooper, W. Lo, J. L. Tallon, J. W. Loram, J. W. Loram, Y. S. Wang, C. W. Chu, Phys. Rev. B **60** (1999) 14617.

[40] N. R. Lee-Hone, J. S. Dodge, D. M. Broun1, Phys Rev. B **96** (2017) 024501.

[41] J. Yong, M. J. Hinton, A. McCray, M. Randeria, M. Naamneh, A. Kanigel, T. R. Lemberger, Phys. Rev. B **85** (2012) 180507.

[42] M. V. Feigel'man, L. B. Ioffe, Phys. Rev. B **92** (2015) 100509 (R).

[43] U. Erdenemunkh, B. Koopman, L. Fu, K. Chatterjee, W. D. Wise, G. D. Gu, E. W. Hudson, M. C. Boyer, Phys. Rev. Lett. **117** (2016) 257003.

[44] T. Sk, D. Rakshit, A. K. Ghosh, Phys. Scr. **97** (2022) 025704.

[45] J. D. Jorgensen, B. W. Veal, A. P. Paulikas, L. J. Nowicki, G. W. Crabtree, H. Claus, W. K. Kwok, Phys. Rev. B **41** (1990) 1863.

[46] J. D. Jorgensen, M. A. Beno, D. G. Hinks, L. Soderholm, K. J. Volin, R. L. Hitterman, J. D. Grace, I. K. Schuller, Phys. Rev. B **36** (1987) 3608.

[47] T. Sk, A. K. Ghosh, AIP Adv. **10** (2020) 065117.

[48] T. Sk, A. K. Ghosh, J. Low Temp. Phys. **198** (2020) 224.

[49] J. Blasco, J. García, G. Subías, J. Stankiewicz, J. A. Rodríguez-Velamazán, C. Ritter, J. L. García-Muñoz, F. Fauth, Phys. Rev. B **93** (2016) 214401.

[50] T. Sk, P. Mandal, D. Rakshit, A. K. Ghosh, Physica C **603** (2022) 1354152.

Chapter 2

Experimental methods

2.1 Introduction

In this chapter, we have discussed the general experimental techniques that we have used. We have used the conventional solid state reaction method to synthesize superconducting samples. Details of the synthesis procedures have been given separately. We have characterized all the samples by using (i) X-ray diffraction (XRD) method (Bruker D8 advanced X-ray diffractometer) (ii) Field emission scanning electron microscope, FESEM, (INSPECT F50). Transport measurements have been carried out using the standard four-probe technique. A vibrating sample magnetometer, VSM (Cryogenics, UK), has been used for all magnetization measurements. In this Chapter, we have briefly discussed the working principle of XRD, FESEM, VSM, and other experimental procedures.

2.2 Sample Synthesis

The synthesis route has a significant role in producing good quality bulk polycrystalline superconducting samples. Sample characteristics like phase formation, grain growth, and grain connectivity depend on synthesis conditions. There are several methods to synthesize polycrystalline cuprate superconductors, like the solid-state reaction method **[1-3]**, the sol-gel method **[4, 5]**, coprecipitation method **[6, 7]**. The solid-state method involving mixing, calcination, and sintering is the most widely used to synthesize polycrystalline bulk superconducting samples.

In the present work, we have synthesized series of several superconducting samples. The compositions of the synthesized samples with labelling are given in **Table 2.1**. To synthesize **Series I** and **Series II,** highly pure powders of Y_2O_3, $BaCO_3$, CuO, CeO_2 (for Ce doped) have been used with proper stoichiometry. For **Series III,** we have used Bi_2O_3, $SrCO_3$, $CaCO_3$, CuO, ZnO_2 (for Zn-doped). Firstly, we have taken the starting chemicals in a proper stoichiometric ratio. Then powders have been mixed and ground thoroughly using agate mortar and pestle for more than 3 hours to get better homogeneity. The mixed powder has been pressed into pellets (diameter typically 8.0 mm and thickness ~0.5-1.0 mm) using dice and a high-pressure hydraulic press. The pellets have been calcined in

Series I:

(i) $YBa_2Cu_3O_{6.9}$(**S1**)

(ii) $Y_{0.9}Ce_{0.1}Ba_2Cu_3O_{6.9}$(**S2**)

(iii) $Y_{0.85}Ce_{0.15}Ba_2Cu_3O_{6.9}$(**S3**)

(iv)$Y_{0.8}Ce_{0.2}Ba_2Cu_3O_{6.9}$(**S4**)

(v) $Y_{0.75}Ce_{0.25}Ba_2Cu_3O_{6.9}$(**S5**)

(vi) $Y_{0.7}Ce_{0.3}Ba_2Cu_3O_{6.9}$(**S6**)

(vii) $Y_{0.65}Ce_{0.35}Ba_2Cu_3O_{6.9}$(**S7**)

(viii) $Y_{0.6}Ce_{0.4}Ba_2Cu_3O_{6.9}$(**S8**)

Series II:

Pure samples:

(i) $YBa_2Cu_3O_{7.0}$(**S9**)

(ii) $YBa_2Cu_3O_{6.9}$(**S10**)

(iii) $YBa_2Cu_3O_{6.7}$(**S11**)

(iv) $YBa_2Cu_3O_{6.5}$(**S12**)

Mixed samples:

(v) $YBa_2Cu_3O_{7.0}$+5%Y_2CoMnO_6(**S13**)

(vi) $YBa_2Cu_3O_{6.9}$+5%Y_2CoMnO_6(**S14**)

(vii) $YBa_2Cu_3O_{6.7}$+5%Y_2CoMnO_6(**S15**)

(viii) $YBa_2Cu_3O_{6.5}$+5%Y_2CoMnO_6(**S16**)

Series III:

(i) $Bi_2Sr_2CaCu_2O_{8+\delta}$(**S17**)

(ii) $Bi_2Sr_2CaCu_{1.95}Zn_{0.05}O_{8+\delta}$(**S18**)

(iii) $Bi_2Sr_2CaCu_{1.9}Zn_{0.1}O_{8+\delta}$ (**S19**)

(iv) $Bi_2Sr_2CaCu_{1.85}Zn_{0.15}O_{8+\delta}$(**S20**)

(v) $Bi_2Sr_2CaCu_{1.8}Zn_{0.2}O_{8+\delta}$(**S21**)

Table 2.1: Synthesized samples series with labelling.

a tube furnace at different temperatures for 24 hours. Typical calcination temperatures are (i) 850 ºC for **Series I** and **II** and (ii) 780 ºC for **Series III**. All the samples have been sintered at different temperatures with intermediate grindings and pelletizations. We have used (i) 930 ºC, 935 ºC and 940 ºC for 24 hours each to sinter **Series I** and **II**, (ii) 820 ºC, 830 ºC, 840 ºC for 36, 48, and 60 hours respectively to sinter **Series III**. Prior to mixing with **Series II**, Y_2CoMnO_6 has been synthesized separately using the standard solid state reaction method, and the sintering temperature has been used at 1250 ºC for 48h. All the samples (**Series I**, **II** and **III**) have been annealed at 450 ºC in flowing oxygen for 24-48 hours to stabilize the oxygen stoichiometry.

2.3 X-Ray Diffraction (XRD)

X-ray diffraction (XRD) is widely used for the structural characterization of crystalline materials **[8]**. This method is also used for phase identification and can provide information on unit cell dimensions **[9−11]**. The working principle of XRD is based on constructive interference of monochromatic X-rays and a crystalline sample. These X-rays are generated by a cathode ray tube. The rays are filtered to produce monochromatic radiation, collimated to concentrate, and directed toward the sample. The interaction of the incident rays with the sample produces constructive interference when the condition satisfies Bragg's law

$$2d_{hkl}\sin\theta = n\lambda \qquad \textbf{(2.1)}$$

Here d_{hkl} is the interplanar separation between the planes having Miller Indices (*hkl*) **[12, 13]**. θ is the angle of the incident beams with the planes (*hkl*), λ is the wavelength of the used X-ray, and *n*-denotes the order of diffraction maxima. The Bragg's law relates the wavelength of electromagnetic radiation to the diffraction angle and the lattice spacing in a crystalline sample. **Figure 2.1** shows the schematic diagram of Braggs diffraction of a crystalline sample. The diffracted X-rays are detected, processed, and counted. The detector counts no. of X-ray pulses as a function of angle 2θ.

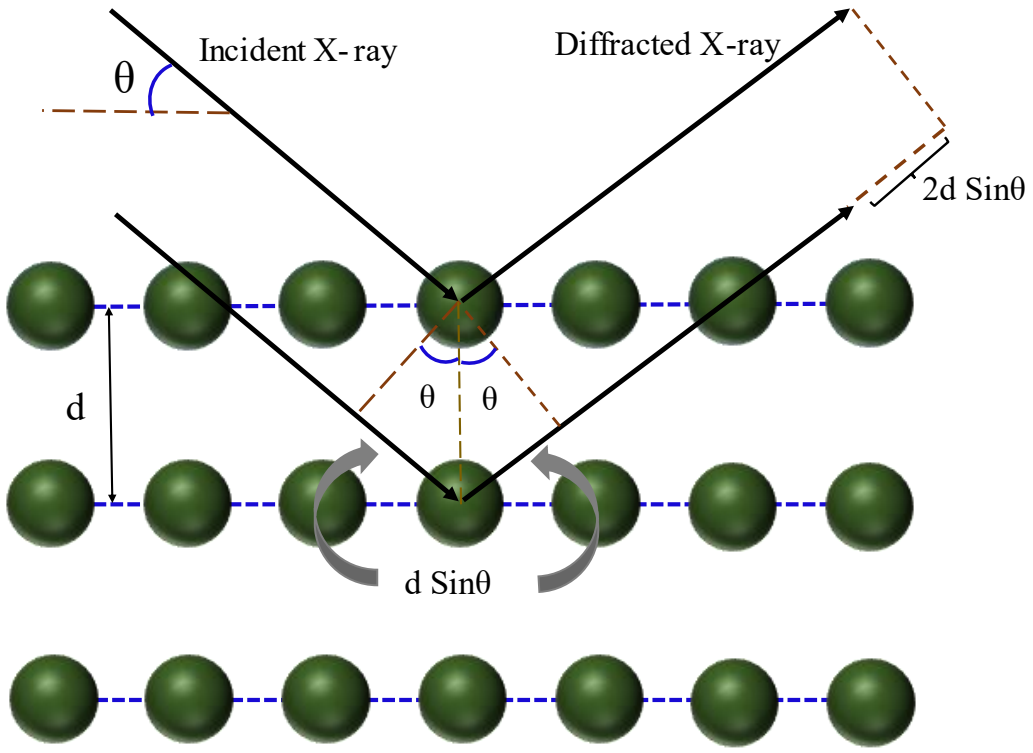

Figure 2.1: Schematic diagram of Bragg's diffraction of the crystalline sample.

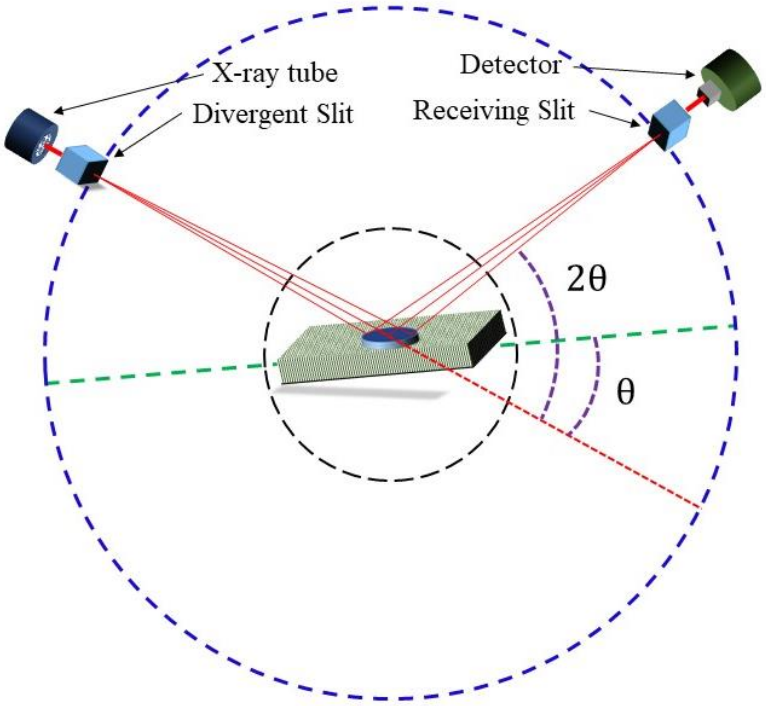

Figure 2.2: Schematic diagram of X-ray diffractometer.

The Bragg-Brentano geometry **[14]** is commonly followed in most diffractometer setups. A schematic diagram of the X-ray diffractometer is shown in **Figure 2.2**. X-ray diffractometer consists of three essential elements: an X-ray tube, a sample holder, and an X-ray detector. X-rays are generated in a cathode ray tube by heating a filament to produce electrons. These electrons are accelerated toward the target by applying a voltage. After bombarding the target materials with electrons, the characteristics of X-ray spectra are produced. These spectra consist of several components. Copper (Cu) is used as the most common target material. In most cases, Cu-K_α wavelength (λ = 1.5406 Å) is used in an X-ray diffractometer. These X-rays are collimated and directed onto the sample.

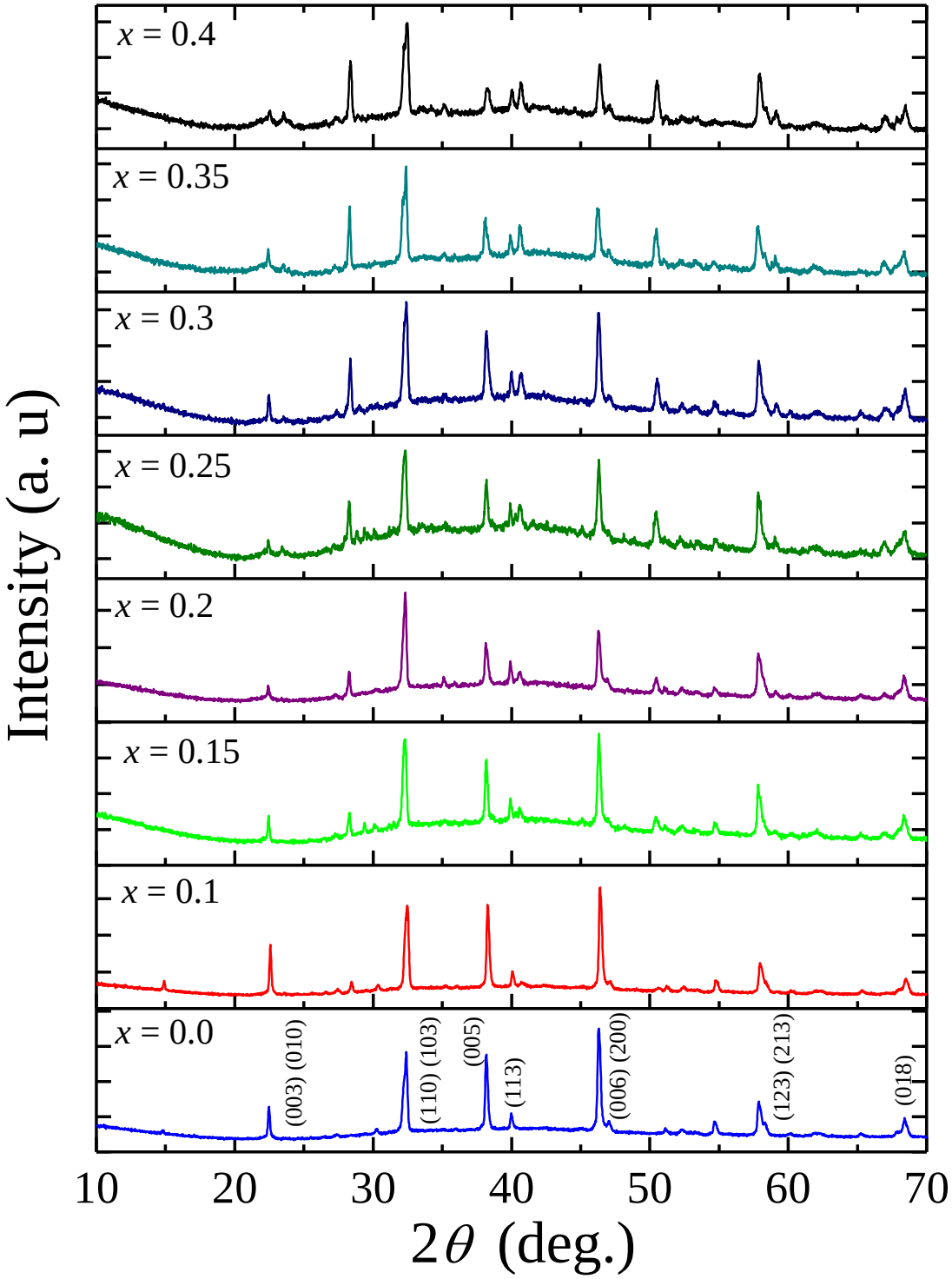

Figure 2.3: Representative X-ray diffraction patterns of $Y_{1-x}Ce_xBa_2CuO_{6.9}$ corresponding to x = 0 (**S1**), 0.1 (**S2**), 0.15 (**S3**), 0.2 (**S4**), 0.25 (**S5**), 0.3 (**S6**), 0.35 (**S7**) and 0.4 (**S8**).

While measuring XRD patterns, both the sample holder and detector are rotated. The geometry of an X-ray diffractometer is such that the sample rotates by an angle θ with respect to the collimated X-ray beams while the detector rotates by an angle 2θ. We have measured XRD data by varying 2θ from 10º to 70º. We have used a scan speed of 0.6 sec/step and a step size of 0.02º. Scan speed is the hold time at each 2θ value set as per the requirement of a fast or slow scan. During measurement, voltage and current have been kept at 35.0 kV and 35.0 mA.

The results of the X-ray diffraction are the intensity of the signal for various angles of diffraction at their respective 2θ position. The intensity of the peaks is related to the number of molecules in that phase or with that spacing. We can determine the space group, unit cell, and lattice constants by identifying *hkl* plane from the corresponding peak position **[15, 16]**. In **Figure 2.3** we have shown representative XRD patterns of $Y_{1-x}Ce_xBa_2CuO_{6.9}$ corresponding to $x = 0$ (**S1**), 0.1 (**S2**), 0.15 (**S3**), 0.2 (**S4**), 0.25 (**S5**), 0.3 (**S6**), 0.35 (**S7**) and 0.4 (**S8**). Indexing all major peaks that correspond to YBCO structure. No structural changes have been observed due to doping at the rare earth site.

2.4 Field Emission Scanning Electron Microscopy (FESEM)

There are two types of electron microscopes, Scanning electron microscope (SEM), and Transmission electron microscope (TEM). SEM is one of the most widely used instrumental methods for examining and analyzing the distribution of the micro and nanoparticle of solid specimens. One of the reasons that SEM is preferred for particle size analysis is due to its resolution of 10 nm. SEM is mainly used to examine surface topology, morphology, and composition **[17-19]**. The main components of the SEM are an electron source, condenser lenses, scanning coil, objective lens, sample chamber and stage, detector, and operating computers. A stable power supply, vacuum, cooling system, and vibration free space are the basic requirements of the SEM. A schematic diagram of the main parts of a SEM is shown in **Figure 2.4**. The main difference between SEM and FESEM is the type of electron source. The working principles of different components of FESEM are described in the following section.

Electron source: In a standard electron microscope, electrons are produced by a crystal of lanthanum hexaboride (LaB_6) that is mounted on a tungsten filament. In FESEM, an extremely thin and sharp tungsten needle (tip diameter 10^{-7} – 10^{-8} m) is used as a cathode in front of the primary and secondary anode. The voltage between the cathode and anode is in the order of magnitude 1.0 kV to 30.0 kV.

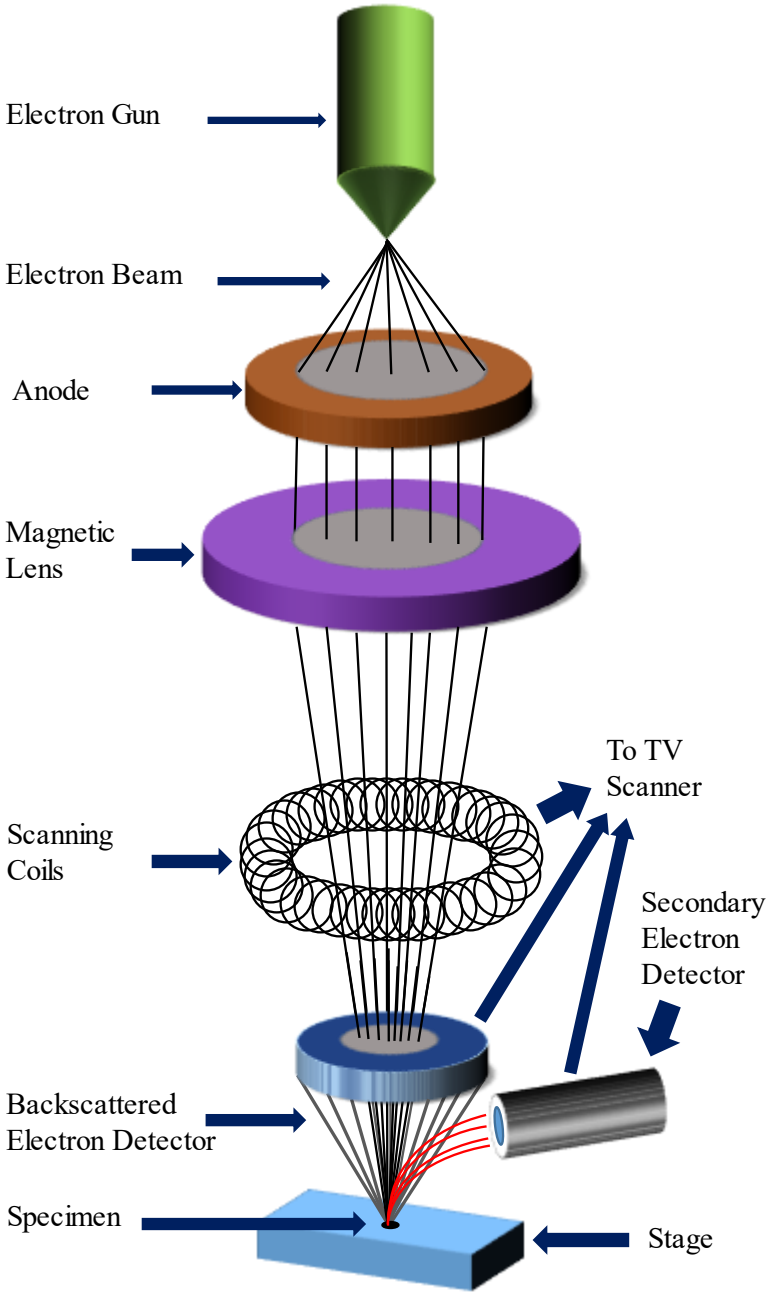

Figure 2.4: Schematic diagram of a SEM.

The electron beam produced by the field emission (FE) source is about 1000 times smaller than in a standard microscope; hence, the image quality is markedly better. After emerging from an electron gun. The electrons are accelerated toward the sample through a column that consists of condenser lenses, scanning coils, and objective lenses.

Condenser lens: The current in the condenser lens determines the diameter of the beam. A low current results in a small diameter, and a higher current produces in a larger diameter of the beam. A narrow beam produces better resolution. So, these lenses play an essential role in controlling the size of the spot.

Scanning coil: The scanning coil mainly controls the motion of the electron beam in two perpendicular directions. The electron beam from condenser lenses passes through the scanning coils. The current in the coils is altered in such a way that the electron beam scans the sample surfaces in a raster pattern. Scanning coils control the resolution of the SEM image by controlling the number of spots in the raster pattern. The scanning coils can also control magnification by changing the scan area on the sample surfaces.

Objective lens: The objective lens is the last lens in the column. The objective lens focuses the electron beam on the sample surface. At a short working distance, the objective lens needs to apply a greater force to deflect the electron beam. The shortest working distance produces the smallest beam diameter, hence resulting the best resolution.

Image formation: When the primary probe bombards the sample, the secondary electrons are emitted from the sample surface with a certain velocity determined by the levels and angles at the surface of the sample. The secondary electrons strike the scintillator that produces photons. The signal produced by the scintillator is amplified and sent to a cathode ray tube (CRT) imaging system.

The contrast in the real-time image that appears on the screen reflects the topographical structure on the surface of the sample.

The samples which are examined in SEM must be conducting or needed to be coated with gold. As the surfaces of our samples are conducting, so no gold coating is required. For taking SEM images, we place the samples on the sample holders and load the holders in the sample mounting stage. After loading the sample, the beam is turned on when chamber pressure goes below 5×10^{-3} Pa. Typically working voltage range is set at 2.0 kV to 50.0 kV. But for our samples, we have set it to 20.0 kV and spot size 3.0 microns. The images are generally taken at several magnifications between 3000x to 50000x magnification. The representative SEM images are shown in the respective Chapters.

2.5 Transport measurement

The transport properties have been measured using standard four-probe method **[20-22]**. We have measured the electrical resistivity (ρ), as a function of T down to 10.0 K, and IV characteristics at several constant temperatures below T_c **[23]**. A closed cycle refrigerator (CCR) (JANIS, USA), is used to decrease the temperature of the sample. The sample holder is kept within a highly vacuum chamber in which pressure is maintained at around 0.001 mbar by a rotary pump.

A Lakeshore temperature controller is used to monitor and control the sample temperature. The precision of the temperature controller is up to 0.01 K. We have used Keithley's constant current source to supply constant current through the sample and Keithley's nanovoltmeter (precision ~10 nV) to measure the voltage drop of the sample.

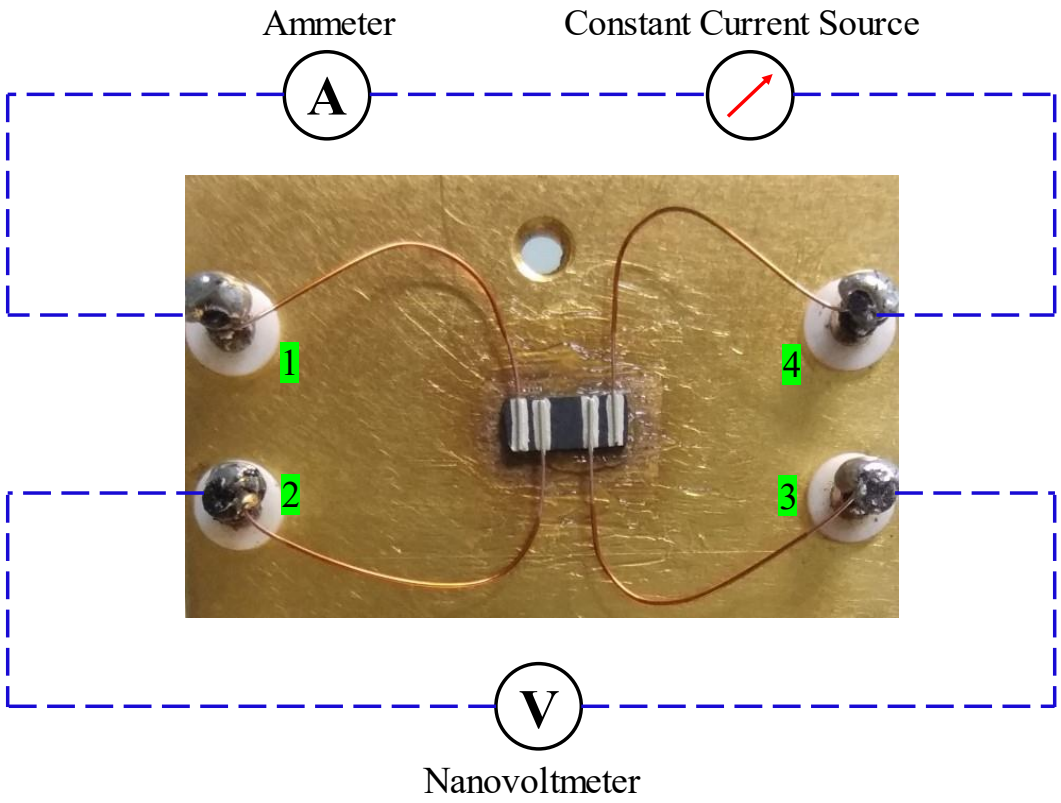

Figure 2.5: Four-probe configurations with bar-shaped sample mounted for transport measurement.

A schematic diagram of a four-probe technique is shown in **Figure 2.5**. A bar shaped sample is cut from the sintered pellet and mounted on the sample holder with the help of Apiezon N grease shown in **Figure 2.5**. Apiezon N grease is electrically insulating but thermally conducting. Delta mode is used to measure $\rho(T)$. DC sweep mode is used to measure *IV* characteristics. The delta mode

eliminates any offset or noise voltage present in the system. Typically, ±1 mA current is used for delta mode. We generally used the current range from 100 nA to 5 mA in DC sweep mode to measure *IV* characteristics at zero magnetic fields.

When current is passed through the sample by some external leads, there is a voltage drop across the sample to lead contact resistance. The four-probe method eliminates such voltage drops in the measured voltage value as separate leads are used to inject current in the sample and the voltage measurement. We have applied current through terminals **1** and **4** and sample voltage is measured between terminals **2** and **3** (shown in **Figure 2.5**). The contacts of the voltage and current leads on the sample surfaces are made by Cu wire with silver conducting adhesive paste. The contact resistance should be stable throughout the temperature range of 300.0 K to 10.0 K. In the present configuration, the value of resistivity is obtained by the formula

$$R = \rho \times \frac{l_{vv}}{w*t} \qquad \textbf{(2.2)}$$

where, l_{vv} is the separation between the voltage leads, and *w* & *t* are the width and thickness of the sample, respectively. In our configuration, for low resistive sample voltage lead separation, l_{vv} must satisfy the relation $l_{vv} > w > t$. The typical dimension of the bar shaped sample used for transport measurement is 6.0× 2.5 × 0.8 mm^3.

2.6 Vibrating Sample Magnetometer (VSM)

The VSM is a sensitive and versatile instrument for studying magnetic moment as a function of magnetic field and temperature **[24-26]**. The basic principle of operation for a VSM is that a varying changing magnetic flux will induce a voltage in a pick-up coil. The time-dependent induced voltage is given by $V_{coil} = \frac{d\Phi}{dt}$. Here Φ is the magnetic flux enclosed by the pick-up coil. For a sinusoidally oscillating sample position, the voltage is given by $V_{coil} = 2\pi CmAsin(2\pi ft)$, here C is a coupling constant, m is the DC magnetic moment of the sample, A is the amplitude of the oscillation and f is the frequency of oscillation.

The different constituent parts of the VSM are, (1) Vibrator and sample holder, (2) Lock-in amplifier, (3) Electromagnet and power supply, (4) Pick up coil or detection coil, (5) Sensor coil, (6) temperature variation system, (7) Computer interface **[27, 28]**. The schematic diagram of a VSM is shown in **Figure 2.6**. The cryogen-free magnet system allows to achieve low temperature 1.6 K and the maximum magnetic field can be applied upto 7.0 T. The sensitiveness of the VSM system is 10^{-6} emu. The cryocoolers operate using a helium compressor. There are two types of cryocoolers, the Gifford McMahon (GM) cryocooler, and Pulse Tube (PT) cryocooler. The GM cryocooler has the advantage of greater thermodynamic efficiency than PT cryocooler.

The sample is attached to the lower end of the rigid rod and made to oscillate vertically, typically over amplitude of 1.0 mm at frequencies typically 21 Hz. When the sample is magnetized or in response to an externally applied field, the

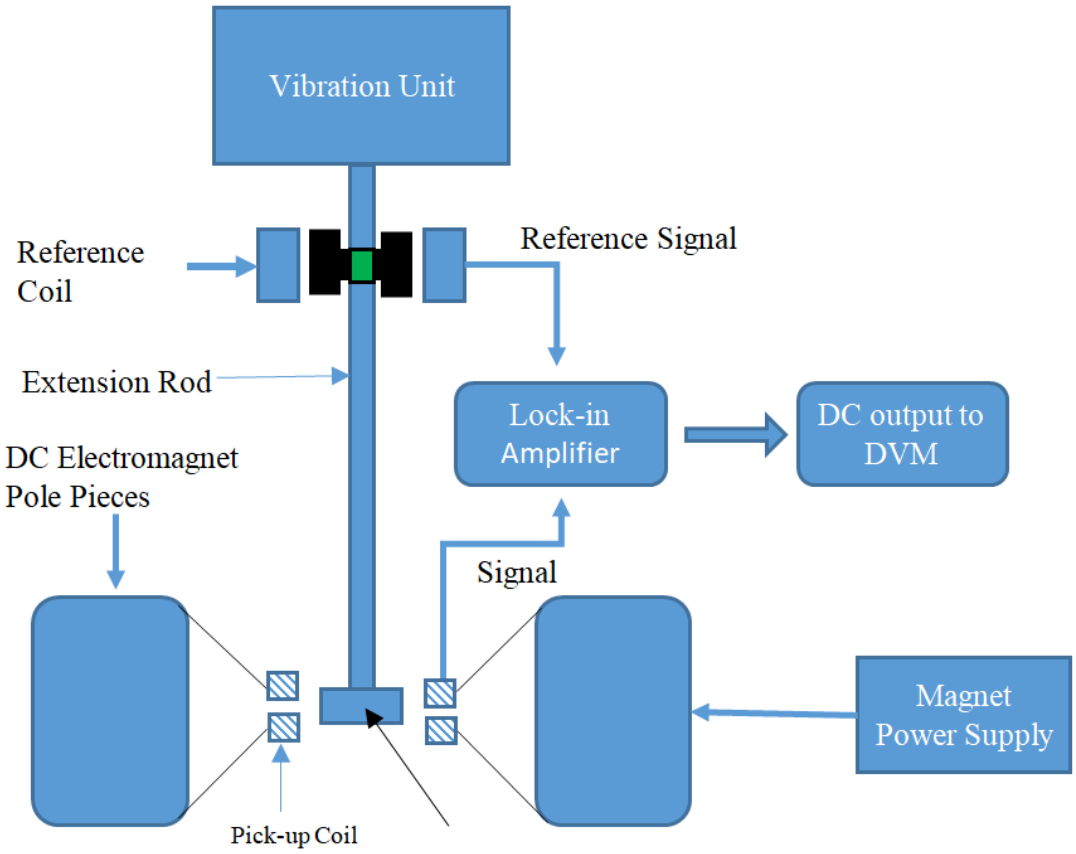

Figure 2.6: Schematic diagram of a VSM.

oscillation induces an AC signal in the pick-up coil. The amplitude of this signal is proportional to the magnetic moment of the sample. It is assumed that the size of the sample is much smaller than the dimensions of the pick-up coils. The pick-up coils are matched and connected in an opposite sense. Without a sample in position, an external field would induce equal and opposite voltages in the two sets of pick-up coils, which produced no overall signal. When the sample is in position, the upward motion of the sample causes an increase in flux through the

upper pick-up coils and a decrease in flux through the lower pick-up coils. The reverse is true for the downward motion of the sample. Therefore, the overall voltage induced when the sample is vibrating is proportional to the magnetic moment of the sample.

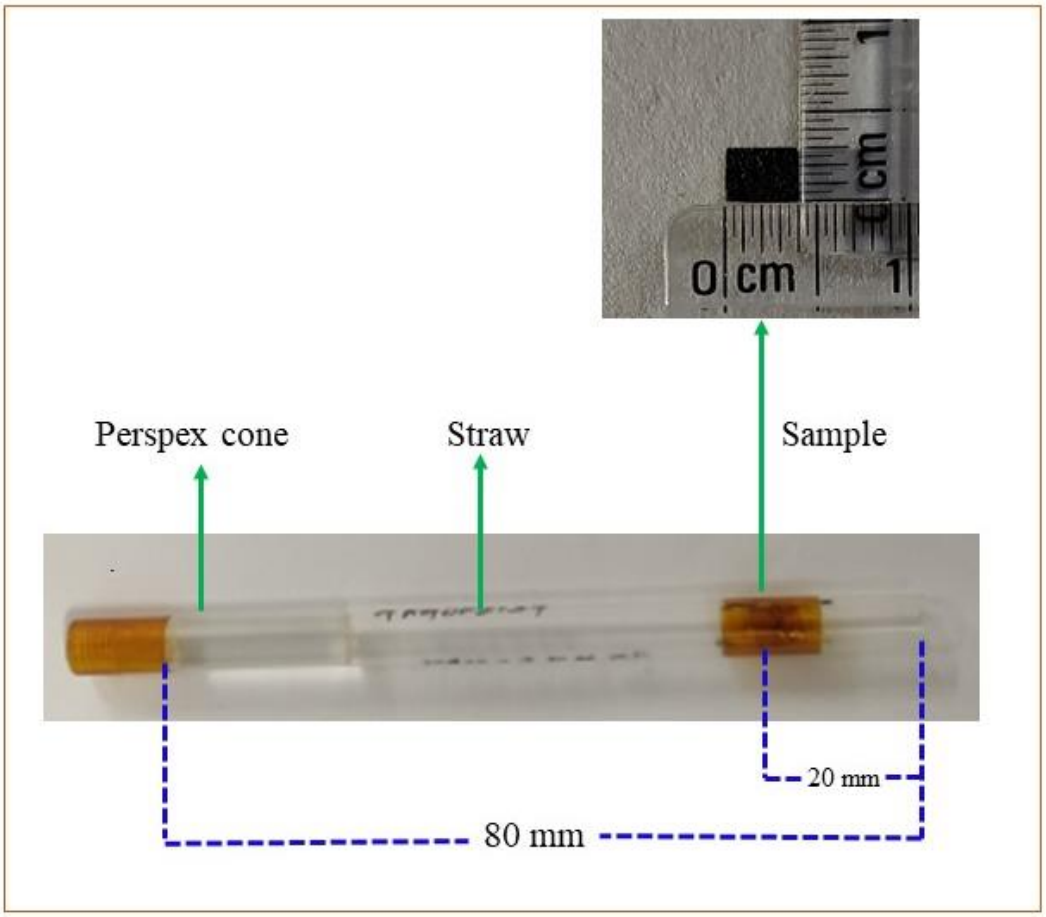

Figure 2.7: Sample mounting straw with bar shaped sample.

The quality of the measurement is generally affected by the dimensions, shape, and mass of the sample. The typical dimensions of the bar shaped sample used for magnetization measurement are $4.0 \times 3.0 \times 1.0$ mm^3. The mass of sample is about 45.0 mg. Mounting of the sample is one of the major parts of the measurement. A straw of length 80 mm is chosen for mounting the sample. Then

the sample is mounted using Kapton tape not more than 20 mm from the end of the straw. Finally, the sample straw is screwed onto the vibrating rod with the help of the Perspex cone, which is shown in **Figure 2.7**. Prior to the measurements, we ensure the positioning of the sample with respect to the pick-up coils using a low field (< H_{c1}) at a lower temperature (~ 2.0 K). We have measured magnetic moment (m) as a function of temperature, $m(T)$ below T_c at several fields, H up to 7T. Magnetic moment as a function of the magnetic field, $m(H)$ (up to $\pm$ 7 T), has also been measured at several fixed temperatures **[29, 30]**. A proper sequence consisting of several cycles of Zero Field Cooling Cycle (ZFCC), Zero Field Cooling Warming (ZFCW), Field Cooled Cooling (FCC), and Field Cooled Warming (FCW) have been used for $m(T)$ measurements. The temperature has been varied at a rate of 0.25 K/min for *m(T)*, and field has been varied at a rate of 0.05 T/min for $m(H)$ measurements.

2.7 References

[1] A. Stein, S. W. Keller, T. E. Mallouk, Science **259** (1993) 1558.

[2] J. M. Tarascon, P. Barboux, L. H. Greene, B. G. Bagley, G. W. Hull, Physica C **153** (1988) 566.

[3] A. Aliabadi, Y. A. Farshchi, M. Akhavan, Physica C **469** (2009) 2012.

[4] S. Komarneni, P. Ravindranathan, A. S. Bhalla, R. Roy, Bull. Mater. Sci. **14** (1991) 359.

[5] M. Kakihana, J. Sol-gel Sci. Technol. **6** (1996) 7.

[6] M. Mujaini, S. Y. Yahya, I. Hamadneh, R. Abd. Shukor, AIP Conf. Proc **1017** (2008) 119.

[7] P. Pramanik, S. Biswas, C. Singh, D. Bhattacharya, T. K. Dey, D. Sen, S. K. Ghatak, K. L. Chopra, Mat. Res. Bull. **23** (1988) 1693.

[8] A. A. Bunaciu, E. G. Udristioiu, H. Y. Aboul-Enein, Crit. Rev. Anal. Chem. **45** (2015) 289.

[9] M. A. Beno, L. Soderholm, D. W. Capone, D. G. Hinks, J. D. Jorgensen, J. D. Grace, I. K. Schuller, C. U Segre, K. Zhang, Appl. Phys. Lett. **51** (1987) 57.

[10] G. Balestrino, S. Barbanera, P. Paroli, J. Cryst. Growth **85** (1987) 585.

[11] H. M. Shao, K. Zhou, Y. Rui, j.c. Shen, X. N. Xu, H. L. Ji, X. X. Yao, L. J. Shen, Z. Wu, Z. J. Li, G. N. Zhang, G. C. Che, Z. X. Zhao, Solid State Commun. **97** (1994) 595.

[12] L. R. B. Elton, D. F. Jackson, Am. J. Phys. **34** (1966) 1036.

[13] W. L. Bragg, Nature **90** (1912) 410.

[14] D. Kriegner, Z. Matej, R. Kuzel, V. Holy, J. Appl. Cryst. **48** (2015) 613.

[15] A. Altomare, R. Caliandro, M. Camalli, C. Cuocci, I. D. Silva, C. Giacovazzo, A. G. G. Moliterni, R. Spagna, J. Appl. Cryst. **37** (2004) 957.

[16] S. Mollah, P. Mandal, T. Sk, S. Haldar, A. K. Ghosh, AIP Conf. Proc. **2220** (2020) 110044.

[17] M. Hartmann, K. Hipler, D. Koelle, F. Kober, K. Bernhardt, T. Sermet, R. Gross, R. P. Huebener, Z. Phys. B **75** (1989) 423.

[18] K. C. A. Smith, C. W. Oatley, Br. J. Appl. Phys. **6** (1955) 391.

[19] A. Frenkel, E. Clausen, C. C. Chang, T. Venkatesan, P. S. D. Lin, X. D. Wu, A. Inam, B. Lalevic, Appl. Phys. Lett. **55** (1989) 911.

[20] D. W. F. James, R. G. Jones, J. Sci. Instrum. **42** (1965) 283.

[21] Miccoli, F. Edler, H. Pfnür, C. Tegenkamp, J. Phys. Condens. Matter **27** (2015) 223201.

[22] M. Yamashita, T. Nishi, H. Mizutani, Jpn. J. Appl. Phys. **42** (2003) 695.

[23] I. Mukherjee, On the studies of current-voltage related exponents in doped cuprates at low temperature around the transition region, Thesis awarded for Ph.D. (Sc.), Jadavpur University (2021).

[24] S. Foner, Rev. Sci. Instrum. **30** (1959) 548.

[25] W. Burgei, M. J. Pechan, H. Jaeger, Am. J. Phys. **71** (2003) 825.

[26] B. W. Mangum, D. D. Thornton, Rev. Sci. Instrum. **41** (1970) 1764.

[27] V. Lopez-Dominguez, A. Quesada, J. C. Guzmán-Mínguez, L. Moreno, M. Lere, J. Spottorno, F. Giacomone, J. F. Fernández, A. Hernando, M. A. García, Rev. Sci. Instrum. **89** (2018) 034707.

[28] M. Springford, J. R. Stockton, W. R. Wampler, J. Phys. E: Sci. instr. **4** (1971) 1036.

[29] T. Sk, P. Mandal, D. Rakshit, A. K. Ghosh, Physica C **603** (2022) 1354152.

[30] T. Sk, P. Mandal, S. Haldar, Ajay Kumar Ghosh, Effectiveness of two pinning profiles in controlling magnetic critical current density in YBCO + YCMO composites (minor revision**).**

Chapter 3

Nonlinear current-voltage characteristics in electron doped YBCO superconductor below the critical temperature

3.1 Introduction

The σ_s in the superconducting system affects both the critical temperature and the critical current density. In several hole doped HTS, the relation between the σ_s at absolute zero and the critical temperature has been studied **[1-5]**. However, in several superconductors, the relation is even more complex and it depends on both the nature of the doping and the disorder level **[6, 7]**. The nonlinear relation between the σ_s and the critical temperature has been observed in numerous cuprate superconducting systems. Reduction in σ_s in cuprates has also been observed **[8]**. The electron-electron correlation in controlling the superfluid properties is an important aspect to understand the relation between the critical temperature and the σ_s **[9]**. The variation of the σ_s with the temperature in the

superconducting state is very important to understand the superconducting phase transition and the possibility of the BKT transition in HTS **[10-12]**.

By measuring the transport properties in electron doped superconducting systems, it is possible to understand the variation of the σ_s as a function of temperature **[2, 3]**. The nonlinear *IV* features are used to extract an exponent and hence to interrelate the phase transition and the variation of the SPS. In the present work we have extracted the SPS in several bulk Ce doped $YBa_2Cu_3O_{7-\delta}$ (YBCO). The determination of the SPS has been done by using the nonlinear nature of the *IV* curves obtained below the critical temperature by following the AHNS theory **[13, 14]**. We have also explored the possibility of the BKT transition in electron doped YBCO superconductors. The variation of the SPS with temperature in the phase transition region has been investigated. We have extracted a crossover temperature above which the suppression of the SPS and the increase in resistivity has been studied in all electron doped YBCO superconductors.

3.2 Experimental

We have synthesized several $Y_{1-x}Ce_xBa_2Cu_3O_{6.9}$ superconducting bulk samples by using the standard solid state reaction method **[15, 16]**. The concentration of Ce,

x is taken to be 0 (**S1**), 0.10 (**S2**), 0.15 (**S3**), 0.20 (**S4**), 0.25 (**S5**), 0.30 (**S6**), 0.35 (**S7**) and 0.4 (**S8**). The details of the synthesis route have been described in **Chapter 2**. We have characterized the granular nature of the samples by using SEM. Resistivity as a function of the temperature has been measured by using the standard four-probe method with the help of a cryogenerator **[17, 18]**. At several constant temperatures, the measurements of *IV* have been carried around and beyond the phase transition region.

3.3 Results and discussions

In **Figure 3.1(A)**, we have shown the variations of the resistivity, ρ, as a function of the temperature, T in $Y_{1-x}Ce_xBa_2Cu_3O_{6.9}$. The normal states of doped YBCO exhibit upturns for the concentration of electron doping, x = 0.25, 0.30, and 0.35, whereas other doped samples and pure YBCO have metallic normal states. However, ρ (300 K) varies strongly with the electron doping. The variations of the normalized resistivity, $\rho(T)/\rho$ (300 K) as a function of T has been shown in **Figure 3.1(B)**. **Figure 3.1(B)** clearly shows how the electron doping affects both the normal state as well as the phase transition region with respect to that of pure YBCO (x = 0). For several doping concentrations, the normal state becomes non-metallic with an upturn in $\rho(T)$. The variations of the $d\rho/dT$ as a function of T are shown in **Figure 3.2(A−H)** corresponding to samples with x = 0 (**S1**), 0.1

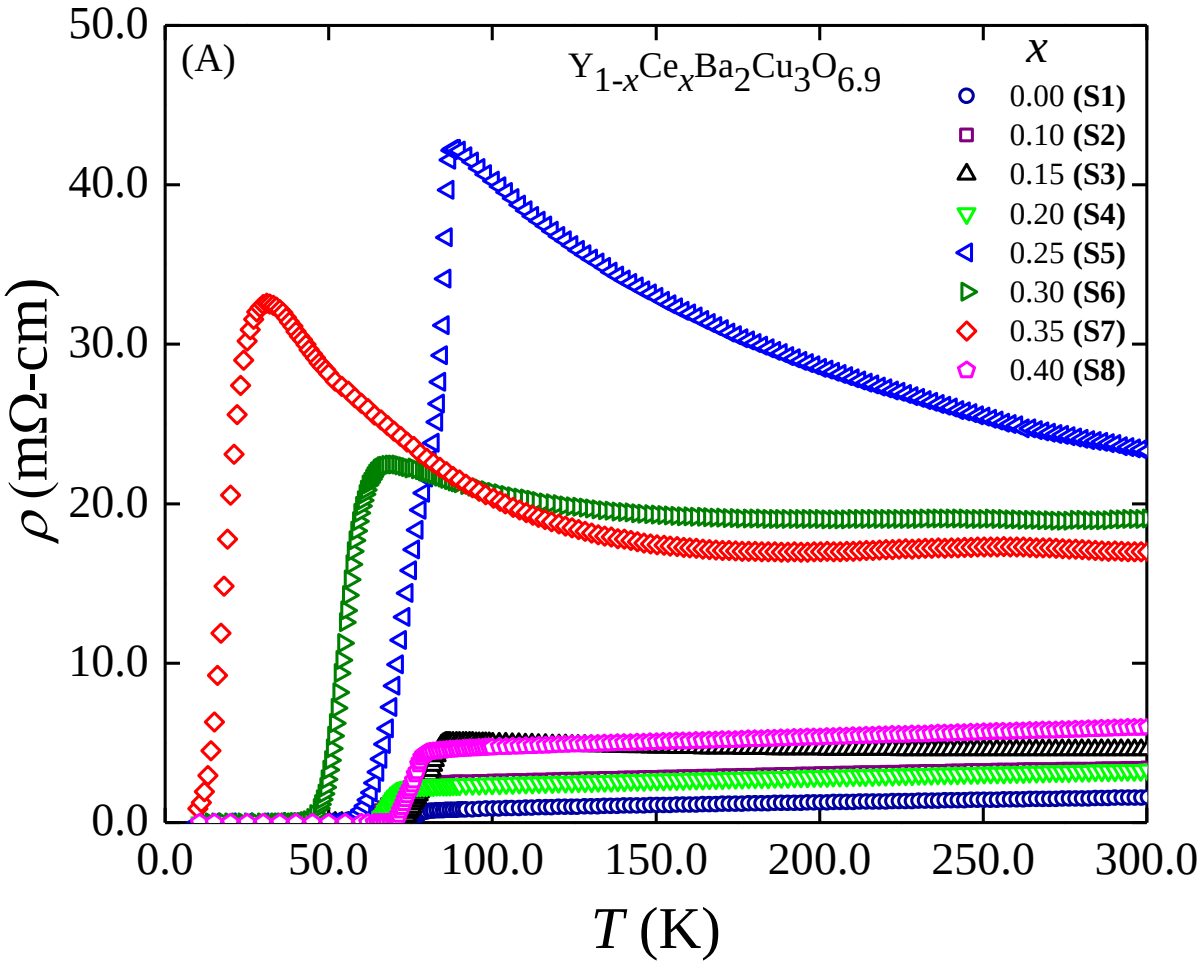

Figure 3.1(A): Resistivity as a function of temperature in $Y_{1-x}Ce_xBa_2Cu_3O_{6.9}$.

(**S2**), 0.15 (**S3**), 0.20 (**S4**), 0.25 (**S5**), 0.30 (**S6**), 0.35 (**S7**) and 0.40 (**S8**) respectively. $d\rho/dT$ (T) reveals how the normal states are sensitive to the electron doping **[19, 20]**. The observed upturn in resistivity in several doped samples corresponds to the negative value in the variation of $d\rho/dT$ (T). An upturn has been observed starting at T = 250.0 K, 300.0 K, 195.0 K and 180.0 K corresponding to x = 0.15, 0.25, 0.30 and 0.35 respectively. The superconducting onset T_c are found to be 82.0 K, 84.0 K, 88.0 K, 78.0 K, 90.0 K, 74.0 K, 37.0 K and 85.0 K corresponding to x = 0, 0.10, 0.15, 0.20, 0.25, 0.30, 0.35 and 0.40

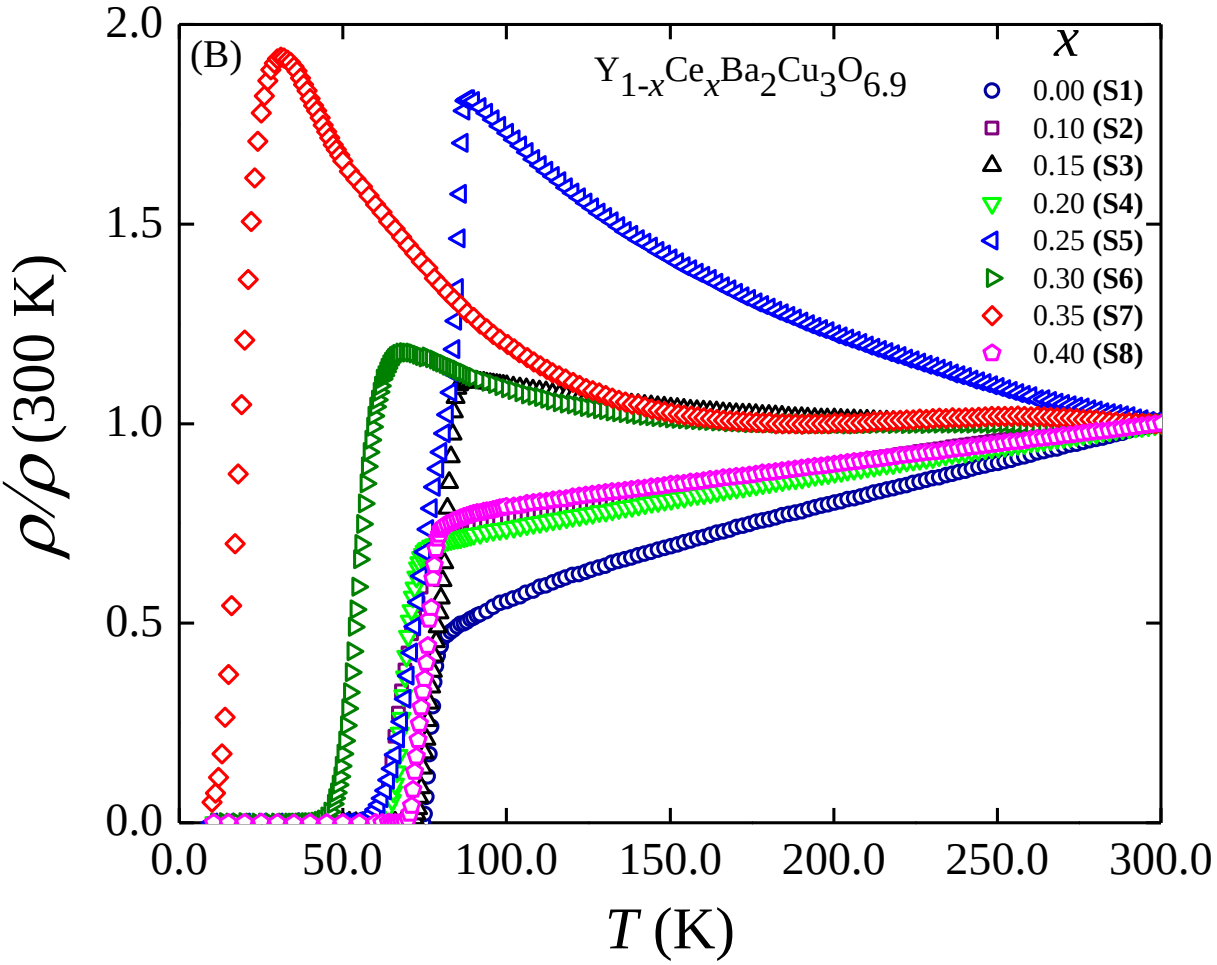

Figure 3.1(B): Normalized resistivity vs *T* in $Y_{1-x}Ce_xBa_2Cu_3O_{6.9}$.

respectively as given in **Table 3.1**. In **Figure 3.3(A− C)**, scanning electron micrographs of samples with x = 0, 0.2 and 0.3 are given as representatives. The granular natures in the pure and doped samples remains almost unchanged. It indicates that change in the resistive properties is mostly due to the change in the intrinsic in nature. The phase transition regions are generally very broad in most of the Ce doped samples which may make these samples better candidates for studying the role of the σ_s in controlling the superconducting phase transition **[7, 21]**.

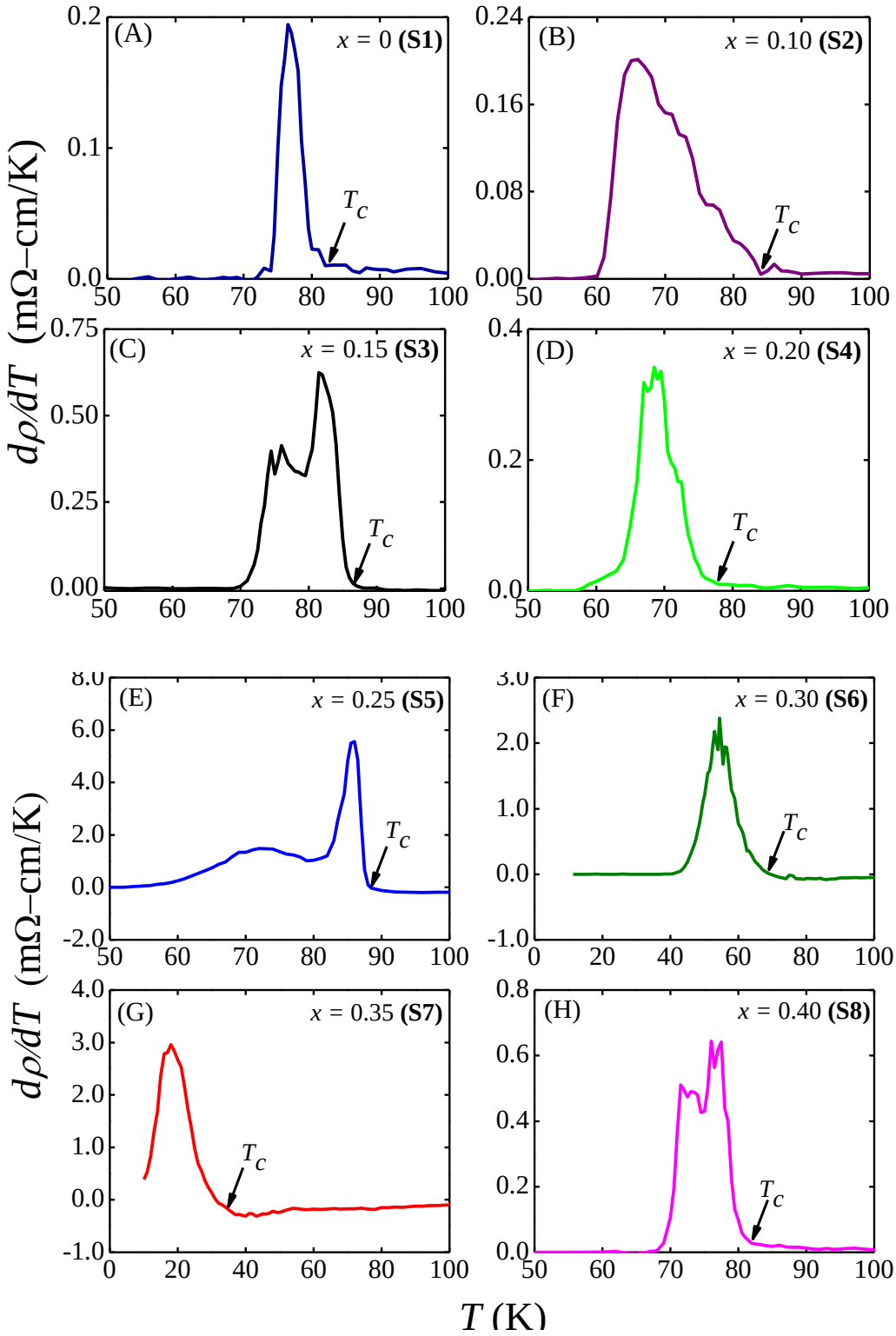

Figure 3.2(A-H): Variations of $d\rho/dT$ versus T in $Y_{1-x}Ce_xBa_2Cu_3O_{6.9}$ for (A) x = 0 (**S1**), (B) x = 0.10 (**S2**), (C) x = 0.15 (**S3**), (D) x = 0.20 (**S4**), (E) x = 0.25 (**S5**), (F) x = 0.30 (**S6**), (G) x = 0.35 (**S7**) and (H) x = 0.40 (**S8**).

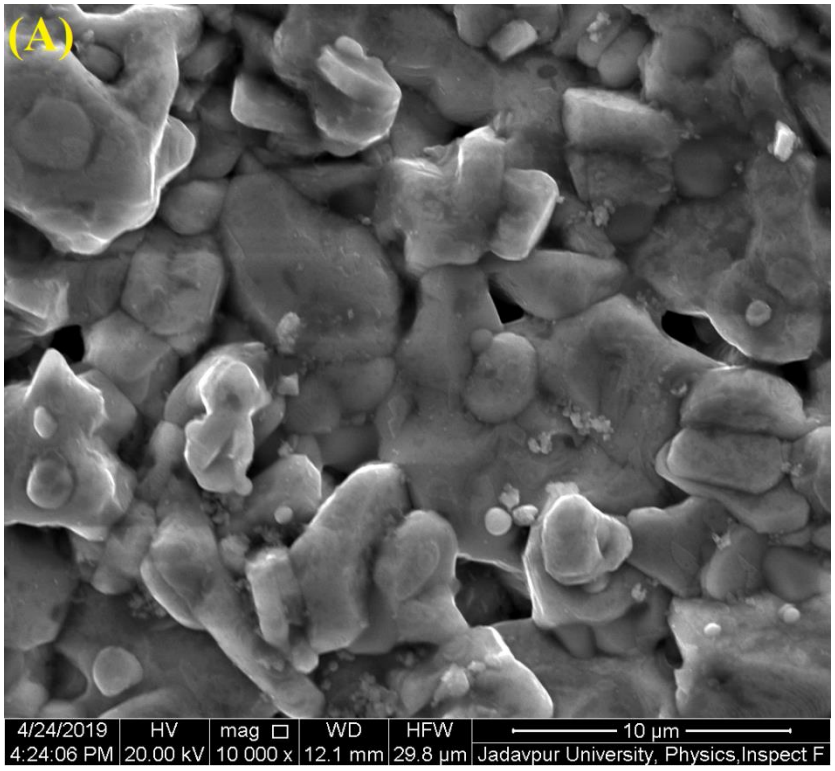

Figure 3.3(A): SEM of the sample $YBa_2Cu_3O_{6.9}$ **(S1)**.

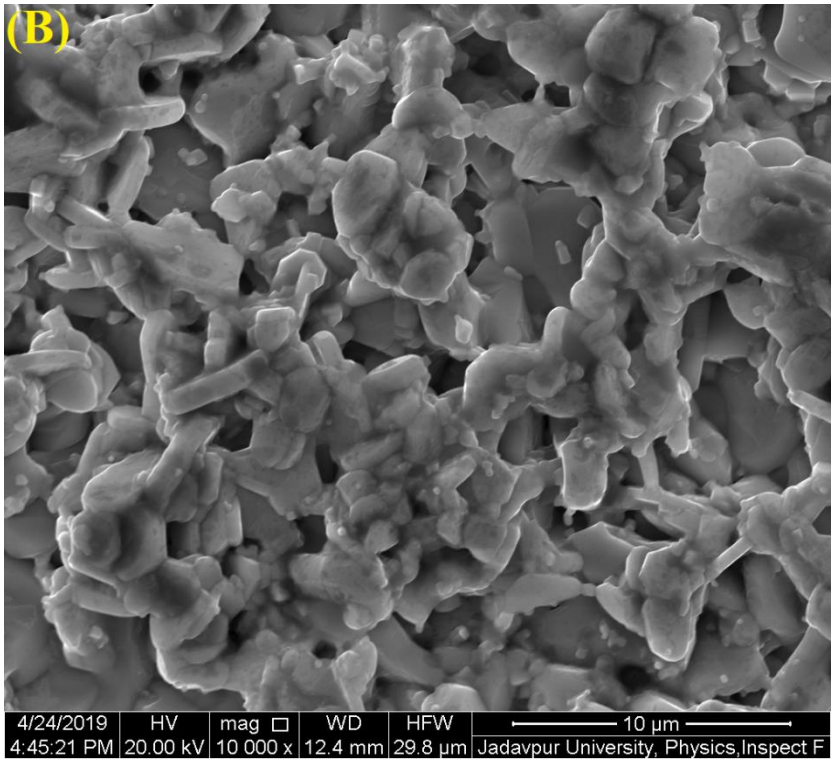

Figure 3.3(B): SEM of the sample $Y_{0.8}Ce_{0.2}Ba_2Cu_3O_{6.9}$ **(S4)**.

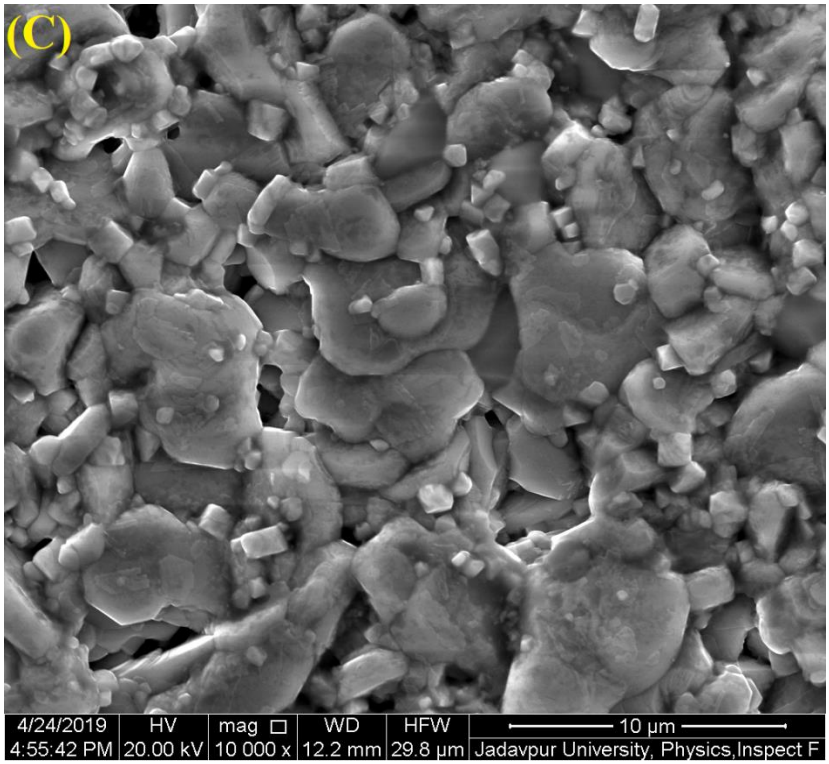

Figure 3.3(C): SEM of the sample $Y_{0.7}Ce_{0.3}Ba_2Cu_3O_{6.9}$ **(S6)**

In **Figure 3.4(A−H)** we have plotted *IV* curves in the *log-log* scale for different samples **[22-25]**. **Figures 3.4(A−H)** correspond to x = 0, 0.10, 0.15, 0.20, 0.25, 0.30 and 0.40. In the pure sample (x = 0), the variations of *IV* are linear in the range of T =75.0 K through 90.0 K as shown in **Figure 3.4(A)**. In several doped YBCO superconductors, the nonlinear variations in *IV* have been observed over a wide range of T **[26-28]**. (i) In **Figure 3.4(B)**, we have shown the *log-log* variations of *IV* of the sample with the lowest x = 0.10 in the range of T = 60.0 K through 80.0 K. In the vicinity of 60.0 K, the clear nonlinear *IV*s have been observed. In the inset of **Figure 3.4(B)**, we have shown a typical *IV* at 60.0 K with a fitting curve. (ii) In **Figure 3.4(C)**, we have shown the variations of *IV* in the *log-log* scale for the range of the temperature 74.0 K through 90.0 K for the

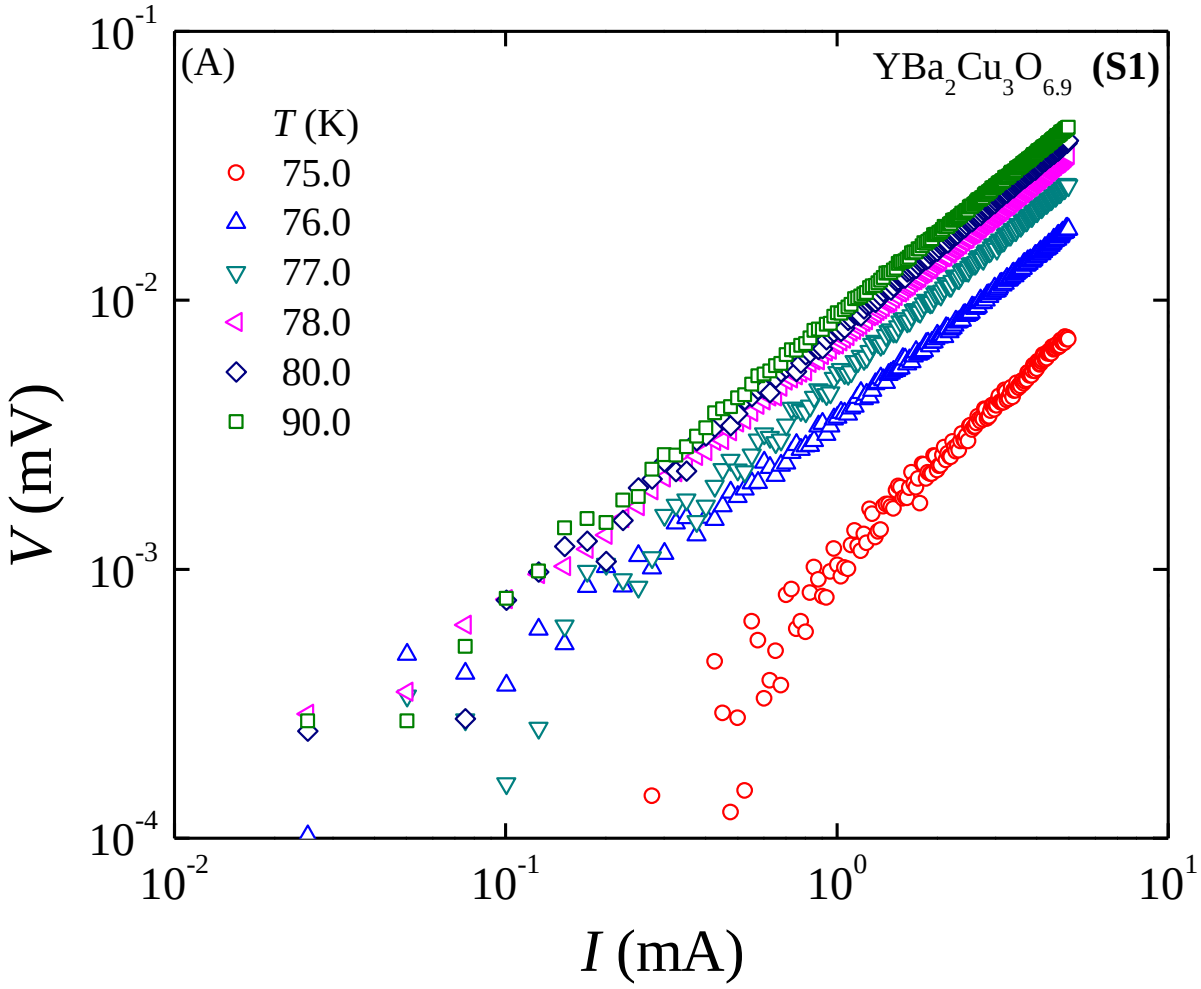

Figure 3.4(A): *IV* characteristics of $YBa_2Cu_3O_{6.9}$ **(S1)** at several temperatures.

sample with $x = 0.15$. The nonlinear variations are visible around the temperature of 74.0 K. A typical nonlinear variation of *IV* has been shown in the inset of **Figure 3.4(C)**. (iii) In **Figure 3.4(E)**, the variations of *IV* in the sample with $x = 0.25$ have been shown in the *log-log* scale for $T = 50.0$ K through 70.0 K. At several temperatures the nonlinear nature of *IV* has been observed. In the inset of **Figure 3.4(E)**, a typical nonlinear variation at $T = 52.0$ K has been shown. (iv) In **Figure 3.4(F)**, we have shown the variations of *IV* in the *log-log* scale for the

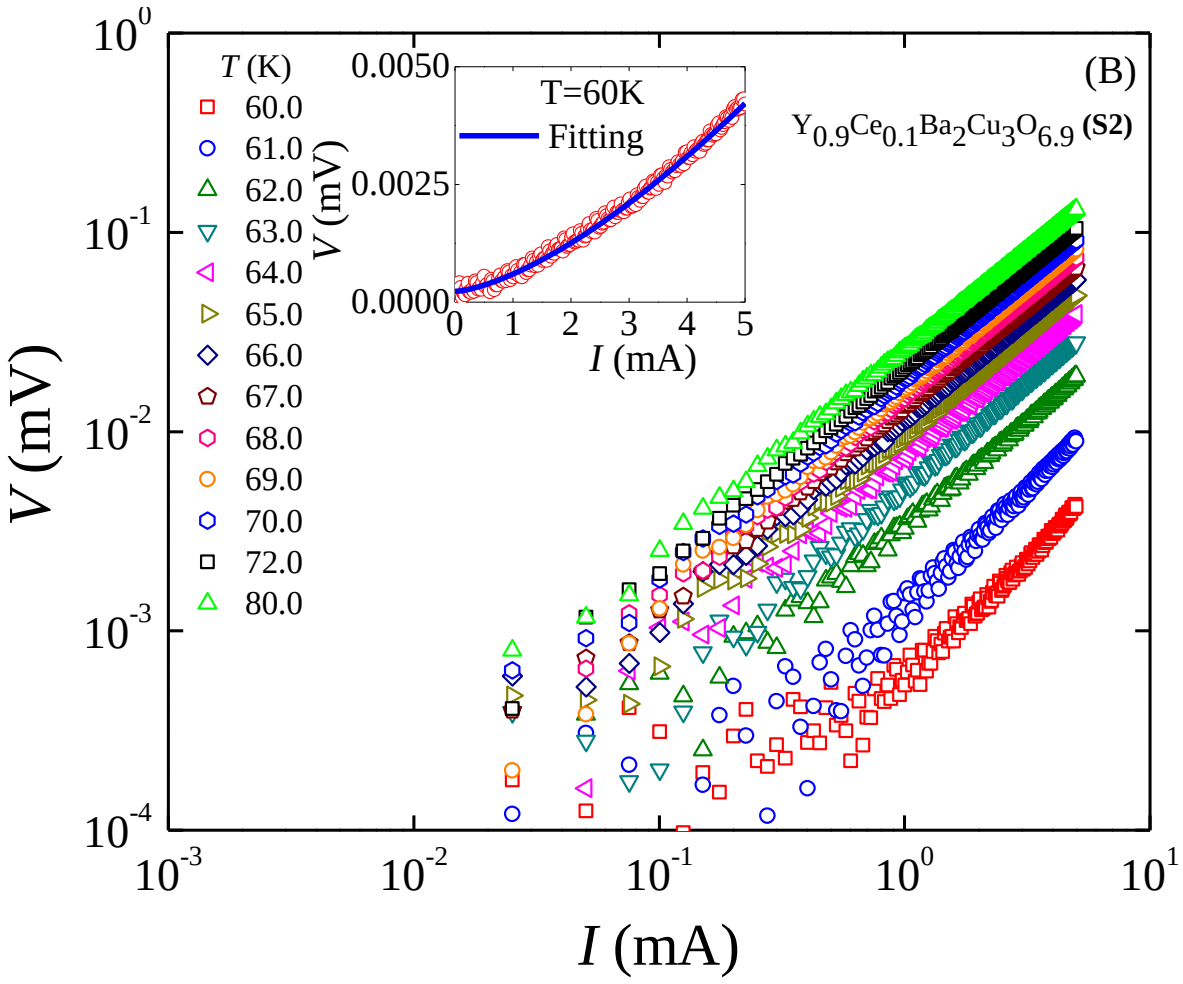

Figure 3.4(B): *IV* characteristics of $Y_{0.9}Ce_{0.1}Ba_2Cu_3O_{6.9}$ **(S2)** at several temperatures. Inset shown a typical nonlinear *IV* at 60.0 K with a fitting line using eqn **1.1**.

sample with x = 0.3 in the range of 46.0 K thorough 65.0 K. Over a wide range of T, the nonlinear variations are observed. A typical nonlinear *IV*-variation corresponding to 47.0 K has been shown in the inset of **Figure 3.4(F)**. (v) Below 30.0 K, several variations of *IV* have been shown in the *log-log* scale for the sample with x = 0.35 in **Figure 3.4(G)**. The typical nonlinear variation of *IV* at

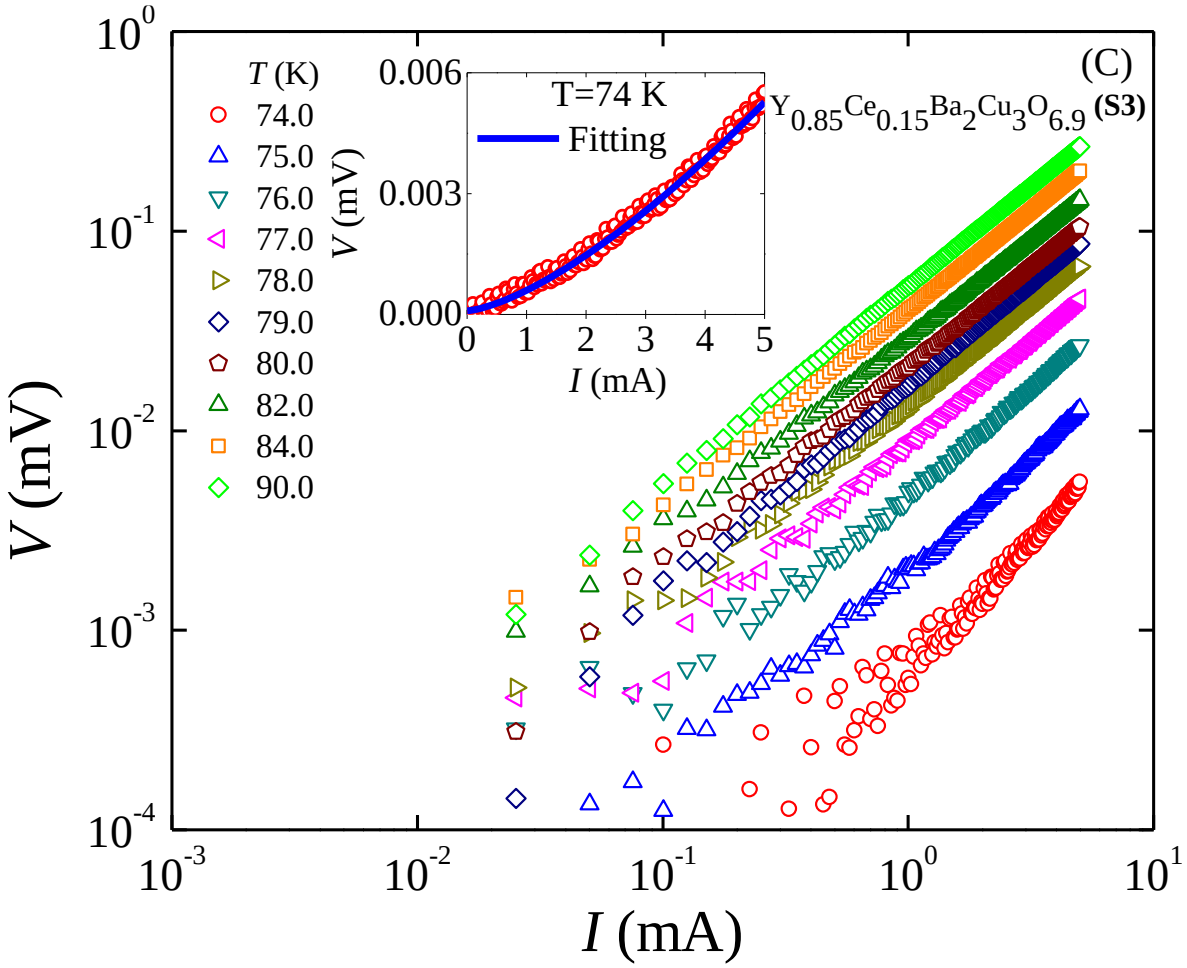

Figure 3.4(C): *IV* characteristics of $Y_{0.85}Ce_{0.15}Ba_2Cu_3O_{6.9}$ **(S3)** at several temperatures.

12.0 K has been given using a linear scale in the inset of **Figure 3.4(G)**. Therefore, the nonlinear variation in *IV* has been observed in most of the electron doped YBCO samples in different ranges of temperature **[3, 4]**.

The analysis of the nonlinear behavior has been carried out based upon an equation **1.1**. **[29, 30]**. We have extracted the exponent as a function of

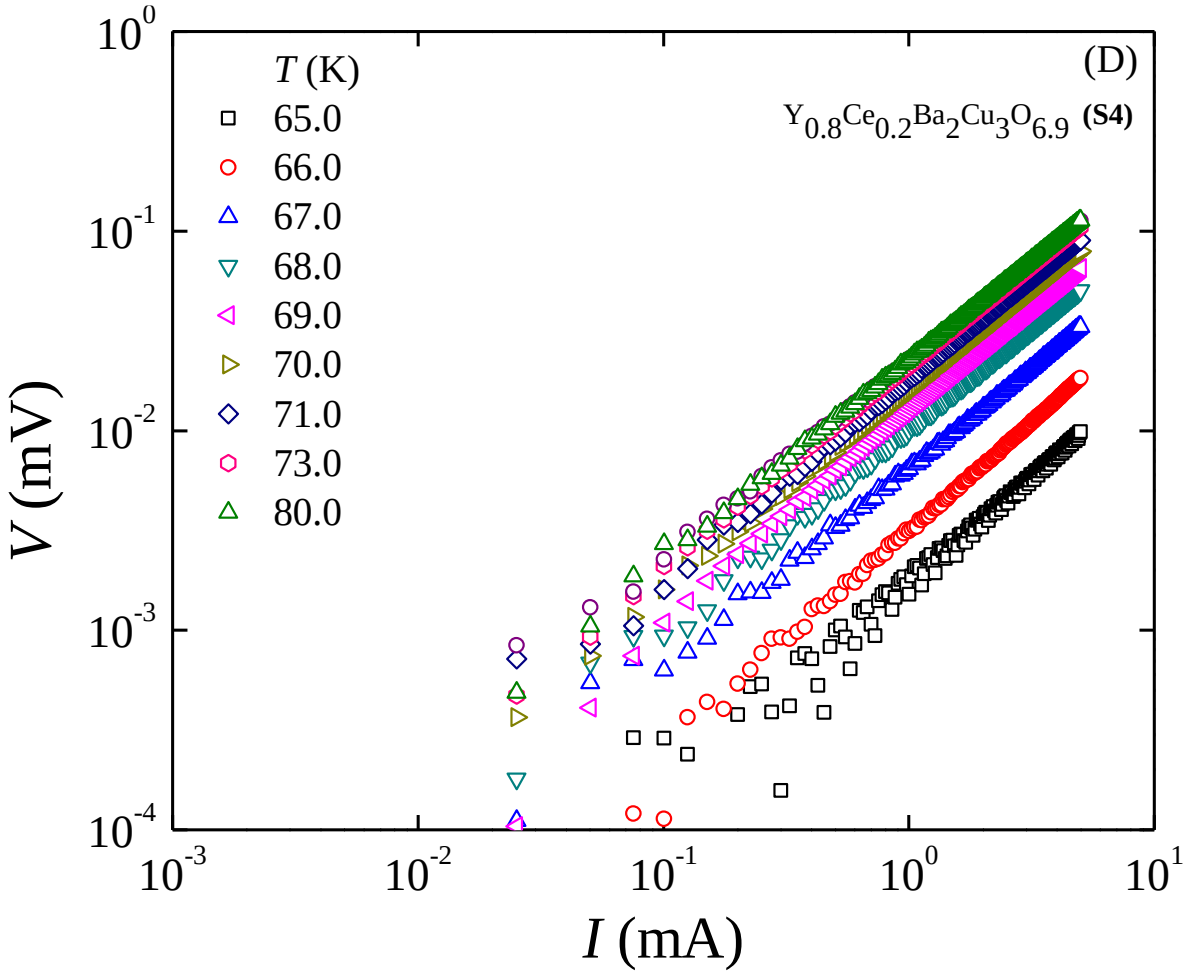

Figure 3.4(D): *IV* characteristics of $Y_{0.8}Ce_{0.2}Ba_2Cu_3O_{6.9}$ **(S4)** at several temperatures.

temperature for the electron-doped sample in which we have observed a very prominent nonlinear variation of *IV*. In **Figure 3.5**, we have plotted the variation of η with *T*. Any value of $\eta > 1.0$ reveals the nonlinear behavior. The minimum temperature, T_u, at which $\eta = 1.0$ may be associated with the onset of the BKT transition **[10, 11]**. We have obtained T_u = 67.0 K, 79.0 K, 72.0 K, 74.0 K, 64.0 K, 29.0 K and 72.0 K corresponding to x = 0.10, 0.15, 0.20, 0.25, 0.30, 0.35 and

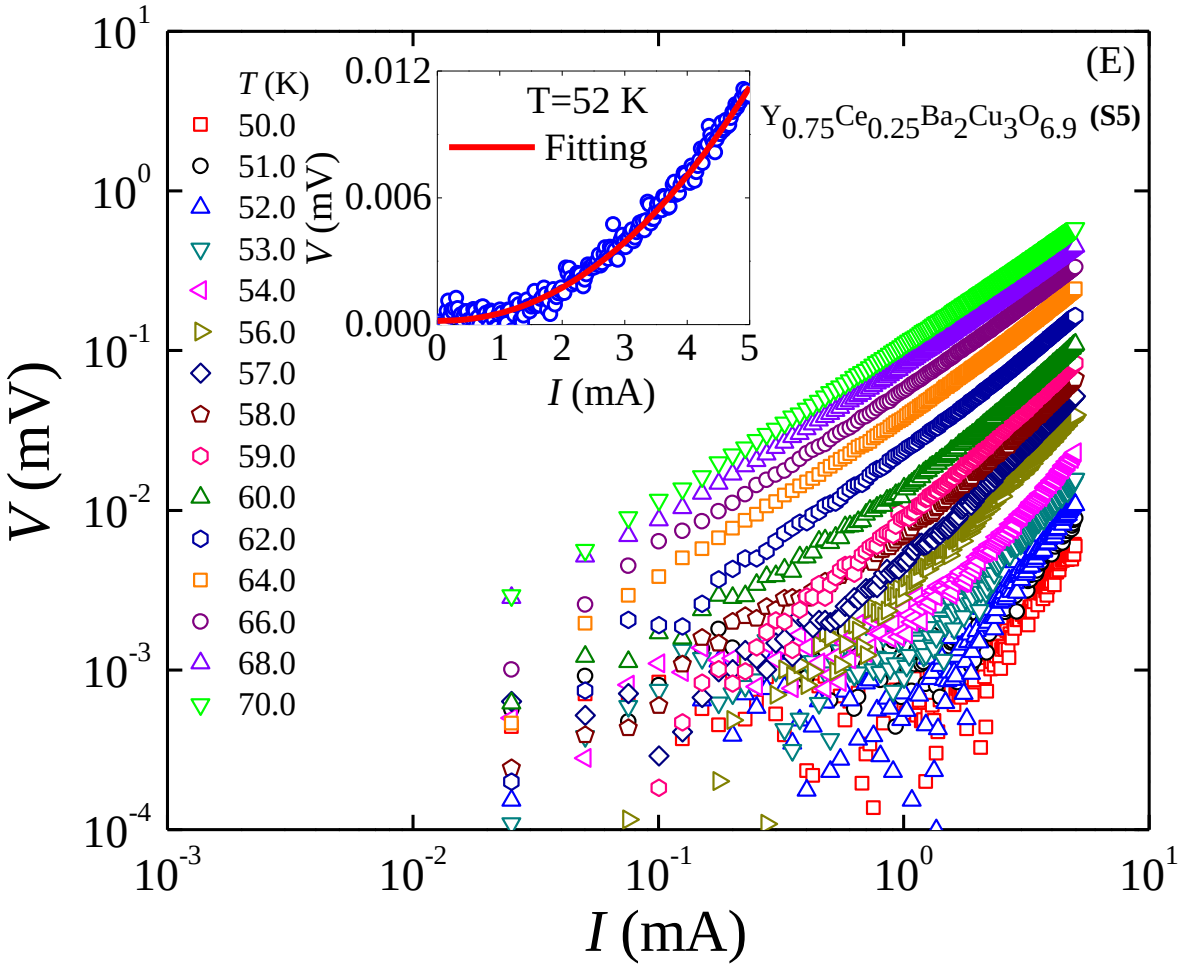

Figure 3.4(E): *IV* characteristics of $Y_{0.75}Ce_{0.25}Ba_2Cu_3O_{6.9}$ **(S5)** at several temperatures. Inset shown a typical nonlinear *IV* at 52.0 K with a fitting line using eqn **1.1**

0.40 respectively as given in **Table 3.1**. Below T_u, the nonlinear nature in electron doped samples may be an indicator of the detection of the BKT transition. However, down to 10.0 K, we have obtained a maximum $\eta = 2.5$ in the sample with $x = 0.35$. No change in the exponent from $\eta = 1.0$ to 3.0 has been observed. Hence, no complete BKT transition has been observed in any of these electrons doped samples. It would be important to mention that no single functional for has

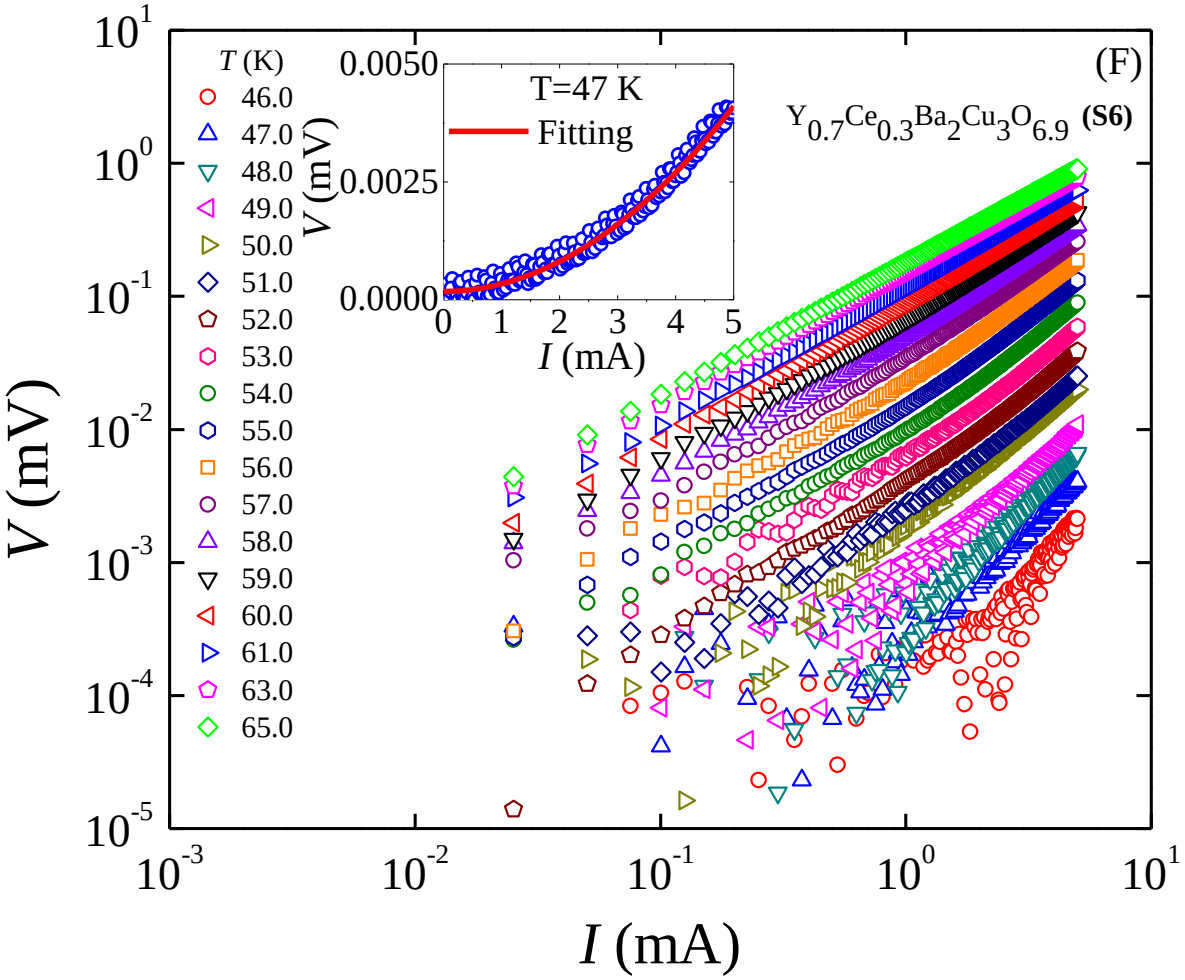

Figure 3.4(F): *IV* characteristics of $Y_{0.7}Ce_{0.3}Ba_2Cu_3O_{6.9}$ **(S6)** at several temperatures. Inset shown a typical nonlinear *IV* at 47.0 K with a fitting line using eqn **1.1**.

been obtained for fitting $\eta(T)$. However, extrapolating the nature of $\eta(T)$ we speculate that BKT transition may be observed at a lower temperature. Above the BKT transition temperature, there is an abrupt transition from a paired vortex state to a vortex unbinding state. The unbinding state is associated with the dissipation and hence higher resistive state. In addition, in electron doped YBCO samples the broad nature of the variation of $\eta(T)$ reveals the continuous phase

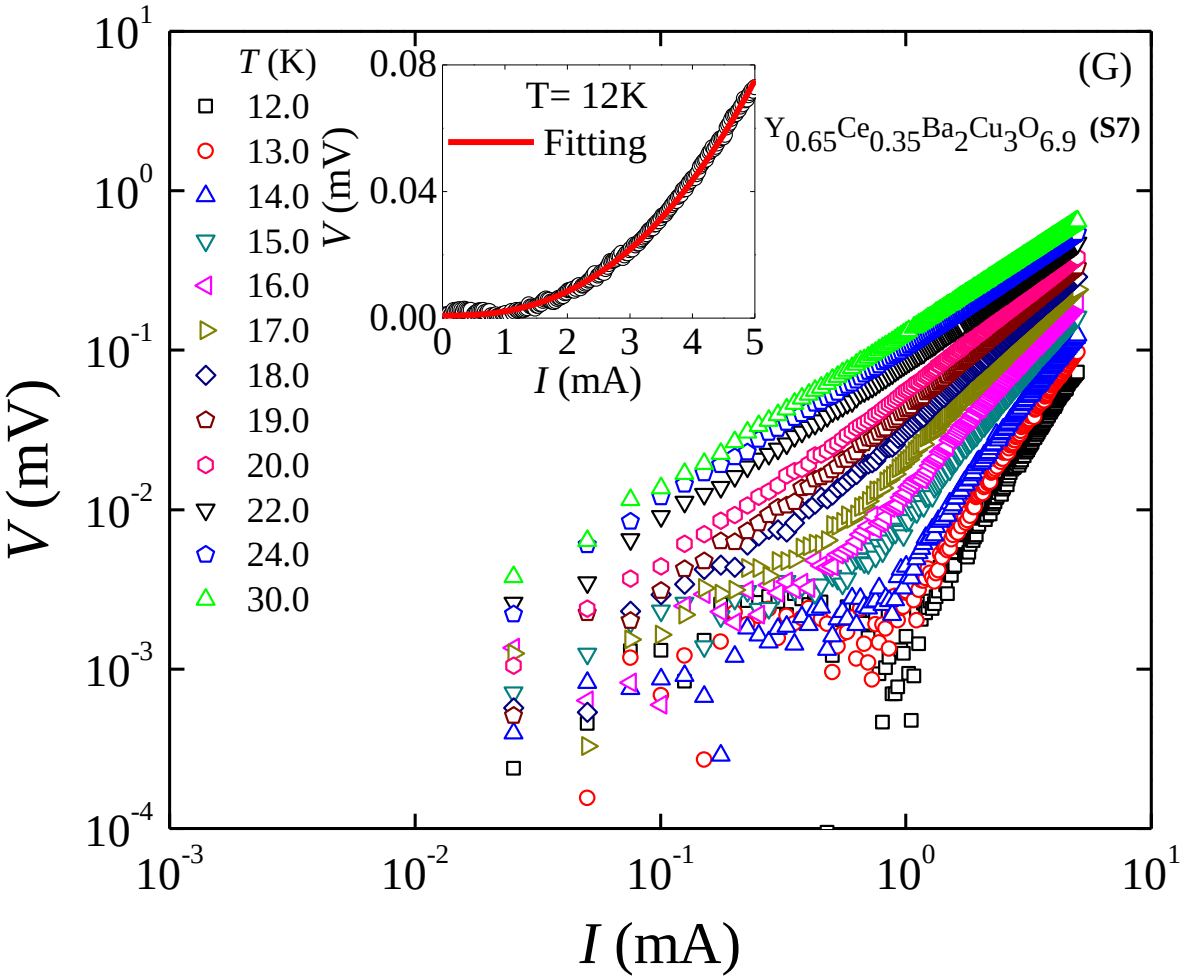

Figure 3.4(G): *IV* characteristics of $Y_{0.65}Ce_{0.35}Ba_2Cu_3O_{6.9}$ **(S7)** at several temperatures. Inset shown a typical nonlinear *IV* at 12.0 K with a fitting line using eqn **1.1**.

transition to the unbinding state with the increase in *T*. The nonlinear variation of $\eta(T)$ in cuprate superconductor has been observed earlier as well **[2, 31]**.

Following the AHNS model, we have found the SPS, J_s by using equation **1.2** **[13, 14]**. The superconducting phase transition region and the variation of the SPS

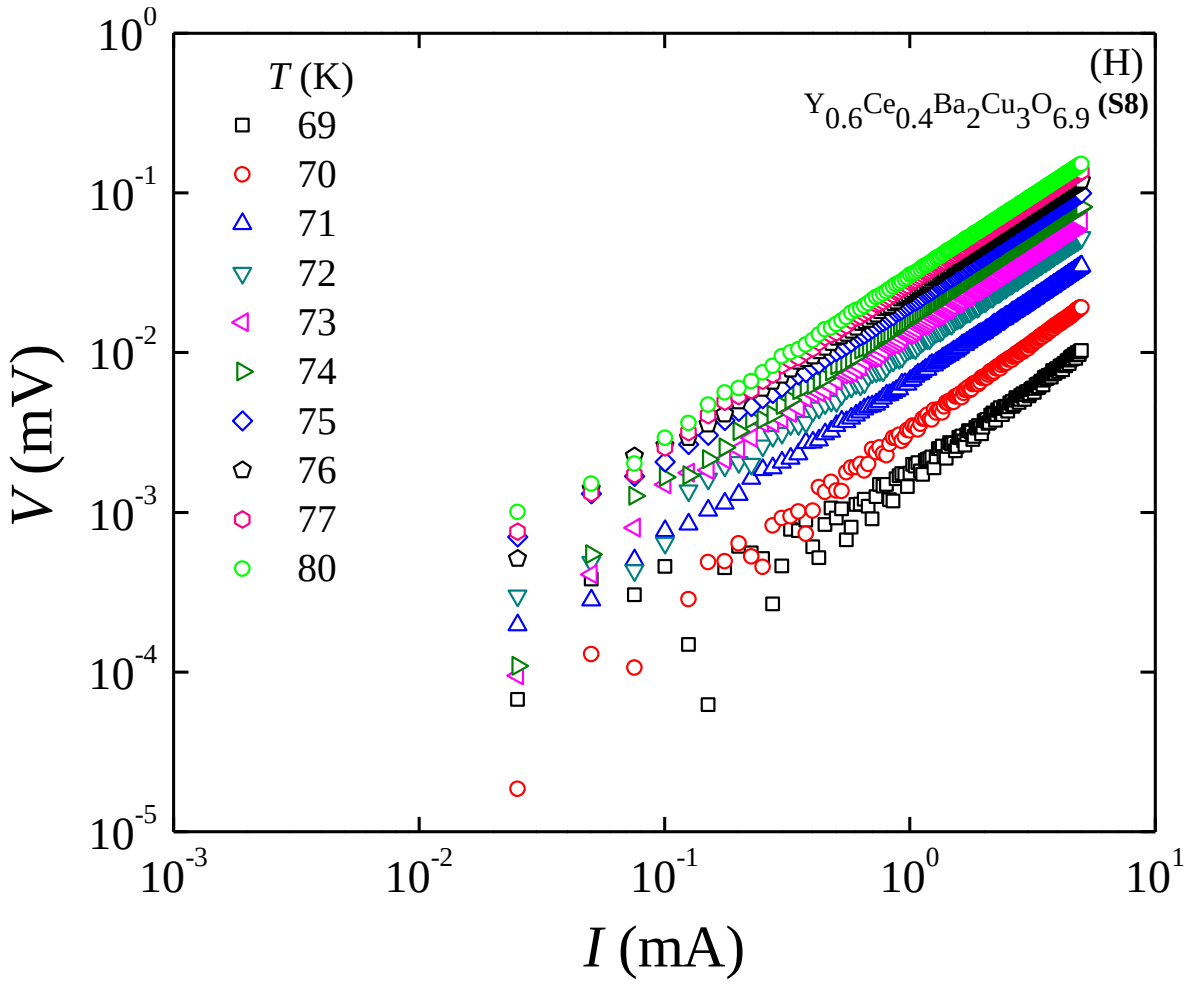

Figure 3.4(H): *IV* characteristics of $Y_{0.6}Ce_{0.4}Ba_2Cu_3O_{6.9}$ **(S8)** at several temperatures.

with *T* are strongly related. As the temperature is decreased the resistivity in the phase transition region decreases. However, with the decrease in *T* the J_s (*T*) increases. There are several types of such combinations of variations in cuprate superconductors **[32]**. In **Figure 3.6(A–G)**, we have shown (i) the variation of the resistivity with *T* and (ii) the SPS with *T* by using a combined plot for electron doped samples. Panels in **Figure 3.6(A–G)** correspond to *x* = 0.10, 0.15, 0.20,

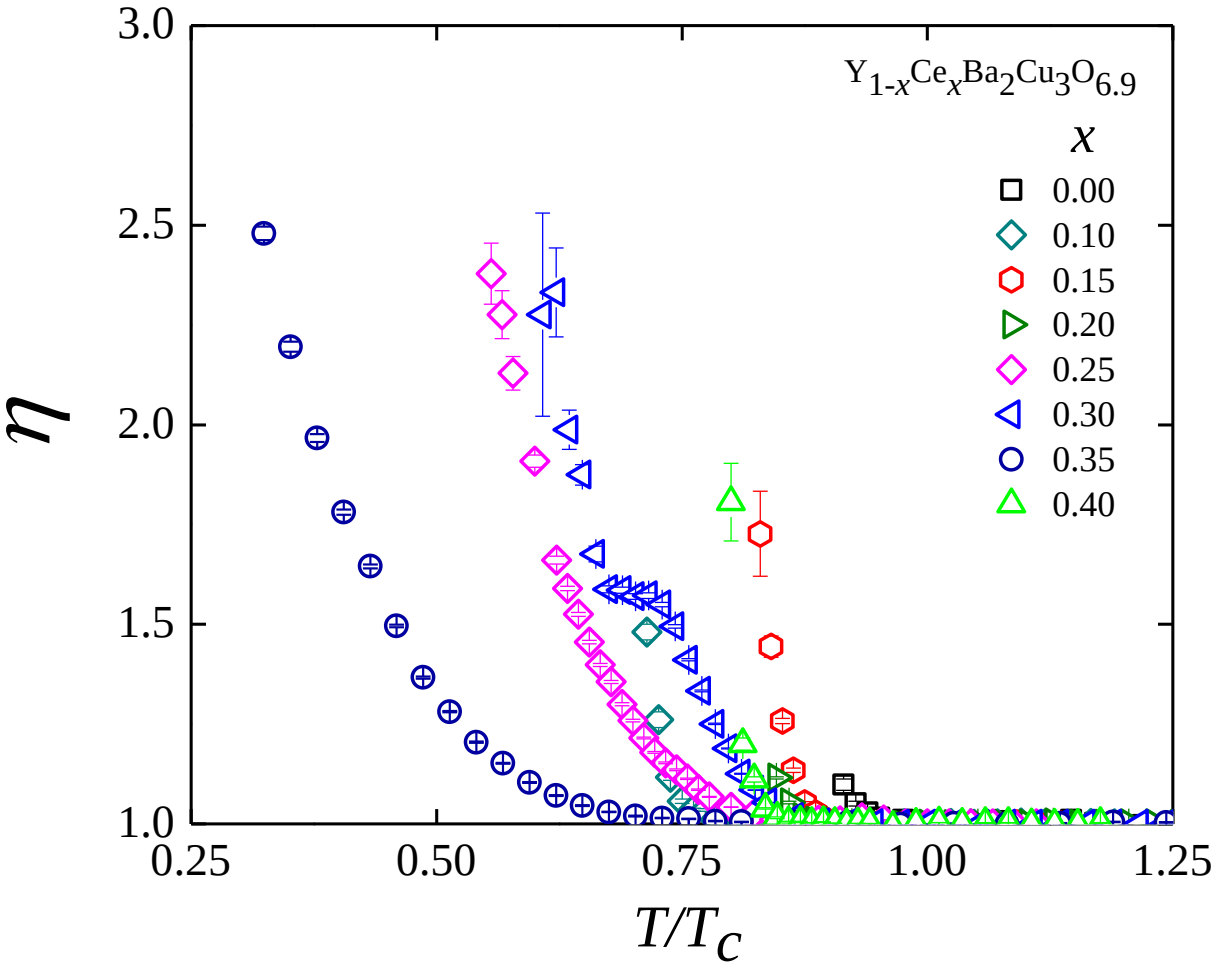

Figure 3.5: Variations of the exponent as a function of T for different values of x.

0.25, 0.30, 0.35 and 0.40 respectively. There is a crossover temperature, T_{cr}, for all electron doped samples as shown in **Table 3.1**. At $T = T_{cr}$, $J_s(T)$ and $\rho(T)$ intersects as revealed in **Figure 3.6(A−G)**. The crossover is consistent with the similar observations reported in several other Ca doped YBCO superconductors **[32]**. We found that below T_{cr} the growth of the $J_s(T)$ is very close to an exponential nature **[17]**. However, the exponential growth is very sensitive to the electron doping. Even at $T = T_c$ ($\rho = 0$), J_s is not equal for all electron doped

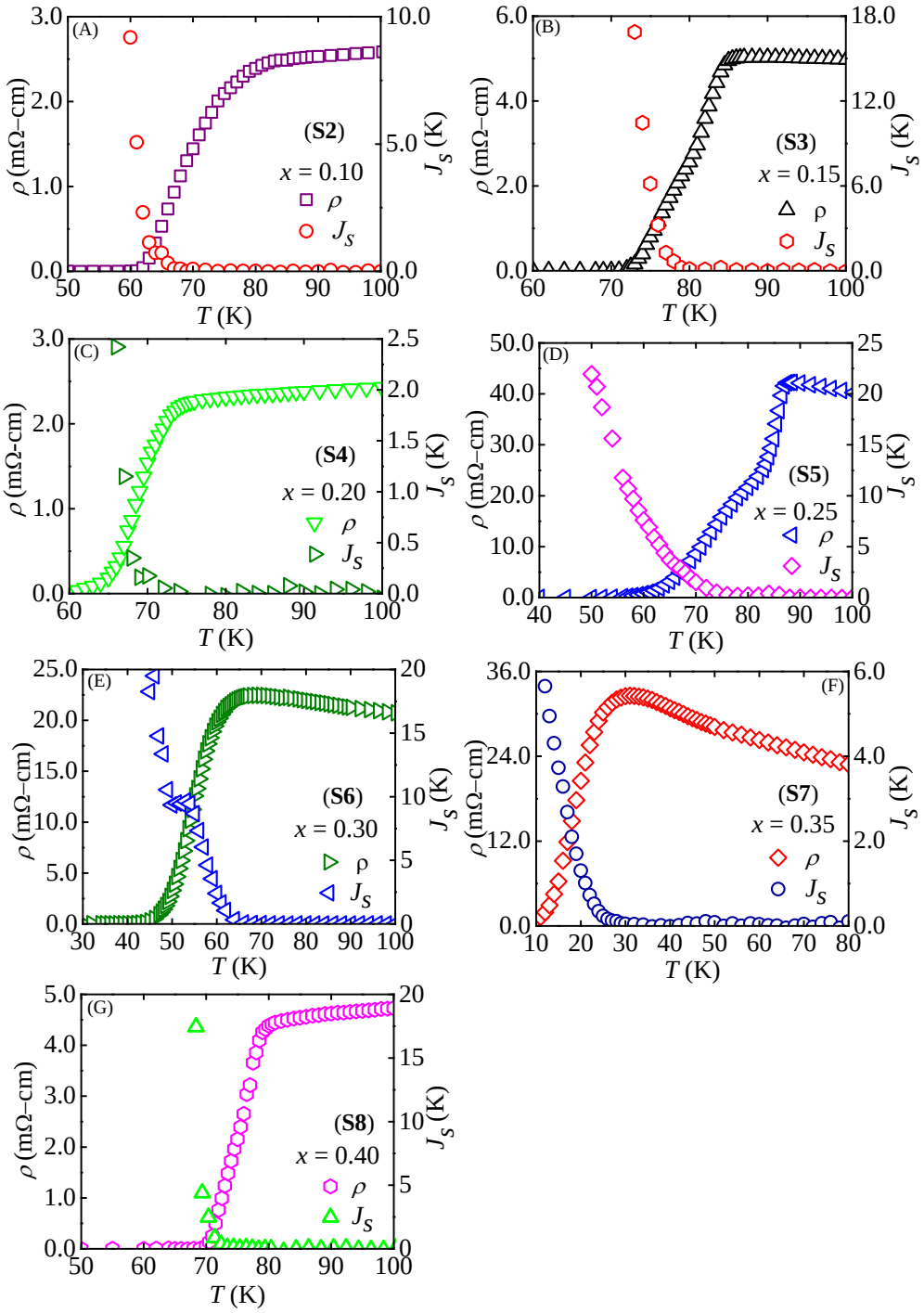

Figure 3.6(A–G): Combined plots of the resistivity and the SPS with *T*. Panels (A-G) correspond to **S2**, **S3**, **S4**, **S5**. **S6**. **S7** and **S8** respectively.

samples. It indicates that no specific critical J_s is required to exhibit the superconducting transition. We have observed that $T_u > T_{cr}$ and the separation of

x	T_c (K)	T_{cr} (K)	T_u (K)
0.00	82.0	------	-----
0.10	84.0	63.5	67.0
0.15	88.0	75.9	79.0
0.20	78.0	67.2	72.0
0.25	90.0	67.5	74.0
0.30	74.0	53.5	64.0
0.35	37.0	17.5	29.0
0.40	85.0	70.6	72.0

Table 3.1: List of different temperatures of several Ce doped YBCO samples.

these two temperatures, (T_u - T_{cr}), are very sensitive to the electron doping. The observed difference between T_{cr} and T_u also gives us an idea quantitatively that below superconducting T_c a vortex states related BKT phase transition occur in YBCO systems. It will be important to understand the variation of the J_s (T), within the range (T_u - T_{cr}) to correlate superconducting phase transition and BKT phase transition.

3.4 Summary

In several electron doped YBCO, the nonlinear variation of *IV* has been observed. The determination of an exponent reveals that complete BKT transition may be observed in electron doped YBCO. The SPS extracted by using AHNS theory varies nonlinearly with temperature. A crossing point, T_{cr}, below the unbinding temperature, T_u has been proposed and extracted below which the resistivity decreases and SPS increases. The separation between two characteristic temperatures, (T_u-T_{cr}) varies strongly with the electron density. The suppression of the J_s (T) above T_{cr} is clearly detectable for all doped samples.

3.5 References

[1] Y. J. Uemura, A. Keren, L. P. Le, G. M. Luke, W. D. Wu, Y. Kubo, T. Manako, Y. Shimakawa, M. Subramanian, J. L. Cobb, J. T. Markert, Nature **364** (1993) 605.

[2] I. Božović, X. He, J. Wu, A. T. Bollinger, Nature **536** (2016) 309.

[3] I. Hetel, T. R. Lemberger, M. Randeria, Nature **3** (2007) 400.

[4] N. R. Lee-Hone, J. S. Dodge, D. M. Broun, Phys. Rev. B **96** (2017) 024501.

[5] P. J. Hirschfeld, N. Goldenfeld, Phys. Rev. B **48** (1993) 4219.

[6] F. Mahmood, X. He, I. Bozovic, N. P. Armitage, Phys. Rev. Lett. **122** (2019) 027003.

[7] I. Bozovic, A.T.Bollinger, J.Wu, X.He, Low. Temp. Phys. **44** (2018) 519.

[8] M. V. Feigel'man, L. B. Ioffe, Phys. Rev. B **92** (2015) 100509 (R).

[9] V. A. Khodel, J. W. Clark, M. V. Zverev, Phys. Rev. B **99** (2019) 184503.

[10] J. M. Kosterlitz, D. J. Thouless, J. Phys. C **6** (1973) 1181.

[11] V. L. Berezinskii, Zh. Eksp. Teor. Fiz **61** (1971) 1144.

[12] L. Benfatto, C. Castellani, T. Giamarchi, Phys. Rev. Lett. **98** (2007) 117008.

[13] V. Ambegaokar, H. Halperin, D. Nelson, E. Siggia, Phys. Rev. Lett. **40** (1978) 783; Phys. Rev. B **21** (1980) 1806.

[14] B. I. Halperin, D. R. Nelson, J. Low Temp. Phys. **36** (1979) 599.

[15] B. Biswas, S. Haldar, I. Mukherjee, A. K. Ghosh, Physica B **506** 173 (2017).

[16] I. Mukherjee, S. Mollah, T. Sk, S. Haldar, and A. K. Ghosh, Physica C **560** (2019) 67.

[17] P. Das, A. K. Ghosh, Physica C **548** (2018) 27.

[18] T. Sk, A. K. Ghosh, J. Low Temp. Phys. **198** (2020) 224.

[19] P. A. Lee, N. Nagaosa, X.-G. Weng, Rev. Mod. Phys.**78** (2006) 17.

[20] C. Bernhard, Ch. Niedermayer, U. Binninger, A. Hofer, Ch. Wenger, J. L. Tallon, G. V. M. Williams, E. J. Ansaldo, J. I. Budnick, C. E. Stronach, D. R. Noakes, M. A. Blankson-Mills, Phys. Rev. B **52** (1995) 10488.

[21] G. C. Kim, M. Cheon, S. S. Ahn, J. H. Jeong, Y. C. Kim, EPL **81** (2008) 27005.

[22] J. M. Repaci, C. Kwon, Qi Li, X. Jiang, T. Venkatessan, R. E. Glover, C. J. Lobb, R. S. Newrock, Phys. Rev. B **54** (1996) R9674.

[23] J. Yong, M. J. Hinton, A. McCray, M. Randeria, M. Naamneh, A. Kanigel, T. R. Lemberger, Phys. Rev. B **85** (2012) 180507.

[24] P. G. Baity, X. Shi, Z. Shi, L. Benfatto, D. Popović, Phys. Rev. B **93** (2016) 024519.

[25] D.M. Broun, W.A. Huttema, P.J. Turner, S. Ozcan, B. Morgan, R. Liang, W. N. Hardy, D.A. Bonn, Phys. Rev. Lett. **99** (2007) 237003.

[26] P. C. E. Stamp, L. Forro, C. Ayache, Phys. Rev. B **38** (1988) 2847.

[27] D. P. Norton, D. H. Lowndes, Phys. Rev. B **48** (1993) 6460.

[28] N.-C. Yeh, C. C. Tsuei, Phys Rev. B **39** (1989) 9708.

[29] L. Benfatto, C. Castellani, T. Giamarchi, Phys. Rev. B **80** (2009) 214506.

[30] N. Reyren, S. Thiel, A. D. Caviglia, L. F. Kourkoutis, G. Ham-merl, C. Richter, C. W. Schneider, T. Kopp, A.-S. Rüetschi, D. Jaccard, M. Gabay, D. A. Muller, J. M. Triscone, J. Mannhart, Science **317** (2007) 1196.

[31] Y. Zuev, M. S. Kim, T. R. Lemberger, Phys. Rev. Lett. **95** (2005) 137002.

[32] S. Steers, T. R. Lemberger, J. Draskovic, Phys. Rev. B **94** (2016) 094525.

Chapter 4

Nonlinear current-voltage characteristics in composite systems consisting of YBCO superconductor and Y_2CoMnO_6

4.1 Introduction

The nonlinear variation of the *IV* characteristic below the critical temperature in superconducting systems is related to the phase transition in vortex configuration **[1, 2]**. An important question is how to control the nonlinearity in *IV*. There are several ways to trigger the nonlinear behaviour in cuprate superconducting systems **[3-8]**. All processes by which the nonlinearity can be altered are of two types in nature in bulk superconducting samples (i) elemental substitution in lattice sites including elemental disorder and twin boundaries and (ii) tuning the inter-granular networks. In cuprate superconductors both processes are effective in controlling the nonlinear behaviour and related outcomes. Commonly used cuprate superconductors are found to exhibit strong sensitiveness of the σ_s to the doping level. By changing doping level superfluid stiffness has been studied in a

wide range. The dependence of the σ_s on the doping level at different temperatures below the critical temperature is different in nature **[9]**.

Even though tuning the nonlinearity through the changes in the lattice site is very popular practice it is also very important to understand how the nonlinear behaviour changes using the inter-granular networks. An important question remains how magnetic structure in the inter-granular network region in the bulk sample influences the nonlinear nature in the *IV* behaviour. It will be even more interesting to understand how superfluid behaviour is affected as a result of the inclusion of magnetic inter-granular components. Composite system of $YBa_2Cu_3O_{7-\delta}$ (YBCO) and Y_2CoMnO_6 (YCMO) have been used for the present study. We have used a low concentration of 5% of YCMO as magnetic material for making the inter-granular network. Several YBCO superconductors have been used for the composite systems. Transport properties of both (i) pure YBCO and (ii) composite systems are analysed to understand the change in the superfluid property. An exponent has been extracted for all systems. Its variation with the temperature has been discussed within the frame work of the AHNS theory.

4.2 Experimental

We have synthesized $YBa_2Cu_3O_{7-\delta}$ by using the standard solid state reaction method. Nominal values of δ are 0 (**S9**), 0.1 (**S10**), 0.3 (**S11**) and 0.5 (**S12**). A part of the sample **S9** and 5% of Y_2CoMnO_6 (YCMO) are mixed thoroughly. Similar mixing has been done using other pure samples of **S10**, **S11** and **S12**. Mixed samples are labelled as **S13**, **S14**, **S15** and **S16**. Annealing of the pure and mixed samples is carried out at 450^{o}C using uniform oxygen flow rate. Resistivity as a function of temperature has been measured by using the standard four-probe method with the help of a CCR **[10, 11]**. At several constant temperatures *IV* measurements have been carried around the phase transition region **[12]**.

4.3 Results and discussions

In **Figure 4.1(A)**, we have plotted resistivity as a function of temperature of pure $YBa_2Cu_3O_{7-\delta}$ with nominal values of $\delta \sim 0$ (**S9**), 0.1 (**S10**), 0.3 (**S11**) and 0.5 (**S12**). Normal states of all pure samples are found to be metallic. Using $d\rho/dT$ versus T plots as shown in **Figure 4.3(A–D)** we obtain the critical temperature. It is taken as the temperature at which $d\rho/dT$ changes abruptly in lowering T from the normal state. T_c onset are found to be 89.8 K, 88.5 K, 90.5 K and 90.0 K corresponding to **S9**, **S10**, **S11** and **S12** respectively. In **Figure 4.1(B)**, we have shown the variation of resistivity as a function of temperature for all four

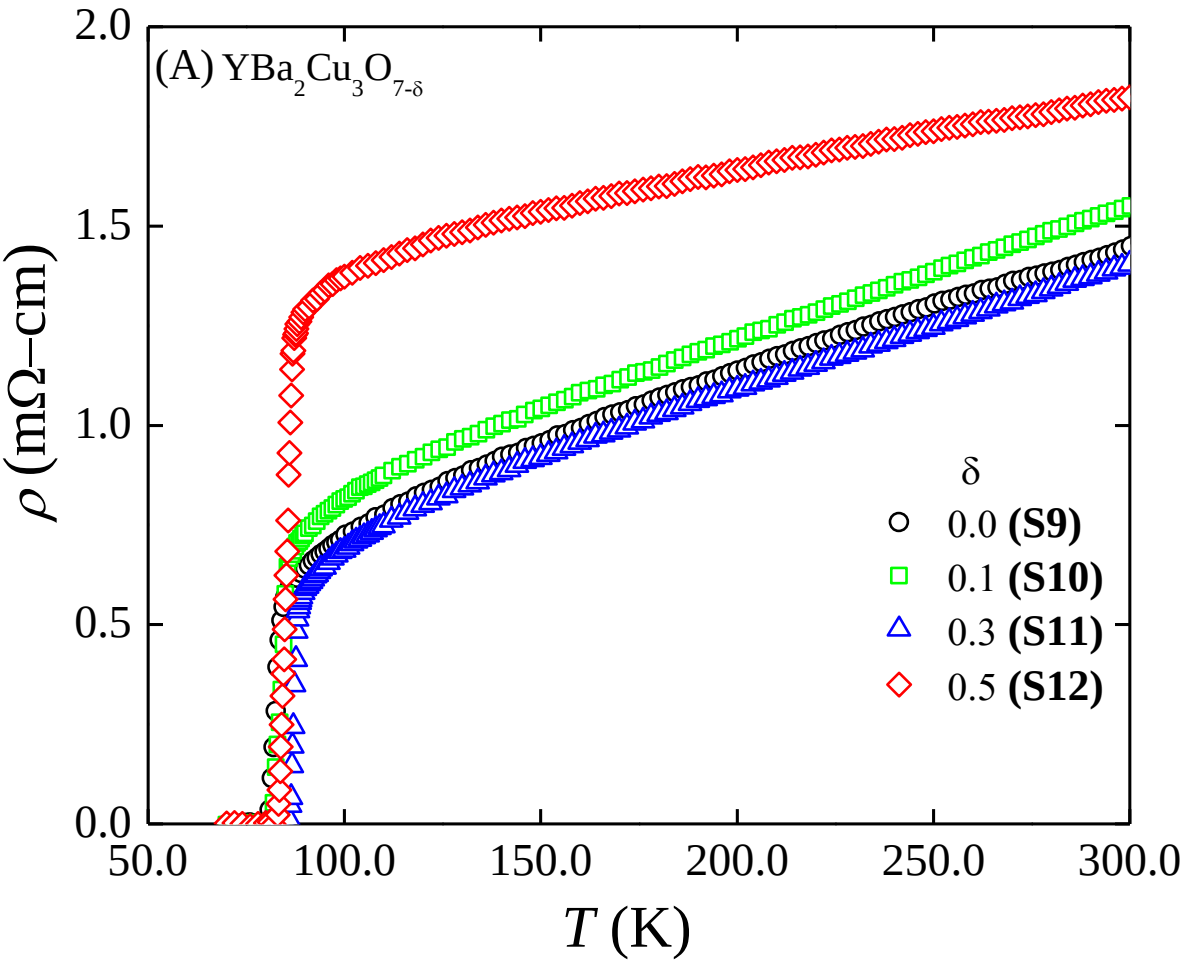

Figure 4.1(A): Resistivity as a function of T in$YBa_2Cu_3O_{7-\delta}$ (**S9 – S12**).

composite samples. Composite samples with 5% YCMO have higher ρ (300 K). We have plotted $d\rho/dT$ versus T in panels (A−D) corresponding to **S13**, **S14**, **S15** and **S16** in **Figure 4.4(A−D)**. T_c onset are found to be 66.3 K, 67.1 K, 67.8 K and 83.0 K corresponding to composite samples **S13**, **S14**, **S15** and **S16** respectively. Reduction of T_c in sample with $\delta \sim 0$ and 5% YCMO is maximum and it is about 23.5 K. In **Figure 4.2**, we have shown a typical SEM of a composite sample as a representative. In addition, it will be important to mention that the inter-granular networks are almost similar in nature in all (**S9−S16)** samples.

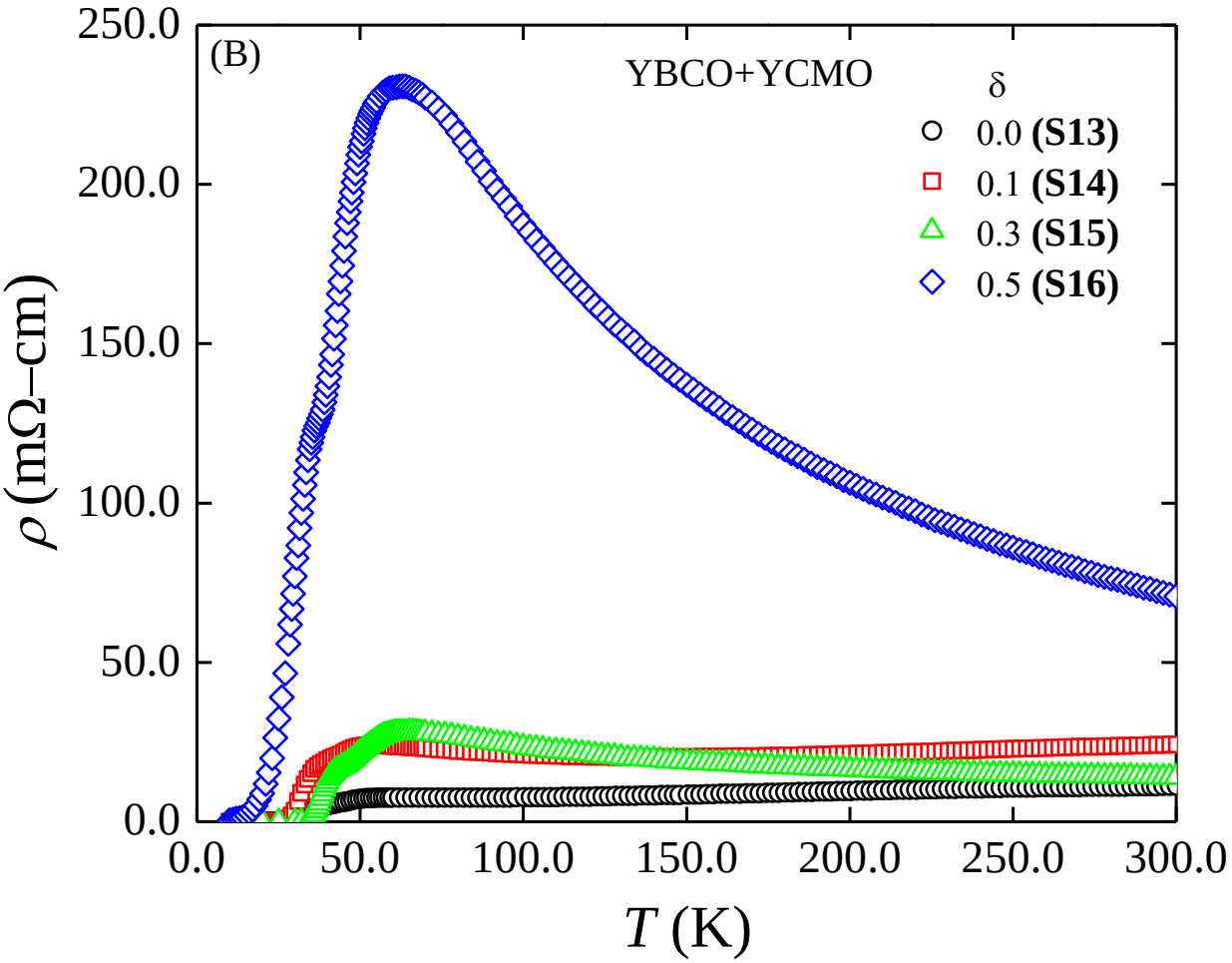

Figure 4.1(B): Resistivity as a function of T of four composite samples consisting of 5% Y_2CoMnO_6 and $YBa_2Cu_3O_{7-\delta}$ (**S13 – S16**).

Normal states and phase transition regions are clearly affected in all four composite samples. Comparing **Figure 4.1(A)** and **Figure 4.1(B)**, few major changes are observed in mixed samples. Even though the normal state of sample with $\delta = 0$ and its corresponding mixed sample remains metallic, a clear upturn in $\rho(T)$ becomes visible in other mixed samples. Sample with $\delta = 0.1$ and mixed with YCMO, normal state exhibits metallic behaviour over a wide range of temperature followed by a saturation in $\rho(T)$ in the vicinity of 150 K. However,

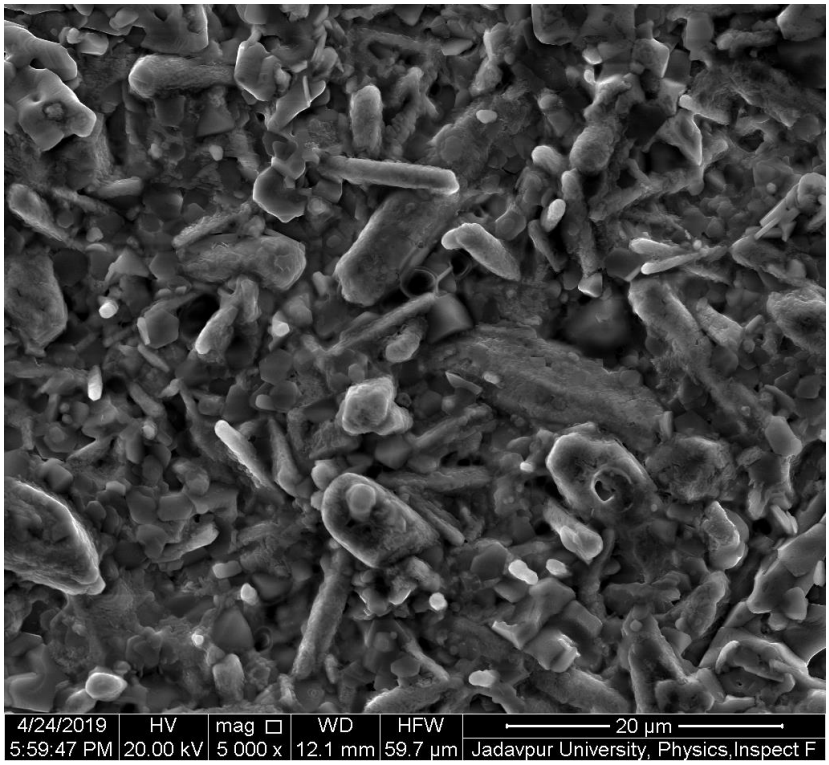

Figure 4.2: A representative SEM of the surface of the composite consisting of YCBO and YCMO (**S13**).

starting at 125.0 K a slight upturn has been observed in the mixed sample having $\delta = 0.1$. Mixed samples with $\delta = 0.3$ and $\delta = 0.5$ exhibit clear upturn starting at $T = 300.0$ K. Therefore, it is clearly observed that mixing is very effective in the range of $0.1 < \delta < 0.3$ in the origin of the upturn in $\rho(T)$. In addition, mixed sample with $\delta = 0.5$ exhibits very high resistivity ρ (300 K) ~ 73.5 mΩ-cm and superconducting transition.

Phase transition regions in both the pure samples and composite samples have been investigated by studying the usual variations in $d\rho/dT$ as a function of T.

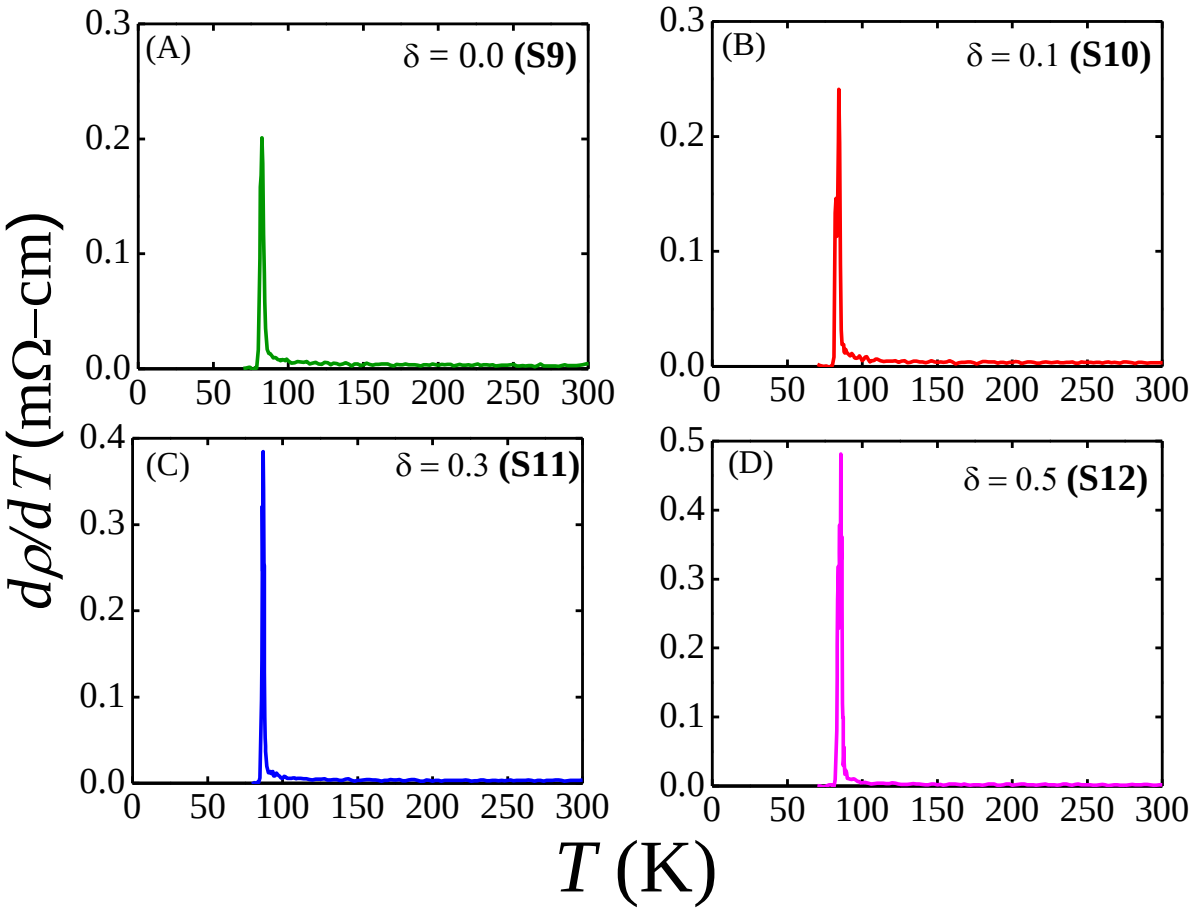

Figure 4.3(A–D): Variation of $d\rho/dT$ versus T in $YBa_2Cu_3O_{7-\delta}$ (**S9 – S12**).

However, we have observed some remarkable features. Firstly, in the pure sample with δ = 0.0, $d\rho/dT$ as a function of T exhibits a single peak at T = 82.5 K and corresponding values of $d\rho/dT$ = 0.19 mΩ - cm/K. For the pure sample with δ = 0.1, we observe a peak $d\rho/dT$ = 0.24 mΩ - cm/K at T = 84.4 K. An enhanced peak of $d\rho/dT$ = 0.38 mΩ - cm/K at T = 86.9 K for the sample with δ = 0.3 has been observed. The highest value of $d\rho/dT$ = 0.47 mΩ - cm/K has been observed in sample with δ = 0.5 and it is around T = 85.6 K. Clearly in pure samples the maximum value of $d\rho/dT$ increases with the increase in δ. It is an indication of how the phase transition gets affected with the variation of δ.

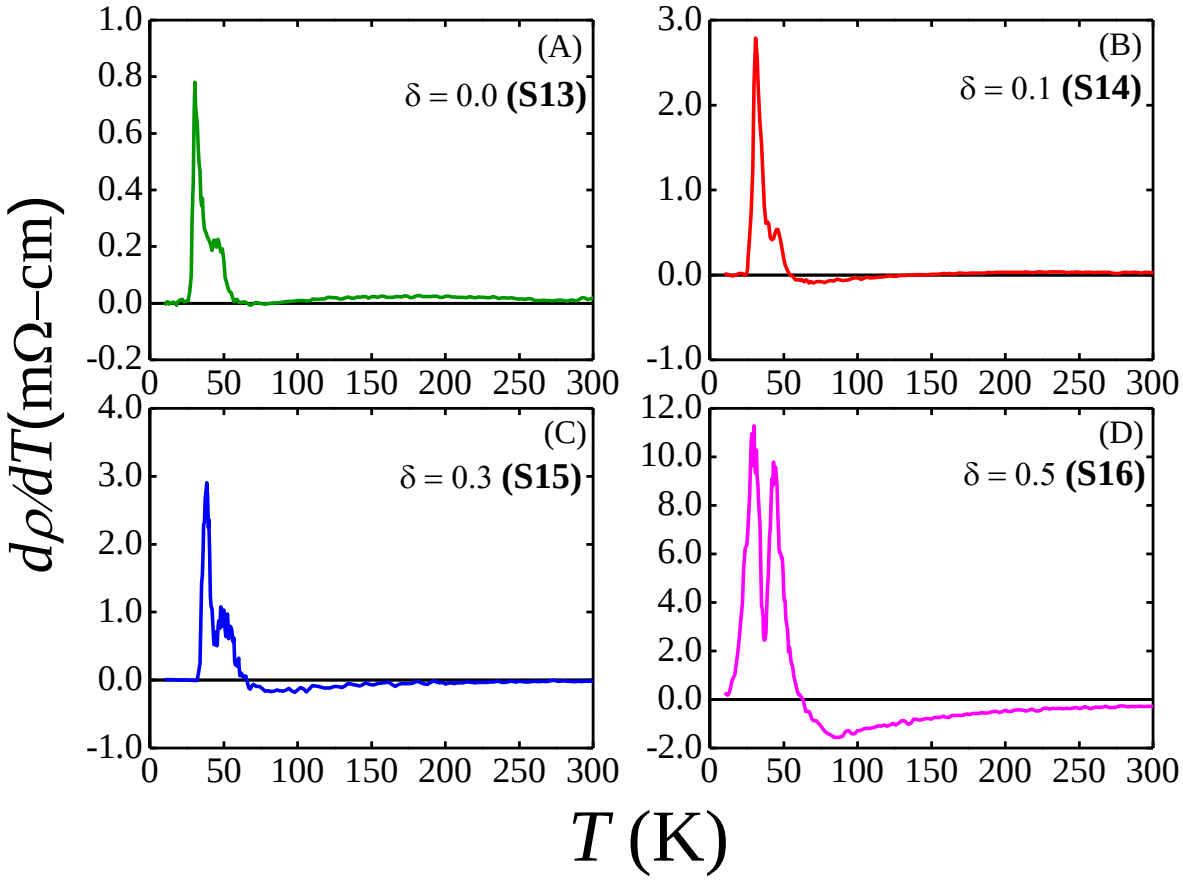

Figure 4.4(A−D) Variation of $d\rho/dT$ versus T in four composite samples consisting of 5% Y_2CoMnO_6 and $YBa_2Cu_3O_{7-\delta}$ (**S13 – S16**).

Variation of $d\rho/dT$ versus T in composite samples is very important to understand the role of the YCMO in the phase transition region. Following **Figure 4.4(A−D)**, $d\rho/dT$ versus T of composite sample **S13** exhibit a peak at T = 30.4 K and the peak value of $d\rho/dT$ is 0.77 mΩ - cm/K. In addition, there is a saturation with $d\rho/dT$ ~ 0.22 mΩ - cm/K a small region around T = 45.0 K. In the composite sample **S14** (with δ = 0.1) there is a peak in $d\rho/dT$ (T) at T = 31.3 K and peak value of $d\rho/dT$ is 2.75 mΩ - cm/K. It is also observed that the saturation in $d\rho/dT$ weakens around 0.51 mΩ - cm/K indicating origin of the another peak. There is

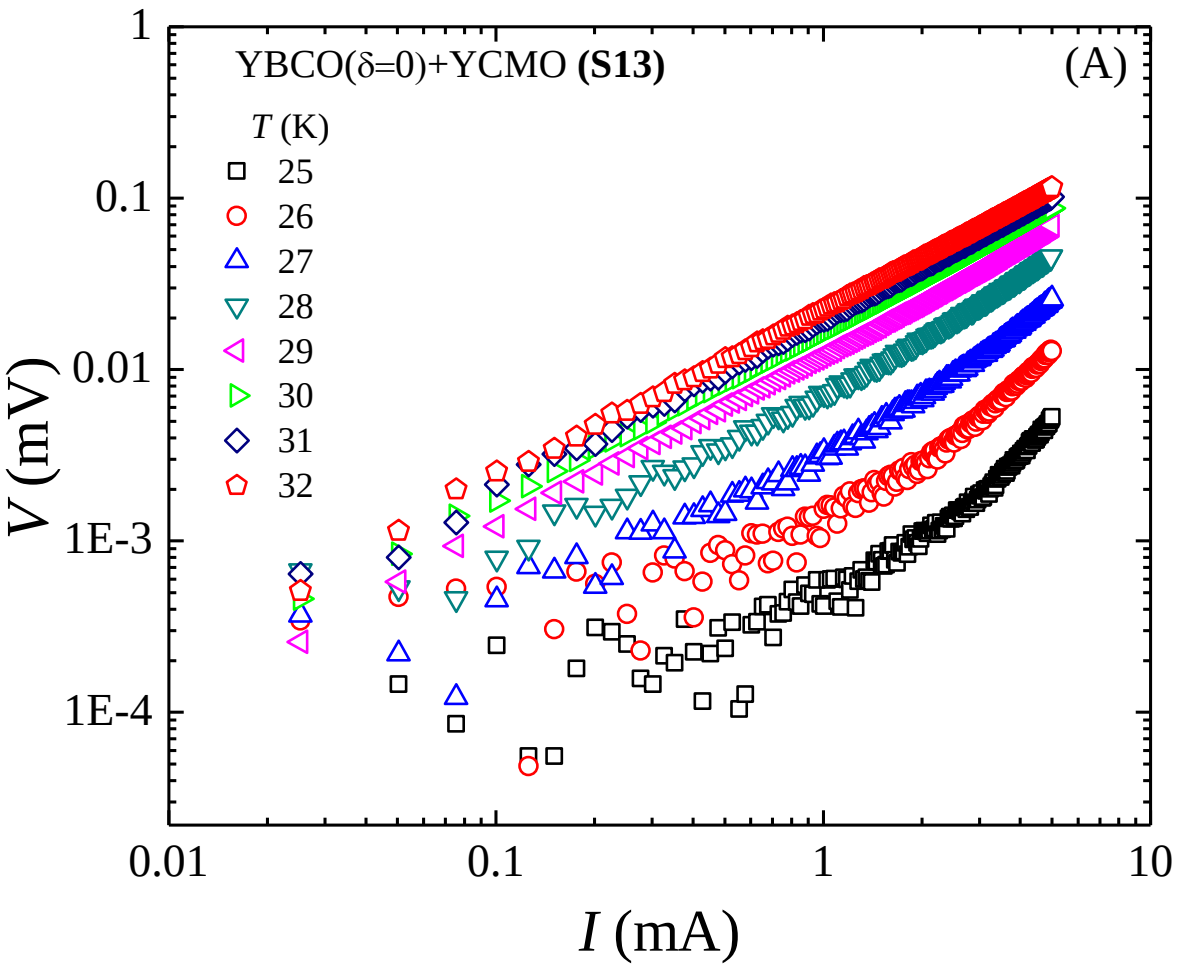

Figure 4.5(A): *IV* variations of a composite sample consisting of 5% Y_2CoMnO_6 and $YBa_2Cu_3O_{7.0}$ (**S13**).

a clear oscillating nature in $d\rho/dT$ (T) in the range of T = 44.8 K to 57.0 K in the composite sample **S15** with δ = 0.3. A clear peak is visible at T = 38.3 K with a value of $d\rho/dT$ ~ 2.85 mΩ - cm/K in **S15**. In the composite sample **S16** we observed two prominent peaks in $d\rho/dT$ (T) at T = 43.7 K and 28.7 K corresponding to the peak values 9.58 mΩ - cm/K and 10.76 mΩ - cm/K respectively. Therefore, the evolution of the nature of the phase transition in composite samples in presence of YCMO needs more insight.

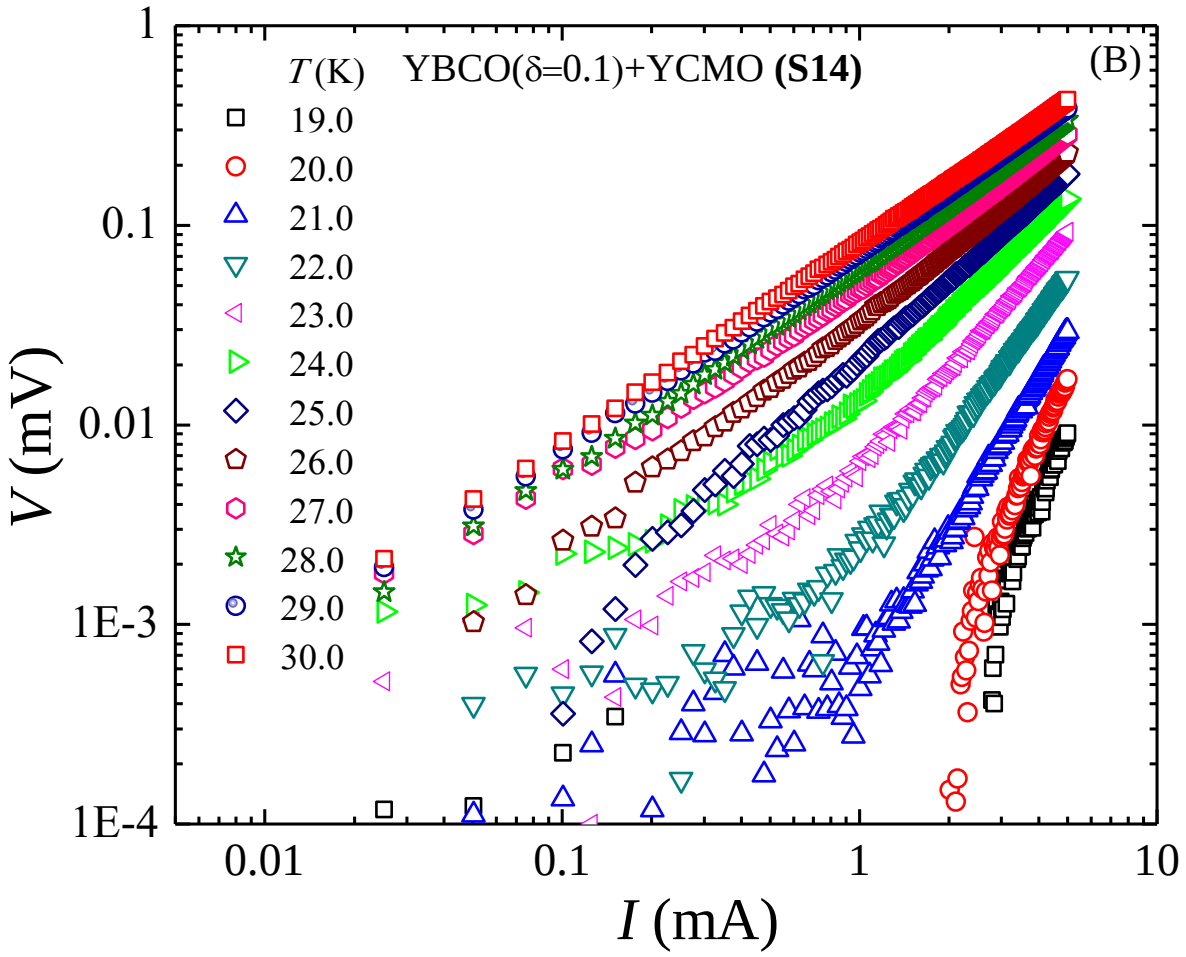

Figure 4.5(B): *IV* variations of a composite sample consisting of 5% Y_2CoMnO_6 and $YBa_2Cu_3O_{6.9}$ (**S14**).

There are several methods to estimate the σ_s in cuprate superconductors **[13, 14]**. Below the critical temperature variations of *IV* represent the SPS which is related to the vortex density correlations **[15]**. In **Figure 4.5(A–D)**, we have shown *IV* characteristics at several temperatures for four composite samples. In **Figure 4.5(A)** we have plotted *IV* for composite sample **S13**. It is observed that the *IV* curves are nonlinear in nature below T = 35.0 K. At T > 35.0 K, all *IV* curves are linear in nature. It will be interesting to mention that the sample **S9** without

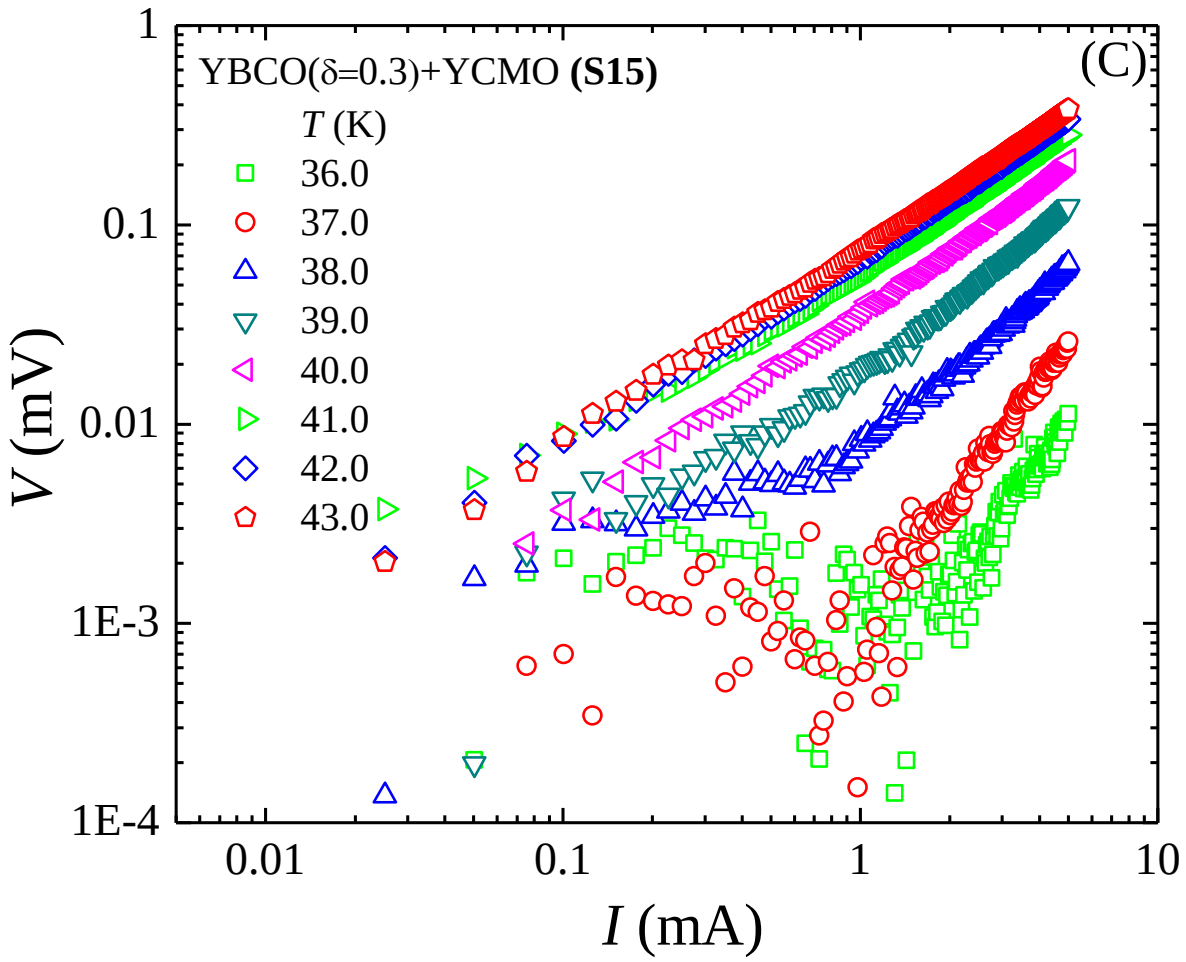

Figure 4.5(C): *IV* variations of a composite sample consisting of 5% Y_2CoMnO_6 and $YBa_2Cu_3O_{6.7}$ (**S15**).

YCMO exhibits no detectable nonlinear nature in *IV* even in the lowest temperature. There may be several reasons for the origin of the nonlinearity in *IV*. Generally, the granularity is cited as one of the reasons. However, there is no observed nonlinear behavior in the granular pure YBCO sample. That is why we exclude granularity as one of the reasons. In addition, we have studied the superfluid behavior for which we need to understand the nonlinearity observed in the composite systems. Therefore, it will be reasonable to say that the presence

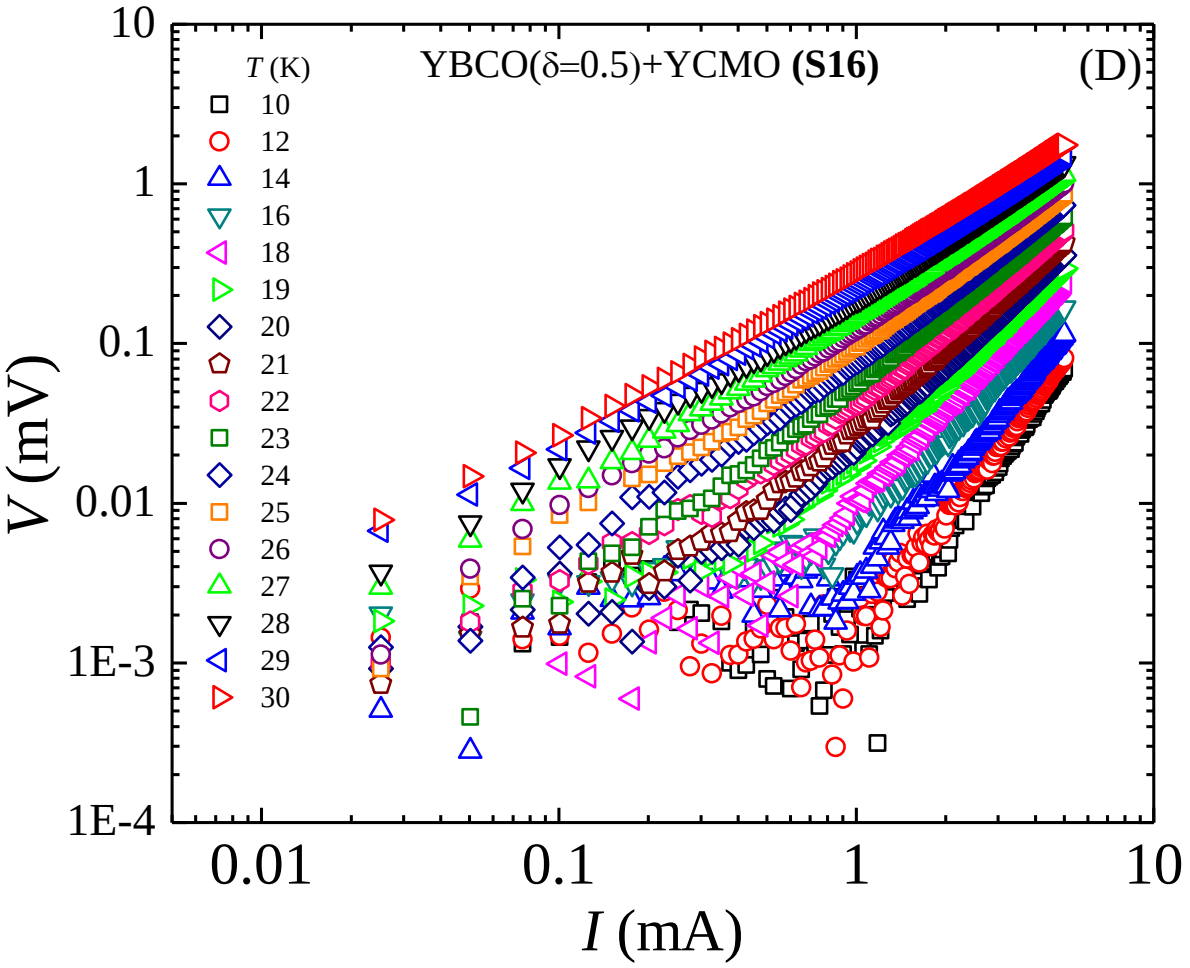

Figure 4.5(D): *IV* variations a composite sample consisting of 5% Y_2CoMnO_6 and $YBa_2Cu_3O_{6.5}$ (**S16**).

of YCMO generates nonlinear nature of *IV* in lower temperatures in **S13**. Similarly, following **Figure 4.5(B–D)** for composite samples **S14**, **S15** and **S16**, nonlinear natures in *IV* have been observed below T = 30.0 K, 40.0 K and 40.0 K respectively.

Following BKT transition several types of phase transitions have been explained including superconducting systems **[1, 15]**. The unbinding of vortex pairs above

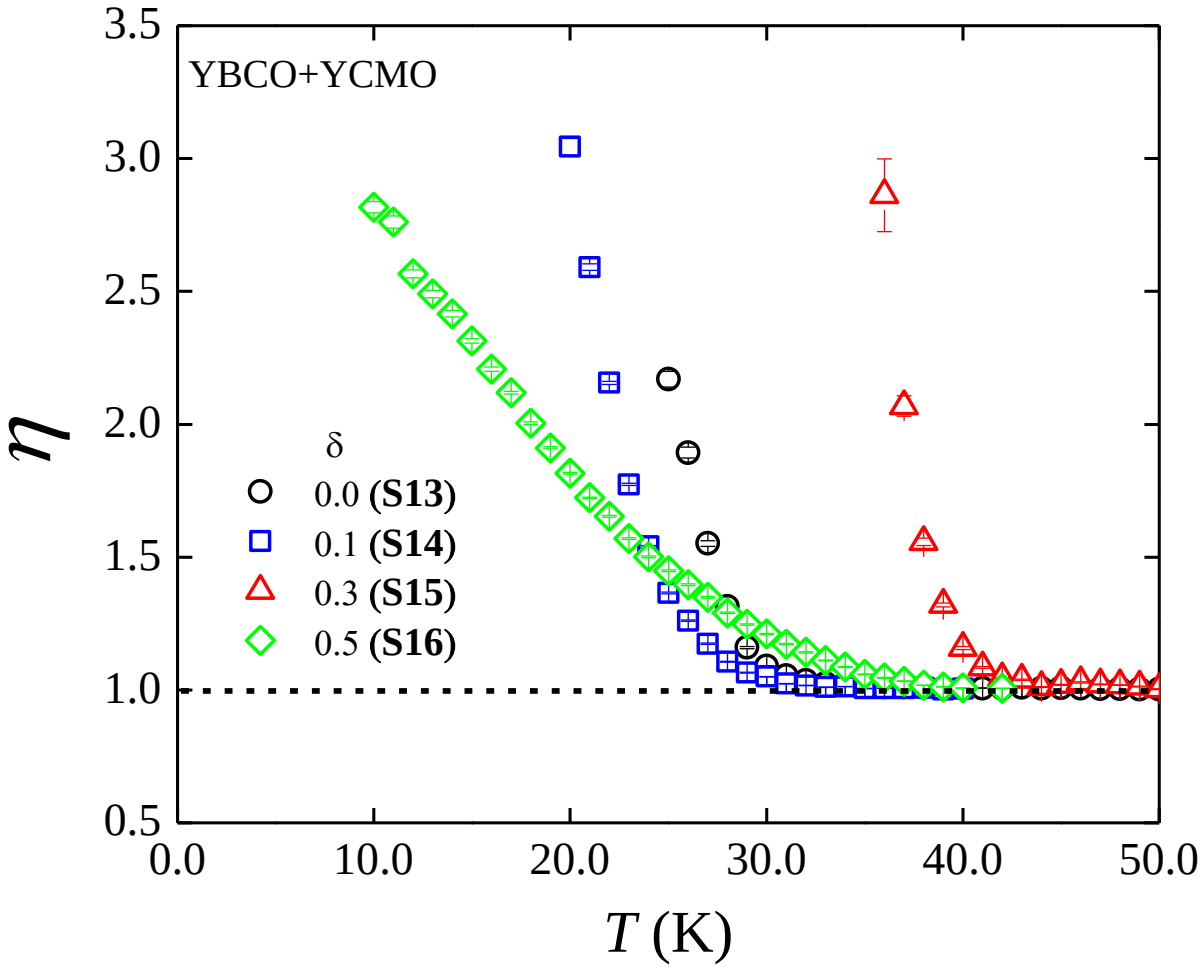

Figure 4.6(A): Variation of a exponent η with the temperature in composite samples **S13-S16**.

the BKT transition temperature has been used to understand the nonlinear *IV* below the superconducting critical temperature. In the origin of the nonlinear nature of *IV*, the role of YCMO has been considered following the idea of the BKT transition **[1]**. The nonlinear voltage can be expressed with the help of an exponent η and corresponding expression for voltage drop is written in eqn **1.1** **[16-18]**. We have fitted *IV* curves by using the above formula and extracted η as a function of *T* for all four composite samples. In **Figure 4.6(A)**, we have shown

the variations of $\eta(T)$. Interestingly, the variation of the exponent with T has a nonlinear nature. All four composite samples have shown a drastic change in $\eta(T)$. The BKT transition is generally detected with the change in $\eta(T)$ from 3.0 to 1.0. Except in sample **S16**, all three samples exhibit a very sharp nature of the variation. However, **S16** shows a broader variation of $\eta(T)$. In the ultrathin layers of the superlattice structure, a broadened variation of the exponent has been observed earlier **[19]**. Nevertheless, the addition of YCMO in YBCO induces the nonlinearity in a wide range of the oxygen concentration of YBCO. Earlier in YBCO it has been reported that the nonlinearity may be observed in a very narrow range of temperature **[20-22]**. Absence of the BKT transition in YBCO thin film has been observed as well **[23]**. Even though we do not observe any nonohmic exponent in pure YBCOs, we have observed the nonohmic exponents for all the composite samples having the low concentration of YCMO. Following the AHNS theory, we have also extracted the $J_s(T)$ with the help of the equation **1.2** **[16, 17]**. The variations of $J_s(T)$ are shown in **Figure 4.6(B)**. The SPS becomes zero in all cases (composite samples, **S13-S16**) above a certain temperature which is much lower than the corresponding superconducting phase transition temperature. Nevertheless, for all pure YBCO samples (**S9-S12**), we observed $J_s(T) = 0$ at any temperature below the phase transition temperature.

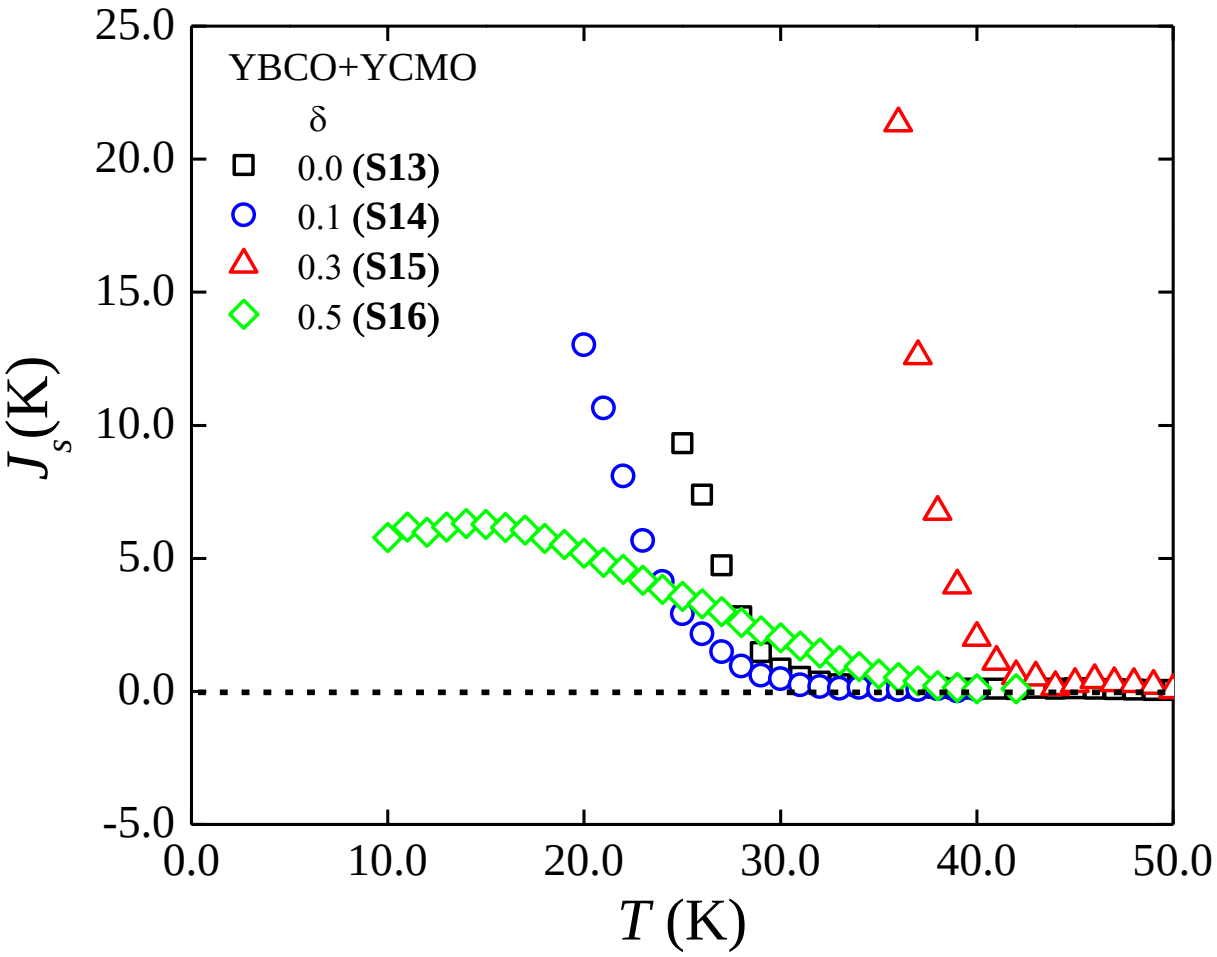

Figure 4.6(B): SPS as a function of *T* of composite systems (**S13-S16**) following AHNS theory using eqn **1.2**.

The pure YBCO exhibits no signature of the nonlinear behaviour in *IV*. As we add the lower concentration of YCMO the possibility of BKT transition becomes prominent. Therefore, the origin of such higher values of the exponent needs an explanation. The multiferroic YCMO exhibits ferromagnetic properties depending on the temperature. It will also be interesting to mention that YCMO has a very complex magnetic structure in the range of the temperature where the composite systems exhibit the nonlinear variation of the SPS **[24, 25]**. There is

an important idea according to which in a ferroelectric system, the BKT transition can be engineered [26] which seems to be very relevant to our observations of higher nonohmic exponent and σ_s. It seems that even a low dimensional thin layer of YCMO formed in the inter-granular networks between two superconducting grains of YBCO can be very effective to exhibit the BKT transition. The hybrid configuration may cause the higher values of the exponent and the nonlinearity in the $J_s(T)$ with the temperature.

4.4 Summary

The linear nature of the *IV* curves below the critical temperature in the pure YBCO system has been observed. On the addition of the low density YCMO in YBCO, the nature of *IV* curves becomes nonlinear in addition to the change in the critical temperature. The nonlinear nature of *IV* curves in composite systems exhibits wide variations. An increase in the exponent with the temperature indicates that the BKT transition may be observed as a result of the presence of the complex nature of the magnetic ordering or multiferroic layer in the inter-granular region. A hybrid system consisting of YBCO and YCMO may be the potential to observe the BKT transition.

4.5 References

[1] J. M. Kosterlitz, D. J. Thouless, J. Phys. C **6** (1973) 1181.

[2] V. L. Berezinskii, Zh. Eksp. Teor. Fiz **61** (1971) 1144.

[3] L. Benfatto, C. Castellani, T. Giamarchi, Phys. Rev. Lett. **98** (2007) 117008.

[4] P. G. Baity, X. Shi, Z. Shi, L. Benfatto, D. Popovi´c, Phys. Rev. B **93** (2016) 024519.

[5] S. Steers,T. R. Lemberger, J. Draskovic, Phys. Rev. B **94** (2016) 094525.

[6] J. Yong, M. J. Hinton, A. McCray, M. Randeria, M. Naamneh, A. Kanigel, T. R. Lemberger, Phys. Rev. B **85** (2012) 180507.

[7] B. Chattopadhyay, S. R. Shenoy, Phys. Rev. Lett. **72** (1994) 400.

[8] I. Hetel, T. R. Lemberger, M. Randeria, Nature **3** (2007) 400.

[9] I. Božović, X. He, J. Wu, A. T. Bollinger, Nature **536** (2016) 309.

[10] S. Mollah, B. Biswas, S. Haldar, A. K. Ghosh, Physica C **539** (2017) 40.

[11] B. Biswas, S. Haldar, I. Mukherjee, A. K. Ghosh, Physica B **506** (2017) 173.

[12] I. Mukherjee, S. Mollah, T. Sk, S. Haldar, A. K.Ghosh, Physica C **560** (2019) 67.

[13] D. M. Broun, W.A. Huttema, P.J. Turner, S. Ozcan, B. Morgan, Ruixing Liang, W.N. Hardy and D.A. Bonn, Phys. Rev. Lett. **99** (2007) 237003.

[14] C. Bernhard, Ch. Niedermayer, U. Binninger, A. Hofer, Ch. Wenger, J. L. Tallon, G. V. M. Williams, E. J. Ansaldo, J. I. Budnick, C. E. Stronach, D. R. Noakes, M. A. Blankson-Mills, Phys. Rev. B **52** (1995) 10488.

[15] P. Das, A. K. Ghosh, Physica C **548** (2018) 27.

[16] V. Ambegaokar, H. Halperin, D. Nelson, E. Siggia, Phys. Rev. Lett. **40** (1978) 783.

[17] V. Ambegaokar, H. Halperin, D. Nelson, E. Siggia, Phys. Rev. B **21** (1980) 1806.

[18] P. Minnhagen, O. Westman, A. Jonsson, P. Olsson, Phys. Rev. Lett. **74** (1995) 3672.

[19] D. P. Norton, D. H. Lowndes, Phys. Rev. B **48** (1993) 6460.

[20] P. C. E. Stamp, L. Forro, C. Ayache, Phys. Rev. B **38** (1988) 2847.

[21] M. Sugahara, M. Kojima, N. Yoshikawa, T. Akeyoshi, N. Haneji, Phys. Lett. A **125** (1987) 429.

[22] N.-C. Yeh, C. C. Tsuei, Phys Rev. B **39** (1989) 9708.

[23] J. M. Repaci, C. Kwon, Qi Li, X. Jiang, T. Venkatessan, R. E. Glover, C. J. Lobb, R. S. Newrock, Phys. Rev. B **54** (1996) R9674.

[24] J. Blasco, J. García, G. Subías, J. Stankiewicz, J. A. Rodríguez-Velamazán, C. Ritter, J. L. García-Muñoz, F. Fauth, Phys. Rev. B **93** (2016) 214401.

[25] T. Jia, Z. Zheng, X. G. Li, H. Q. Lin, J. Appl. Phys. **117** (2015) 17E119.

[26] Y. Nahas, S. Prokhorenko, I. Kornev, L. Bellaiche, Phys. Rev. Lett **119** (2017) 117601.

Chapter 5

Nonmagnetic scattering induced suppression of superfluid density in Bi-2212

5.1 Introduction

Increasing the SPS, an enhancement of the T_c in a superconductor is a very complex process. Beyond a maximum SPS, no further enhancement of T_c is possible in the HTS. However, it is not clear whether any critical SPS is there beyond which increasing SPS is no more effective in controlling T_c. The relation between the SPS and σ_s has been extracted in several superconducting systems **[1-10]**. Bi-2212 is such a superconducting 2D system in which SPS has been studied, the objective of which remains many **[11-14]**. An important direction is how to change SPS in Bi-2212 superconducting systems and understand the associated underlying mechanism **[15]**. Suppression of the SPS in Bi-2212 is also equally important which has added an additional direction in the same purpose and the area of investigation **[16]**.

The SPS in superconducting systems has been studied by using several experimental methods [17-21]. With the increase in T, the suppression of the SPS in cuprates including Bi-2212 follows a crossover from the linear to a nonlinear T-dependence [22]. In addition, depending on the carrier doping, the T-dependence of the SPS is affected in different ways [23]. As an origin of the superconducting pairs, any substitution of the impurity (doping) in Cu site affects T_c strongly. Even though the SPS at absolute zero (T = 0) is said to be scales linearly below the quantum critical point (QCP), T-variation of the SPS reveals how the σ_s varies in such superconducting systems. *IV* characteristics below T_c are found to be very effective to extract the SPS in such systems [24, 25].

Nonmagnetic Zn-doped Bi-2212 is such a system in which the nonmagnetic impurity suppresses superconductivity strongly. The suppression of T_c is reported to be caused by the local suppression of the superconductivity by the strong scattering [26, 27]. In presence of such a strong local scattering ambience around the nonmagnetic site, how the SPS is affected in Bi-2212 is our main objective. For the first time, we have investigated how the SPS varies with T in the pure Bi-2212 by using *IV* characteristics. In the presence of the nonmagnetic impurity Zn replacing Cu, how the nonlinear T - dependence of the SPS is affected is investigated for the first time by using *IV* at the zero magnetic field. The *IV* characteristics below T_c of several $Bi_2Sr_2CaCu_{2-x}Zn_xO_{8+\delta}$ superconductors have

been investigated to extract $J_s(T)$ following AHNS theory **[28, 29]**. An idea associating the phase fluctuations in the distribution of the BKT vortices in strong scattering potential has been used to understand the $J_s(T)$ in presence of nonmagnetic Zn in $Bi_2Sr_2CaCu_{2-x}Zn_xO_{8+\delta}$ **[30-32]**.

5.2 Experimental

We have synthesized several $Bi_2Sr_2CaCu_{2-x}Zn_xO_{8+\delta}$ (Bi-2212) superconducting bulk samples by using the standard solid state reaction method **[33, 34]**. The concentration of Zn, x is taken to be 0 (**S17**), 0.05 (**S18**), 0.10 (**S19**), 0.15 (**S20**) and 0.20 (**S21**). Sintering temperature have been used to synthesize the above sample in the range of 820°C - 840° C and the duration is about 60 hours. In the inset of **Figure 5.1**, we have shown a typical bar-shaped sample used for the transport measurements. Typical dimension of the bar-shaped sample is 6.5 × 2.5 × 0.5 mm^3. The resistivity (ρ) as a function of T has been measured by using the standard four-probe method with the help of a cryogenerator **[35, 36]**. At constant T below the onset T_c, the measurements of IV have been carried around the phase transition region. Generally, there are several criteria for determining critical current, I_c from IV. We have used a criterion E = 0.01 mV/cm for the determination of critical current I_c. The critical current in the pure Bi-2212 is found to be about 3.7 mA at 60.0 K.

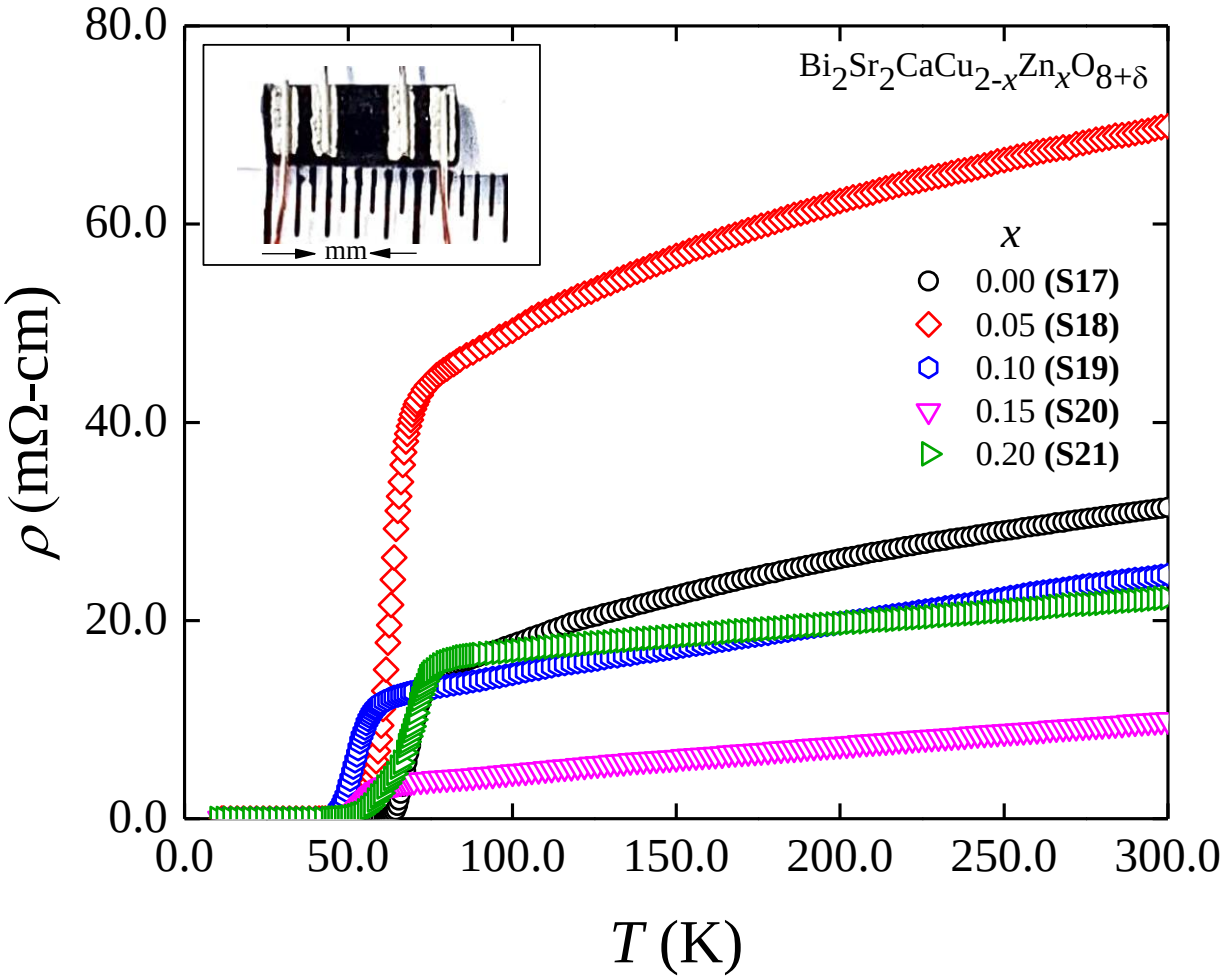

Figure 5.1: Resistivity, ρ as a function T in $Bi_2Sr_2CaCu_{2-x}Zn_xO_{8+\delta}$ (**S17 – S21**).

5.3 Results and discussions

We have shown the resistivity, ρ, as a function of T in $Bi_2Sr_2CaCu_{2-x}Zn_xO_{8+\delta}$ superconductors in **Figure 5.1**. ρ (T) corresponding to the normal states of all samples are found to be metallic in nature. In **Figure 5.2(A-E)**, $d\rho/dT$ as a function of T has been plotted for the samples (**S17** – **S21**). The superconducting onset T_c are found to be 83.2 K, 78.0 K, 70.0 K, 72.0 K and 82.0 K corresponding to x = 0, 0.05, 0.10, 0.15 and 0.20 respectively. Even though the temperature

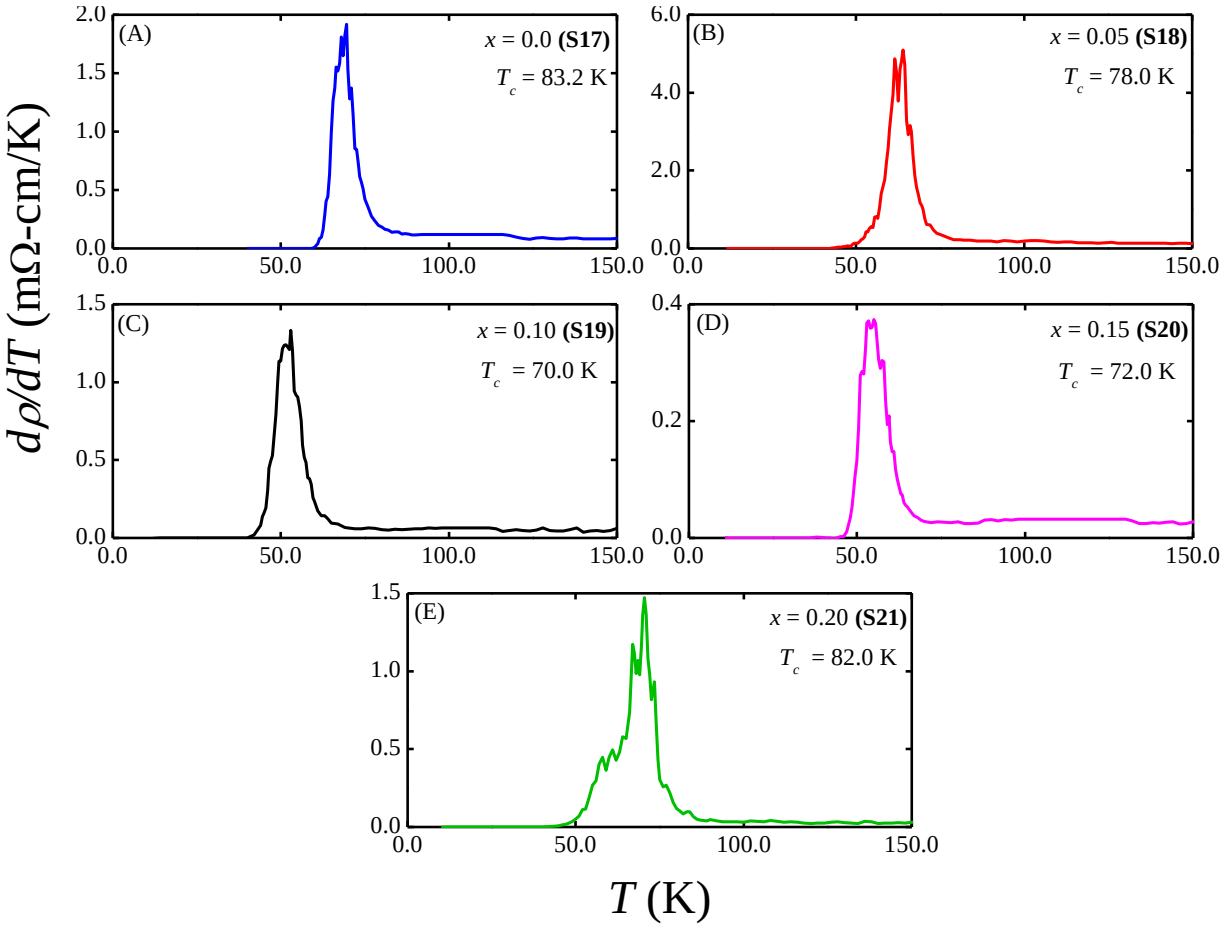

Figure 5.2(A-E) Variations of $d\rho/dT$ versus T in $Bi_2Sr_2CaCu_{2-x}Zn_xO_{8+\delta}$ for (A) x = 0 (**S17**), (B) x = 0.05 (**S18**), (C) x = 0.10 (**S19**), (D) x = 0.15 (**S20**), and (E) x = 0.20 (**S21**).

dependence of in-plane resistivity, ρ_{ab} and out-of-plane resistivity, ρ_c are known to be highly anisotropic in nature in Bi-2212 single crystal, T_c is found to be almost the same in both $\rho_{ab}(T)$ and $\rho_c(T)$ **[37,38]**. The effect of the nonmagnetic Zn in the bulk Bi-2212 is very complex in nature because of the randomness in induced scattering centres in the superconducting planes. It is observed that above a certain concentration, the effectiveness of Zn in the formation of energy gap

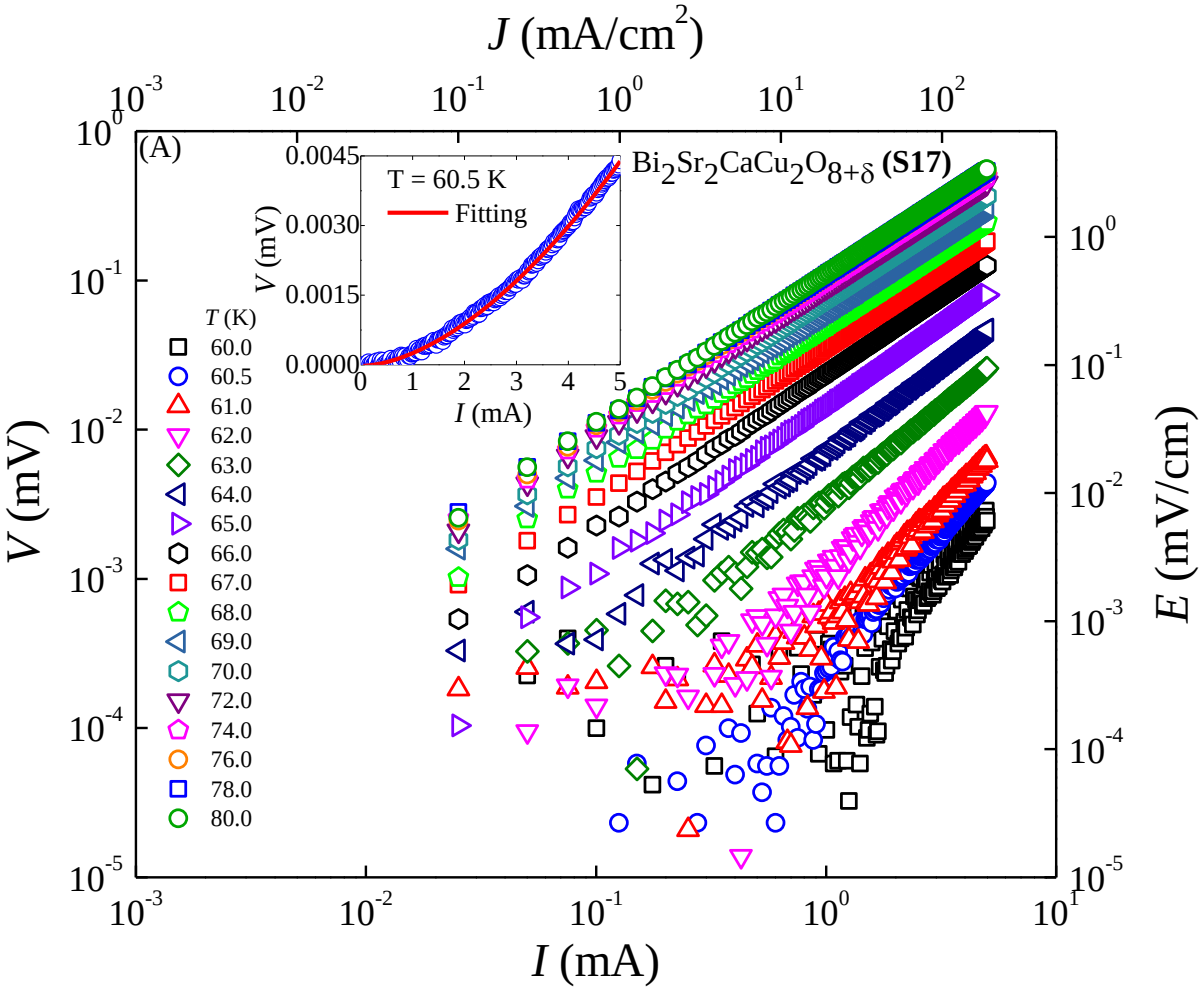

Figure 5.3(A): *IV* characteristics in the *log-log* scale in superconducting $Bi_2Sr_2CaCu_2O_{8+\delta}$ **(S17)** at several temperatures. An inset shown a nonlinear curve of the respective sample with a fitting line by using eqn **1.1**.

remains almost unchanged **[39]**. Even though Zn suppresses T_c it is known that the suppression of order parameters takes place locally. Because all samples are in the optimally doped region, the suppression of T_c is not strong enough. Adjusting the excess oxygen contributed a number of holes T_c may remain almost unchanged even though locally Zn suppresses superconducting order parameters.

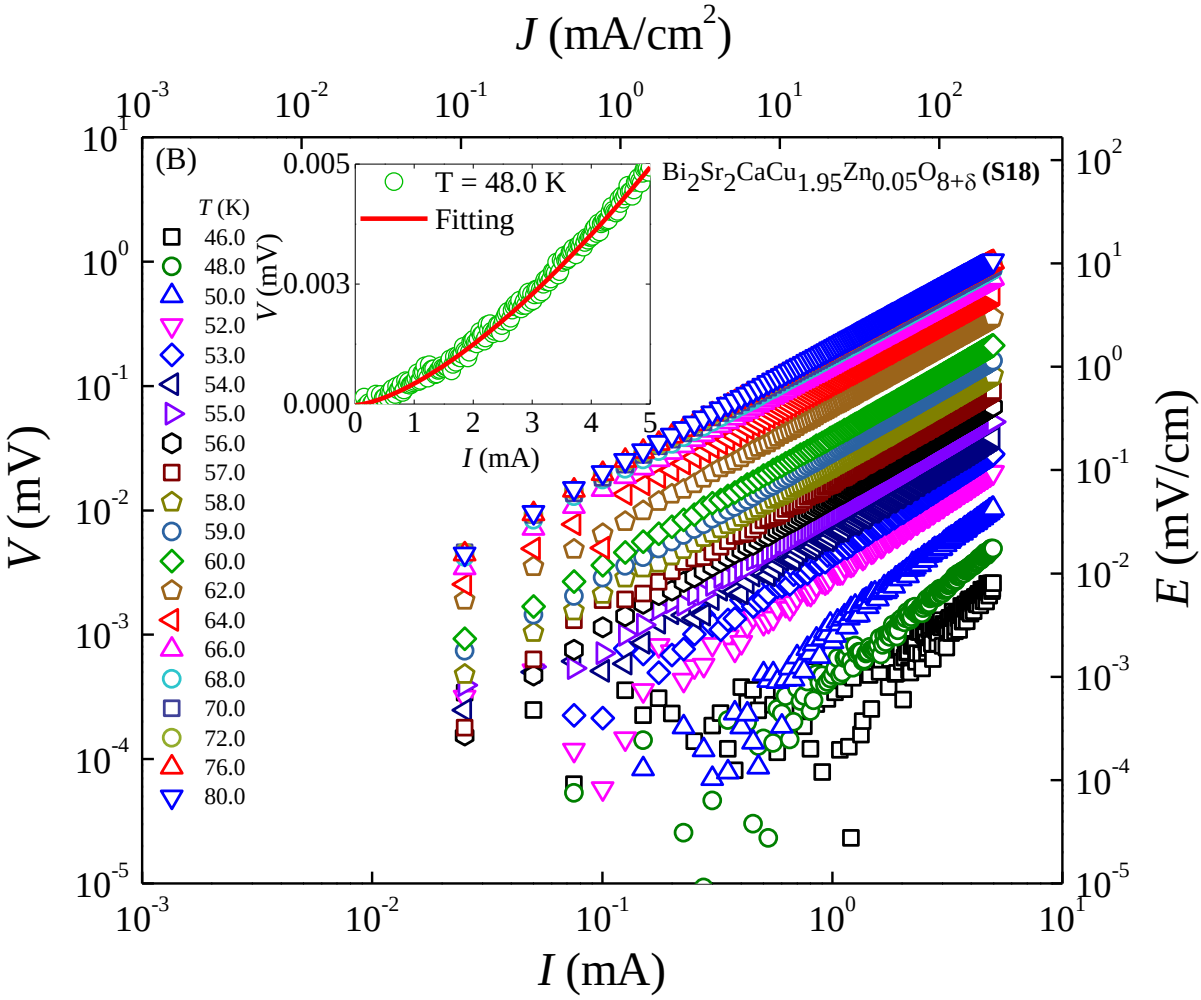

Figure 5.3(B): *IV* characteristics in the *log-log* scale in superconducting $Bi_2Sr_2CaCu_{1.95}Zn_{0.05}O_{8+\delta}$ **(S18)** at several temperatures. An inset shown a nonlinear curve of the respective sample with a fitting line by using eqn **1.1**.

The σ_s controls critical temperatures in a complex way in Bi-2212. Both the linear ($T_c \propto \sigma_s$) and nonlinear (for example, $T_c \propto \sigma_s^{½}$) relations between the T_c and the σ_s are reported in several cuprate superconductors **[40]**. However, any relation between the critical temperature, T_c ($\rho \approx 0$) and σ_s (J_s) in Zn-doped Bi-2212 is not known **[41]**.

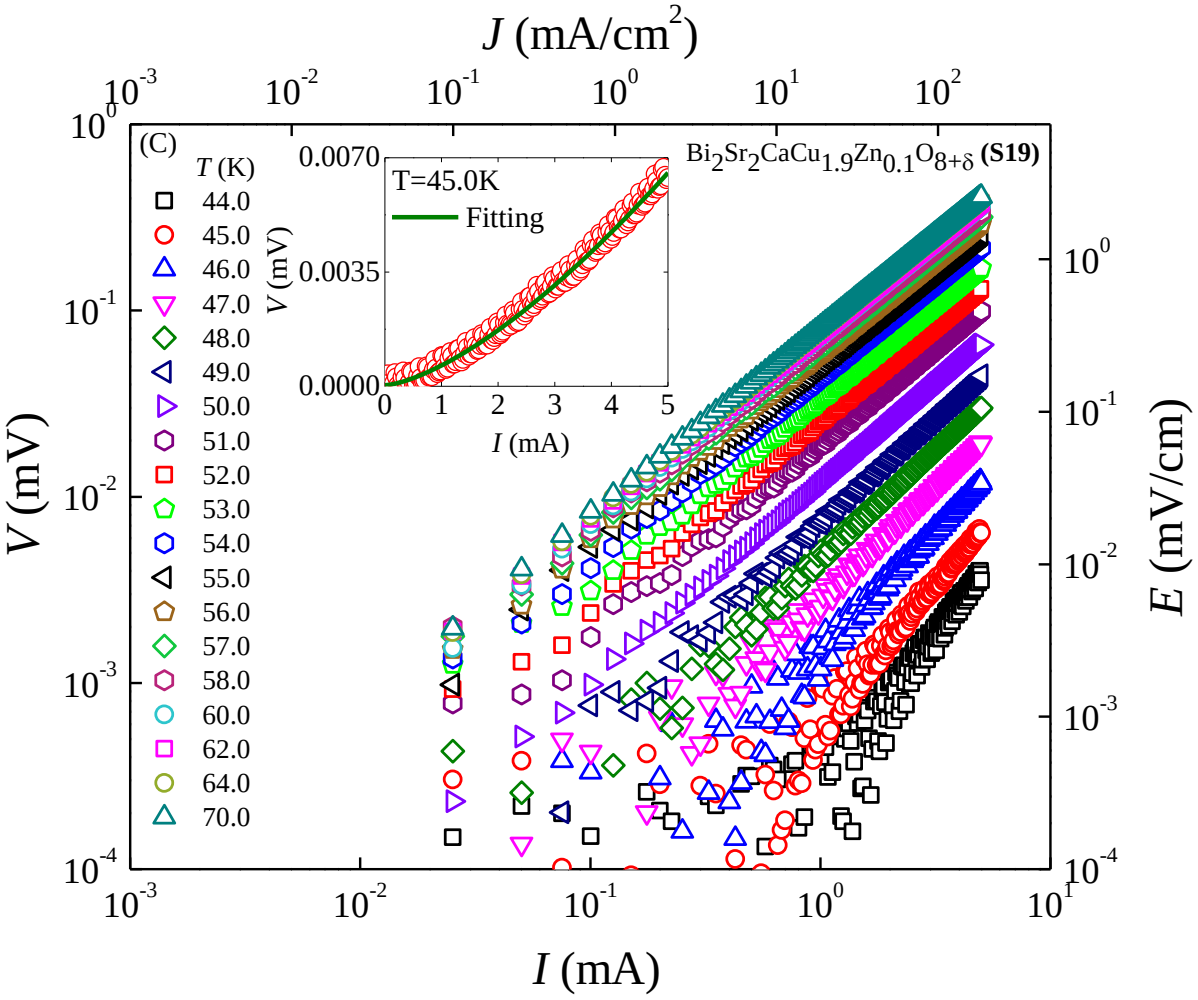

Figure 5.3(C): *IV* characteristics in the *log-log* scale in superconducting $Bi_2Sr_2CaCu_{1.9}Zn_{0.1}O_{8+\delta}$ **(S19)** at several temperatures. An inset shown a nonlinear curve of the respective sample with a fitting line by using eqn **1.1**.

In **Figure 5.3(A-E)** we have shown *IV* characteristics at several temperatures for all five samples (**S17-S21**) together with the corresponding electric field (*E*) and current density (*J*). In the pure Bi-2212 sample with (x = 0), the *IVs* as shown in **Figure 5.3(A)** are found to be nonlinear in the range of 60.0 K to 66.0 K. In the

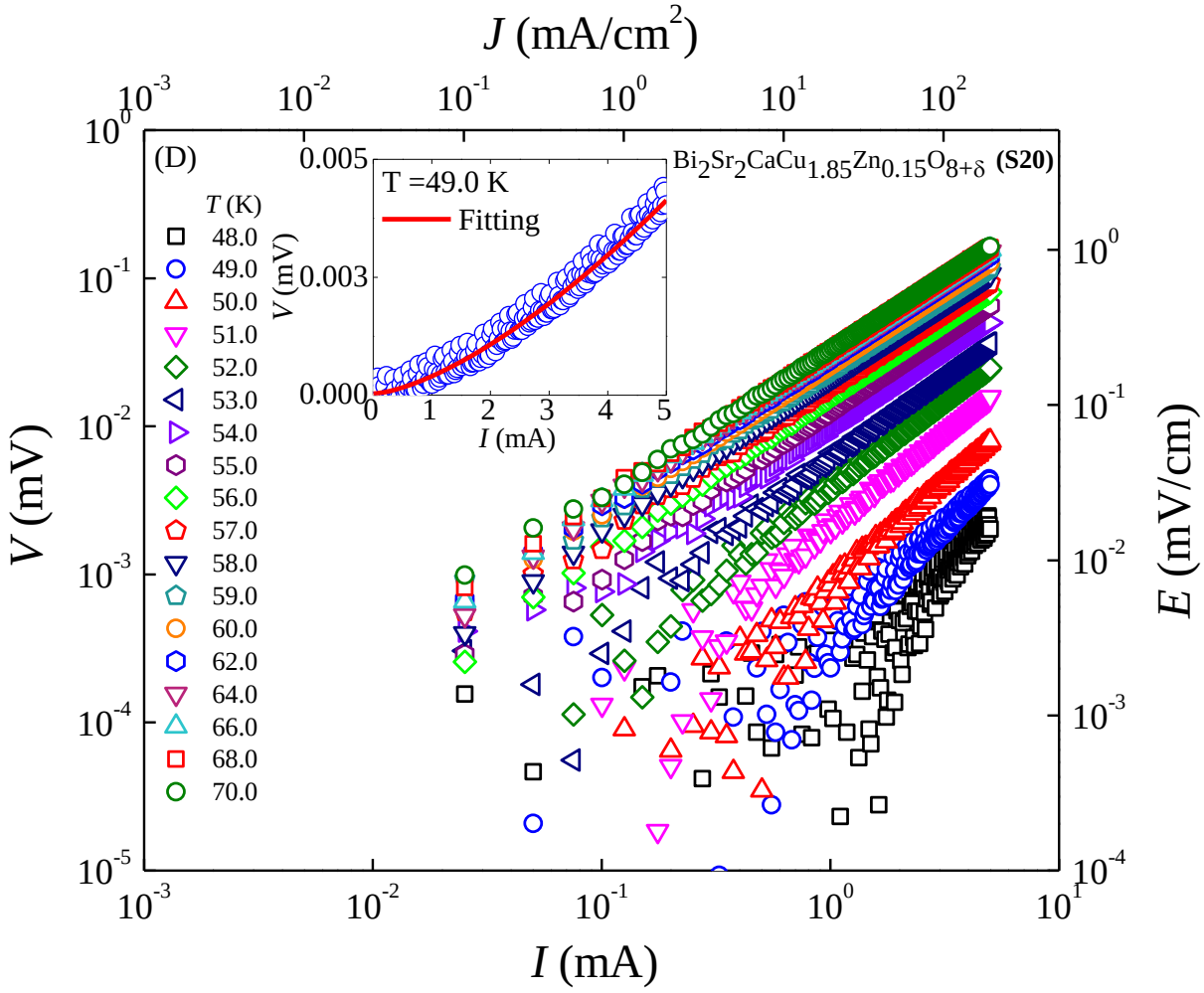

Figure 5.3(D): *IV* characteristics in the *log-log* scale in superconducting $Bi_2Sr_2CaCu_{1.85}Zn_{0.15}O_{8+\delta}$ **(S20)** at several temperatures. An inset shown a nonlinear curve of the respective sample with a fitting line by using eqn **1.1**.

inset of **Figure 5.3(A)**, we have plotted a typical nonlinear *IV* at 60.5 K. In **Figure 5.3(B)** we have shown *IV* characteristics in the range of 46.0 K through 80.0 K for the sample **S18**. A representative nonlinear *IV* curve corresponding to T = 48.0 K is shown in the inset of **Figure 5.3(B)**. We have shown the nonlinear variation of *IV* in the range of 44.0 K to 70.0 K for **S19** with x = 0.10 in **Figure 5.3(C)**. A

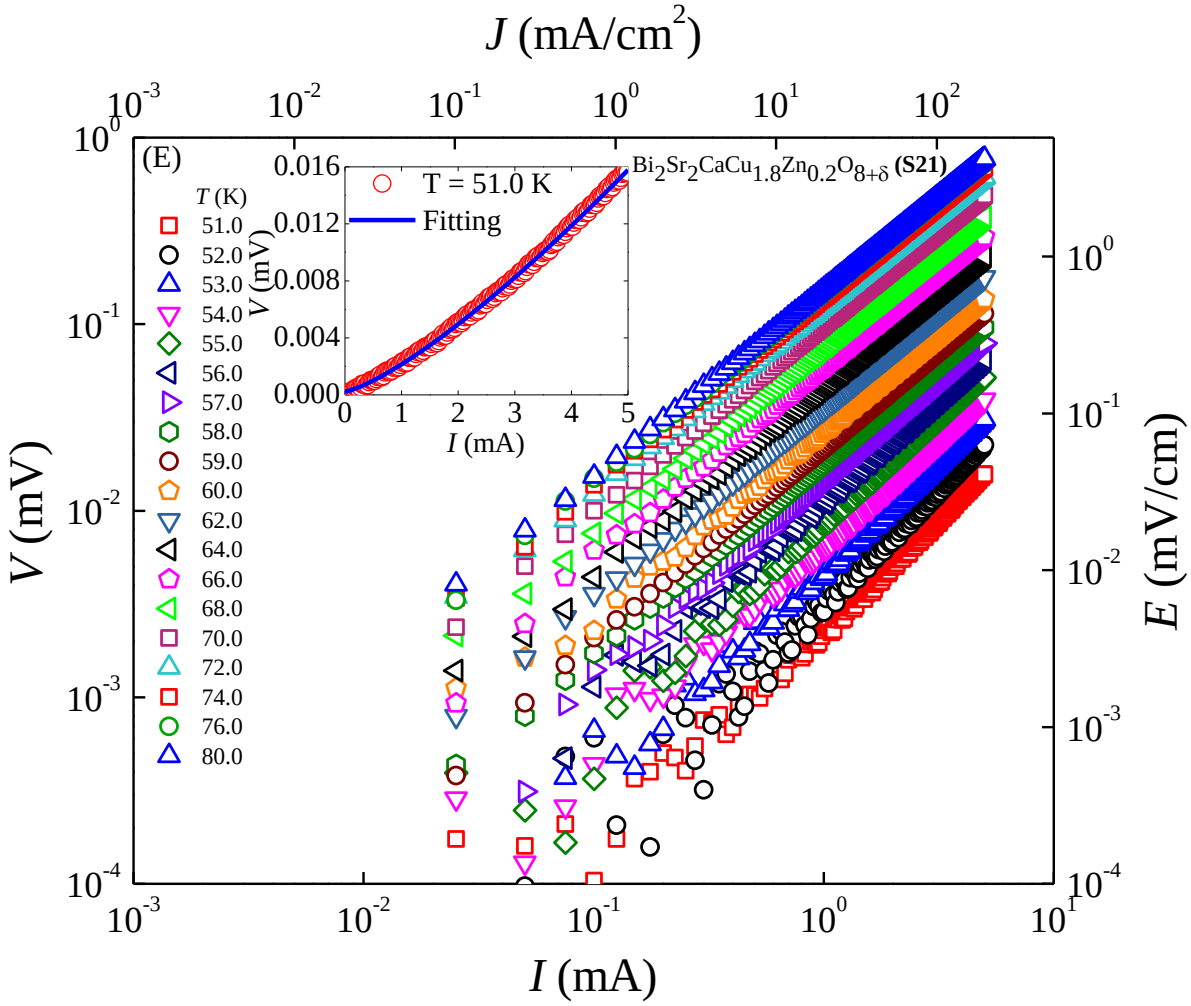

Figure 5.3(E): *IV* characteristics in the *log-log* scale in superconducting $Bi_2Sr_2CaCu_{1.8}Zn_{0.2}O_{8+\delta}$ **(S21)** at several temperatures. An inset shown a nonlinear curve of the respective sample with a fitting line by using eqn **1.1**

typical nonlinear *IV* corresponding to T = 45.0 K has been shown in the inset of **Figure 5.3(C)**. For **S20** with x = 0.15, the *IV* characteristics in the range of 48.0 K to 70.0 K are shown in **Figure 5.3(D)**. In the inset of **Figure 5.3(D)**, we have plotted a typical nonlinear *IV* characteristic at T = 49.0 K. We have shown the *IV* characteristics for **S21** (x = 0.20) in **Figure 5.3(E).** A typical nonlinear *IV*

variation is shown in the inset of **Figure 5.3(E)** at temperature T = 51.0 K. Therefore, below the onset superconducting T_c, the *IV* characteristics exhibit similar linear to nonlinear transformation with the decreasing in T. Nonlinear *IV* characteristics of several cuprate superconductors have been observed including Bi-2212 superconductors **[42-45]**.

Nonlinear behaviour in *IV* has been observed in both the pure (**S17**) and doped (**S18**-**S21**) superconductors. Moreover, the nonlinear behaviour becomes visible within a range of temperatures which is below the onset T_c but above T_c ($\rho \approx 0$). The nonlinear behaviour is related to the zero field BKT vortex distribution in the 2D and quasi-3D systems. Firstly, we have analysed the nonlinear behaviour of *IV* using eqn **1.1** **[46, 47]**. The BKT transition at $T = T_{BKT}$ is characterized by a change in η **[48]**. Above T_{BKT}, as a result of the unbinding of the vortex-antivortex pairs linear *IV* corresponding to η = 1 is observed. We have fitted *IV* curves by using eqn **1.1** and extracted η as a function of T for all samples. In the inset of **Figure 5.3(A-E)**, we have shown the fitting lines for the corresponding samples. In **Figure 5.4** we have shown the variation of extracted η with T for all samples. (i) Clearly the variation η (T) is found to be nonlinear in nature in **S17** and there is no signature of the saturation even at the lower temperature. (ii) The maximum observed η = 2.0 corresponding to the pure sample (**S17**). Therefore, no clear BKT transition is observed in the pure **S17** down to the lowest possible measured

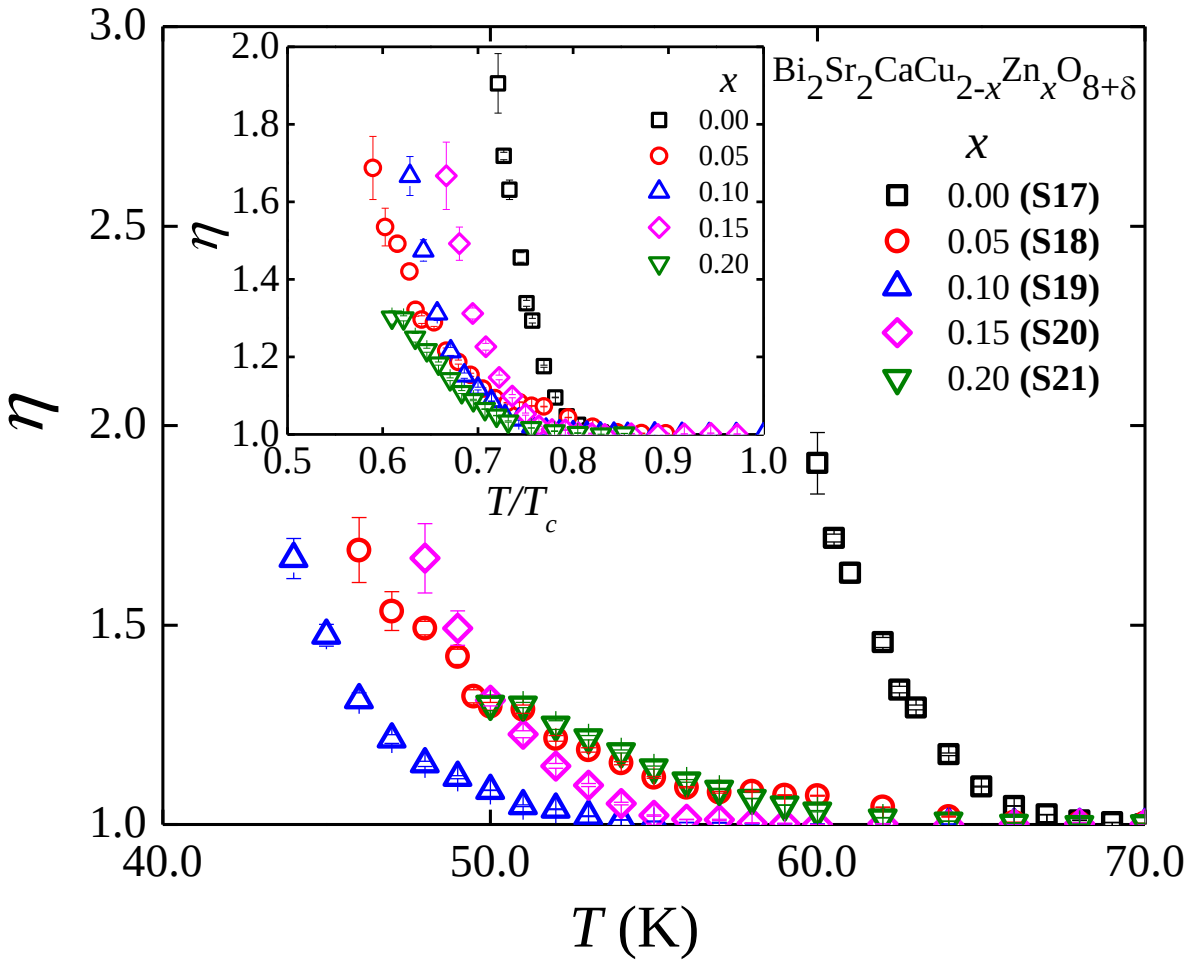

Figure 5.4: Variations of η as a function of T for **S17-S21**. In the inset we have shown η as a function of the reduced temperature T/T_c.

T. In several pure Bi-2212, a clear BKT has been reported earlier **[49, 50]**. The reduced η reveals that the BKT transition is broadened in the pure Bi-2212 (**S17**) **[51]**. (iii) In Zn-doped Bi-2212 (**S18 - S21**), all η (T) remains nonlinear but with an indication of more broadened in nature. With the increase in Zn concentration beyond 0.05, the broadening is reduced with x = 0.1 and 0.15 followed by a further enhanced broadening in η (T) for x = 0.2 **[52, 53]**. In inset of **Figure 5.4**

we have shown the variations of η as a function of the reduced temperature, T/T_c. It reveals how the η (T) in Zn-doped superconductors drastically changes with that corresponding to **S17**. A clear reduction in the observed highest η in each Zn-doped Bi-2212 reveals that the vortex-antivortex paired state in the BKT system below T_{BKT} gets strongly affected even by the nonmagnetic impurity. In a highly layered Bi-2212 superconducting system, how the nonmagnetic can affect such nonlinear η (T) has been resolved by analysing the SPS as a function of T **[54]**.

Following the AHNS model, we have extracted the $J_s(T)$ with the help of the eqn **1.2** **[55-57]**. At $T=T_{BKT}$ the SPS, $J_s(T = T_{BKT})$ is zero. In addition, below T_{BKT}, the topological phase consisting of vortex-antivortex pairs forms. In **Figure 5.5**, we have shown J_s as a function of T. We have shown J_s as a function of the reduced temperature, T/T_c in the inset of **Figure 5.5**. Nonlinear variation of J_s with T has been observed in the pure Bi-2212 superconductors **[58, 59]**. Actually, the distribution of the phase angle of superconducting pairs forms the vortex-antivortex pairs in zero external magnetic field case. Thermal fluctuations induce unbinding of such pairs. Generally, the J_s is almost zero for unbound pairs ($T \geq T_{BKT}$). Phase of the non-condensed (Copper) pairs generally related with the unbinding state of vortices. In the pure Bi-2212 the maximum SPS, J_s^m = 17.3 K has been observed at T = 60.0 K which corresponds to $T/T_c \sim 0.75$. The maximum SPS is an important quantity because below T_c ($\rho \approx 0$), the extraction of the SPS

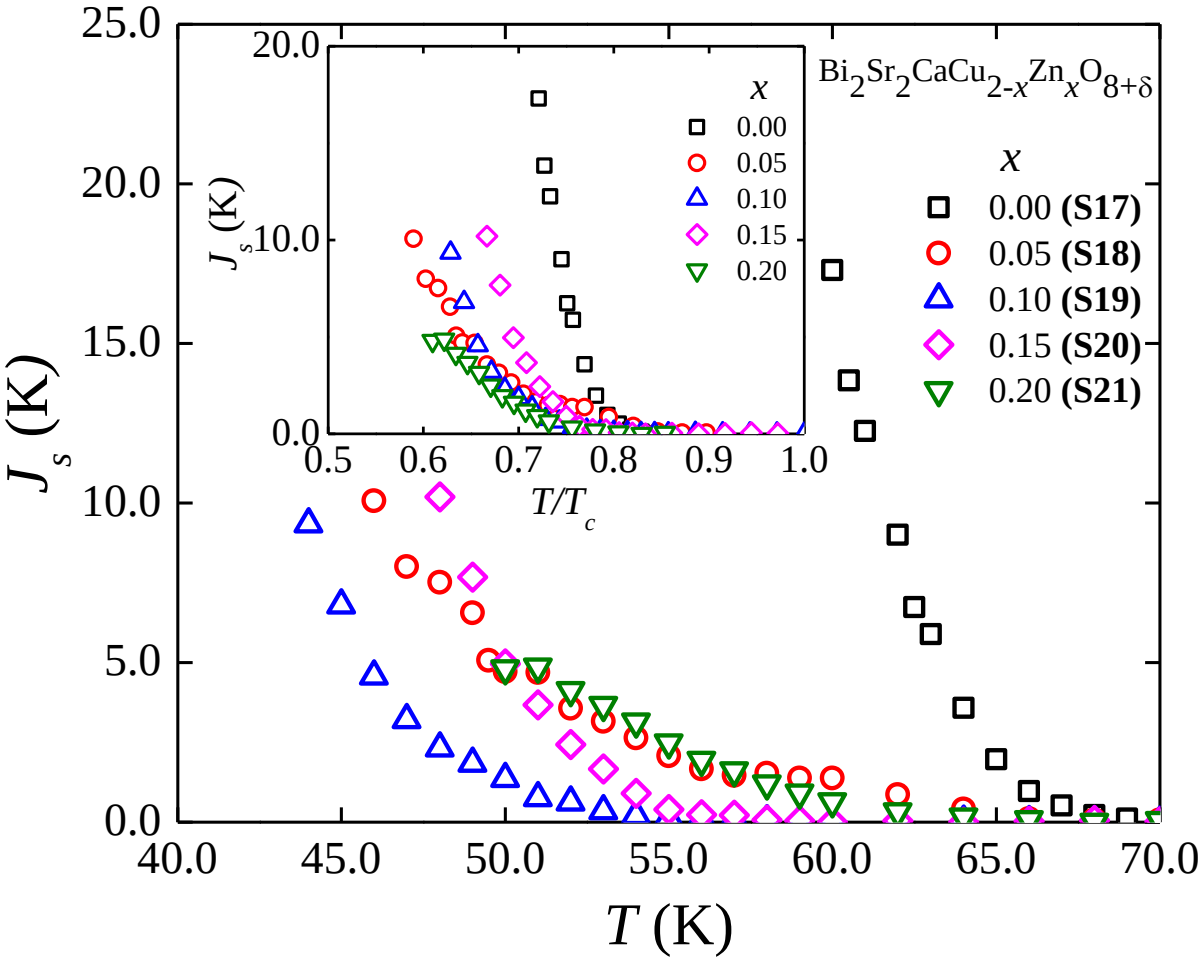

Figure 5.5: Variations of J_s (T) for the pure **S17** to Zn-doped Bi-2212 (**S18-S21**). In the inset corresponding $J_s(T/T_c)$ is also shown.

is not possible in *IV* method. However, it is reasonable to assume that the maximum SPS, J_s ($T \rightarrow T_c$ ($\rho \approx 0$)) is sufficiently close enough to correlate with T_c ($\rho \approx 0$).

The J_s (T) in all **S18-S21** superconducting samples are found to be nonlinear. A strong suppression in J_s (T) has been observed in Zn substituted Bi-2212 (**S18-**

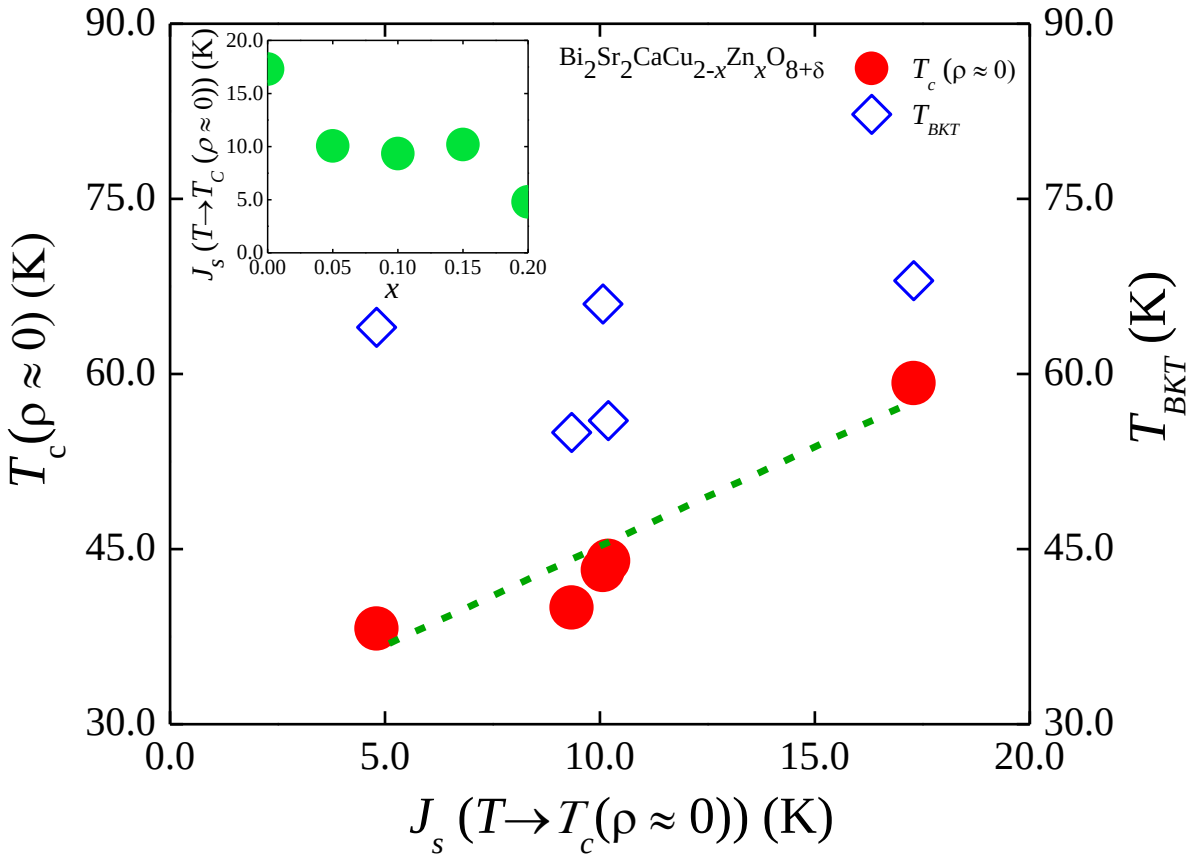

Figure 5.6: Variation of $T_c(\rho \approx 0)$ with $J_s\ (T \rightarrow T_c(\rho \approx 0))$ with a fitting (dotted) line. In the inset the variation of $J_s\ (T \rightarrow T_c(\rho \approx 0))$ as a function of x is shown.

S21). With the increase in the doping of the nonmagnetic Zn the maximum J_s also decreases. In the inset of **Figure 5.6**, we have shown how $J_s^m = J_s\ (T \rightarrow T_c(\rho \approx 0))$ decreases with x. The observed suppression of the SPS is clearly caused by the nonmagnetic impurity in the superconducting planes. It also indicates that the underlying BKT vortex system formed at the zero field has been highly affected. In **Figure 5.6**, we have plotted $T_c(\rho \approx 0)$ as a function of $J_s\ (T \rightarrow T_c(\rho \approx 0))$ of the corresponding sample. Clearly a linear variation has been observed in presence of the suppression by a nonmagnetic impurity in Bi-2212 which is consistent with

the linear Uemura plot **[58, 59]**. We observed that the nonmagnetic Zn in the Cu site causes the suppression in J_s. A scanning tunneling microscopy (STM) showed that the nonmagnetic Zn induces a quasiparticle scattering in the superconducting planes in Bi-2212 **[26, 27]**. A localized scattering center induces an additional scattering to the existing pairing interactions over a length scale of ~15 Å. A strong phase fluctuation results from such additional scattering centers **[60, 61]**. An induced phase fluctuations in the superconducting planes suppress the SPS strongly **[62]**. However, the induced localized phase fluctuations are having inhomogeneous distributions as a result of which the linear scaling relation gets affected weakly. We assume that at the unbinding temperature $T = T_{BKT}$ as shown in **Figure 5.6** the phase coherence completely disappears and it is reasonable because of the known unbinding of BKT vortices at T_{BKT} **[46, 47]**. The ratio of $T_{BKT}/T_c(\rho \approx 0) = 1.2$ for the pure Bi-2212 ($x = 0$) which indicates that the phase fluctuations are important. In Bi-2212 single crystal, the ratio is found to be 1.5 **[62]**. With the increase in Zn concentration, the ratios are 1.5, 1.4, 1.37 and 1.7 for $x = 0.05$, 0.1, 0.15 and 0.2 respectively which reveals that the local scattering centres induced phase fluctuations are reasonably affected.

5.4 Summary

Nonlinear *IV* characteristics have been observed in Zn-doped Bi-2212 below the superconducting transition temperature. An exponent exhibit how the

nonlinearity is affected by nonmagnetic scattering centers. The SPS extracted by using the AHNS theory reveals a strong suppression by nonmagnetic impurities in the superconducting planes of Bi-2212. Phase fluctuations are found to be responsible for the suppression following the ratio of T_{BKT} and $T_c(\rho \approx 0)$. The characteristic critical temperature $T_c(\rho \approx 0)$ follows a linear scaling relation with the SPS.

Nonlinear *IV* characteristics are observed in several HTS as discussed in **Chapter 3** (electron doping in lattice site of YBCO), **Chapter 4** (YCMO inclusions in inter-granular region of YBCO) and the present **Chapter 5** (nonmagnetic doping in lattice sites of Bi-2212). In all studied HTS are having nonlinear nature of *IV* and have comparable tuning of the SPS. However, no uniform relation between T_c and the SPS has been observed for several systems. Both the carrier concentration and the inter-granular inclusions affect SPS strongly. Both the YBCO and Bi-2212 based HTS systems are having nonlinear variations of the SPS with *T*. *IV* studies therefore reveals that the tuning of the SPS is therefore possible by using both types of inclusions from (i) lattice sites and (ii) inter-granular regions. Investigating magnetic properties (magnetization and magnetic critical current density) of several such representative HTS systems with comparable nature of the variations of the SPS (observed from the *IV* studies) will be important to enhance the pinning of vortices. Next two Chapters have been included for that purpose.

5.5 References

[1] I. Božović, X. He, J. Wu, A. T. Bollinger, Nature **536** (2016) 309.

[2] S. Steers, T. R. Lemberger, J. Draskovic, Phys. Rev. B **94** (2016) 094525.

[3] T. R. Lemberger, I. Hetel, A. Tsukada, M. Naito, M. Randeria, Phys. Rev. B **83** (2011) 140507(R).

[4] P. G. Baity, X. Shi, Z. Shi, L. Benfatto, D. Popović, Phys. Rev. B **93** (2016) 024519.

[5] I. Hetel, T. R. Lemberger, M. Randeria, Nat. Phys. **3** (2007) 700.

[6] B. Nachumi, A. Keren, K. Kojima, M. Larkin, G. M. Luke, J. Merrin, O. Tchernyshöv, Y. J. Uemura, N. Ichikawa, M. Goto, S. Uchida, Phys. Rev. Lett. **77** (1996) 5421.

[7] D. Deepwell, D. C. Peets, C. J. S. Truncik, N. C. Murphy, M. P. Kennett, W. A. Huttema, R. Liang, D. A. Bonn, W. N. Hardy, D. M. Broun, Phys. Rev. B **88** (2013) 214509.

[8] I. Maccari, L. Benfatto, C. Castellani, Phys. Rev. B **96** (2017) 060508(R).

[9] T. Sk, A. K. Ghosh, J. Low Temp. Phys. **198** (2020) 224.

[10] O. Simard, C.-D. Hébert, A. Foley, D. Sénéchal, A.-M. S. Tremblay, Phys. Rev. B **100** (2019) 094506.

[11] S. Weyeneth, T. Schneider and E. Giannini Phys. Rev. B **79** (2009) 214504.

[12] T. M. Benseman, J. R. Cooper, C. L. Zentile, L. Lemberger, G. Balakrishnan, Phys. Rev. B **84** (2011) 144503.

[13] W. C. Lee, J. Sinova, A. A. Burkov, Y. Joglekar, A. H. MacDonald, Phys. Rev. B **77** (2008) 214518.

[14] I. Božović, A. T. Bollinger, J. Wu, X. He, Low. Temp. Phys. **44** (2018) 519.

[15] U. Erdenemunkh, B. Koopman, L. Fu, K. Chatterjee, W. D. Wise, G. D. Gu, E. W. Hudson, M. C. Boyer, Phys. Rev. Lett. **117** (2016) 257003.

[16] J. Yong, M. J. Hinton, A. McCray, M. Randeria, M. Naamneh, A. Kanigel, T. R. Lemberger, Phys. Rev. B **85** (2012) 180507(R).

[17] J. E. Sonier, Rep. Prog. Phys. **70** (2007) 1717.

[18] L. Luan, O. M. Auslaender, T. M. Lippman, C. W. Hicks, B. Kalisky, J. H. Chu, J. G. Analytis, I. R. Fisher, J. R. Kirtley, K. A. Moler, Phys. Rev. B **81** (2010) 100501(R).

[19] S. J. Turneaure, A. A. pesetski, T. R. Lemberger, J. Appl. Phys. **83** (1998) 4334.

[20] H. Kim, V. G. Kogan, K. Cho, M. A. Tanatar, R. Prozorov, Phys. Rev. B **87** (2013) 214518.

[21] P. A. Lee, N. Nagaosa, X. G. Wen, Rev. Mod. Phys. **78** (2006) 17.

[22] H. G. Luo, T. Xiang, Phys. Rev. Lett. **94** (2005) 027001.

[23] C. Panagopoulos, B. D. Rainford, J. R. Cooper, W. Lo, J. L. Tallon, J. W. Loram, J. Betouras, Y. S. Wang, C. W. Chu, Phys. Rev. B **60** (1999) 14617.

[24] Z. Sefrioui, D. Arias, C. Leon, and J. Santamaria, E. M. Gonzalez, J. L. Vicent, P. Prieto, Phys. Rev. B **70** (2004) 064502.

[25] D. P. Norton, D. H. Lowndes, Phys. Rev. B **48** (1993) 6460.

[26] S. H. Pan, E. W. Hudson, K. M. Lang, H. Eisaki, S. Uchida, J. C. Davis, Nature **403** (2000) 746.

[27] Y. Fukuzumi, K. Mizuhashi, K. Takenaka, S. Uchida, Phys. Rev. Lett. **76** (1996) 684.

[28] V. Ambegaokar, B. I. Halperin, D. R. Nelson, E. D. Siggia, Phys. Rev. Lett. **40** (1978) 783.

[29] V. Ambegaokar, B. I. Halperin, D. R. Nelson, E. D. Siggia, Phys. Rev. B **21** (1980) 1806.

[30] C. Bernhard, J. L. Tallon, C. Bucci, R. De Renzi, G. Guidi, G. V. M. Williams, C. Niedermayer, Phys. Rev. Lett. **77** (1996) 2304

[31] E. W. Carlson, S. A. Kivelson, V. J. Emery, E. Manousakis, Phys. Rev. Lett. **83** (1999) 612.

[32] G. Seibold, L. Benfatto, C. Castellani, J. Lorenzana, Phys. Rev. Lett. **108** (2012) 207004.

[33] A. K. Ghosh, A. N. Basu, Phys. Rev. B **59** (1999) 11193.

[34] A. K. Ghosh, A. N. Basu, Supercond. Sci. Technol. **11** (1998) 852.

[35] P. Das, A. K. Ghosh, Physica C **548** (2018) 27.

[36] T. Sk, A. K. Ghosh, AIP advances **10** (2020) 065117.

[37] S. Ono, Y. Ando, Phys. Rev. B **67** (2003) 104512.

[38] X. H. Chen, M. Yu, K. Q. Ruan, S. Y. Li, Z. Gui, C.G.Zhang, L. Z. Cao, Phys. Rev. B **58** (1998) 14221.

[39] Y. Lubashevsky, A. Garg, Y. Sassa, M. Shi, A. KanigeL, Phys. Rev. Lett. **106** (2011) 047002.

[40] M. Akoshima, T. Noji, Y. Ono, Y. Koike, Phys. Rev. B **57** (1998) 7491.

[41] Y. Zuev, M. S. Kim, T. R. Lemberger, Phys. Rev. Lett. **95** (2005)137002.

[42] Y. Matsuda, S. Komiyama, T. Onogi, T. Terashima, K. Shimura, Y. Bando Phys. Rev B **48** (1993) 10498.

[43] S. Martin, A. T. Fiory, R. M. Fleming, G. P. Espinosa, A. S. Cooper, Phys. Rev. Lett **62** (1989) 677.

[44] D. H. Kim, A. M. Goldman, J. H. Kang, R. T. Kampwirth, Phys. Rev. B **40** (1989) 8834.

[45] H. H. Wen, P. Ziemann, H. A. Radovan, S. L. Yan, Europhys. Lett. **42** (1998) 319.

[46] V. L. Berezinskiĭ, Zh. Eksp. Teor. Fiz. **61** (1971) 1144.

[47] J. M. Kosterlitz, D. J. Thouless, J. Phys. C **6** (1973) 1181.

[48] B. I. Halperin, D. R. Nelson, J. Low Temp. Phys. **36** (1979) 599.

[49] S. N. Artemenko, I. G. Gorlova, Y. I. Latyshev, Phys. Lett. A **138** (1989) 428.

[50] L. Miu, D. Miu, G. Jakob, H. Adrian, Phys. Rev. B **73** (2006) 224526.

[51] L. Benfatto, C. Castellani, T. Giamarchi, Phys. Rev. B **80** (2009) 214506.

[52] D. M. Broun, W. A. Huttema, P. J. Turner, S. Özcan, B. Morgan, R. Liang, W. N. Hardy, D. A. Bonn, Phys. Rev. Lett. **99** (2007) 237003.

[53] N. R. Lee-Hone, J. S. Dodge, D. M. Broun, Phys. Rev. B **96** (2017) 024501.

[54] M. Franz, C. Kallin, A. J. Berlinsky, M. I. Salkola, Phys. Rev. B **56** (1997) 7882.

[55] P. Minnhagen, Rev. Mod. Phys. **59** (1987) 1001.

[56] A. Andersson, J. Lidmar, Phys. Rev. B **87** (2013) 224506.

[57] D. R. Nelson, J. M. Kosterlitz, Phys. Rev. Lett. **39** (1977) 1201.

[58] Y. J. Uemura, G. M. Luke, B. J. Sternlieb, J. H. Brewer, J. F. Carolan, W. N. Hardy, R. Kadono, J. R. Kempton, R. F. Kiefl, S. R. Kreitzman, P. Mulhern, T. M. Riseman, D. Ll. Williams, B. X. Yang, S. Uchida, H. Takagi, J. Gopalakrishnan, A. W. Sleight, M. A. Subramanian, C. L. Chien, M. Z. Cieplak, G. Xiao, V. Y. Lee, B. W. Statt, C. E. Stronach, W. J. Kossler, X. H. Yu, Phys. Rev. Lett. **62** (1989) 2317.

[59] Y. J. Uemura, A. Keren, L. P. Le, G. M. Luke, W. D. Wu, Y. Kubo, T. Manako, Y. Shimakawa, M. Subramanian, J. L. Cobb, J. T. Markert, Nature **364** (1993) 605.

[60] A. V. Balatsky, M. I. Salkola, A. Rosengren, Phys. Rev. B **51** (1995) 15547.

[61] H. Tsuchiura, Y. Tanaka, M. Ogata, S. Kashiwaya, J. Phys. Soc. Jpn. **68** (1999) 2510.

[62] V. J. Emery, S. A. Kivelson, Nature **374** (1995) 434.

Chapter 6

Drastic enhancement of magnetic critical current density in Zn-doped Bi-2212

6.1 Introduction

In cuprate HTS studies on the correlation between the vortex pinning and critical current density, J_{cm} have been carried out in several ways in the last few decades **[1-10]**. The critical current density of the HTS systems can be measured by using both the transport and magnetic methods **[11, 12]**. Studying magnetic J_{cm} as a function of (i) temperature (T) and (ii) magnetic field (H) is important to understand the underlying pinning mechanisms. The nature and strengths of pinning can be tuned in HTS in a number of ways **[13-15]**. An important aspect of research in the area is to understand how the number density and nature of the pinning centers can be changed which will be very effective in enhancing J_{cm}. Doping in planes in which superconductivity originates is an efficient method to alter the pinning force density and hence the critical current density **[16, 17]**.

Controlling of motion of vortex and critical current density are intensively studied by several experimental techniques in both low anisotropic and high anisotropic superconductors **[18, 19]**. It is known that localised magnetic moments of a magnetic domain are highly effective in vortex confinement which in turn reduces vortex dissipations and alters critical current density. Nonmagnetic impurity suppresses superconductivity in the Zn-doped Bi-2212. The suppression of T_c is caused by the local suppression of the superconductivity by the strong scattering **[20, 21]**. It will be very important to understand how nonmagnetic dopants affect the pinning of pancake vortices in Bi-2212 superconductors.

We have studied magnetization (M) as a function of H at several T in two bulk superconductors. Using the $M(H)$ curves we have extracted irreversible magnetization, ΔM and corresponding $J_{cm}(H, T)$. A phase diagram, H-T has been found to understand the nature of vortex pinning in different regions (combinations of H and T). The irreversibility line (IL) has also been determined. Change in the J_{cm} in nonmagnetic Zn-doped Bi-2212 has been studied. In addition, associated pinning force densities of both samples have been extracted.

6.2 Experimental

We have synthesized a series of bulk $Bi_2Sr_2 CaCu_{2-x} Zn_xO_{8+\delta}$ (Bi-2212) (x = 0 through 0.2) superconducting samples by using the standard solid state reaction

method **[22-25].** Two Bi-2212 samples with x is 0 (**S17**) and 0.15 (**S20**) have been included for the magnetization studies of the present Chapter. The typical dimensions of the bar-shaped sample used for the magnetization measurement are 4.0 × 3.0 × 1.0 mm^3. Measurements of $M(H)$ by using a VSM have been discussed in **Chapter 2**. At H = 100.0 Oe, $M(T)$ has been measured in the field cooled (FC) mode to determine critical temperature.

6.3 Results and discussions

In **Figure 6.1(A)** we have plotted M as a function of H for the pure Bi-2212 superconductor at several temperatures in the range of 2.0 K through 60.0 K. We have observed that at 2.0 K, $M \equiv M_+(H)$ above $H \sim 0.15$ T correspond to the vortex states which is extended up to the maximum H of 7.0 T **[26]**. As T is increased to 50.0 K, the vortex state is observed for $H \geq 0.02$ T. During decreasing H from 7.0 T to 0, measured $M \equiv M_-(H)$ is also shown in **Figure 6.1(A)**. The width of the magnetization curve, $\Delta M = M_-(H) - M_+(H)$ varies strongly with H and it is shown in **Figure 6.1(B)**. In the inset of $\Delta M(H)$, we have shown the bar-shaped Bi-2212 sample used for the measurement. The applied field (H) is perpendicular to the shown surface of the sample. However, since we have used bulk sample superconducting grains are randomly oriented with respect to the applied magnetic field for both $M_-(H)$ and $M_+(H)$. Therefore, $\Delta M(H)$ as shown in **Figure 6.1(B)** is contributed by the vortex states of Bi-2212 superconductor **[27]**.

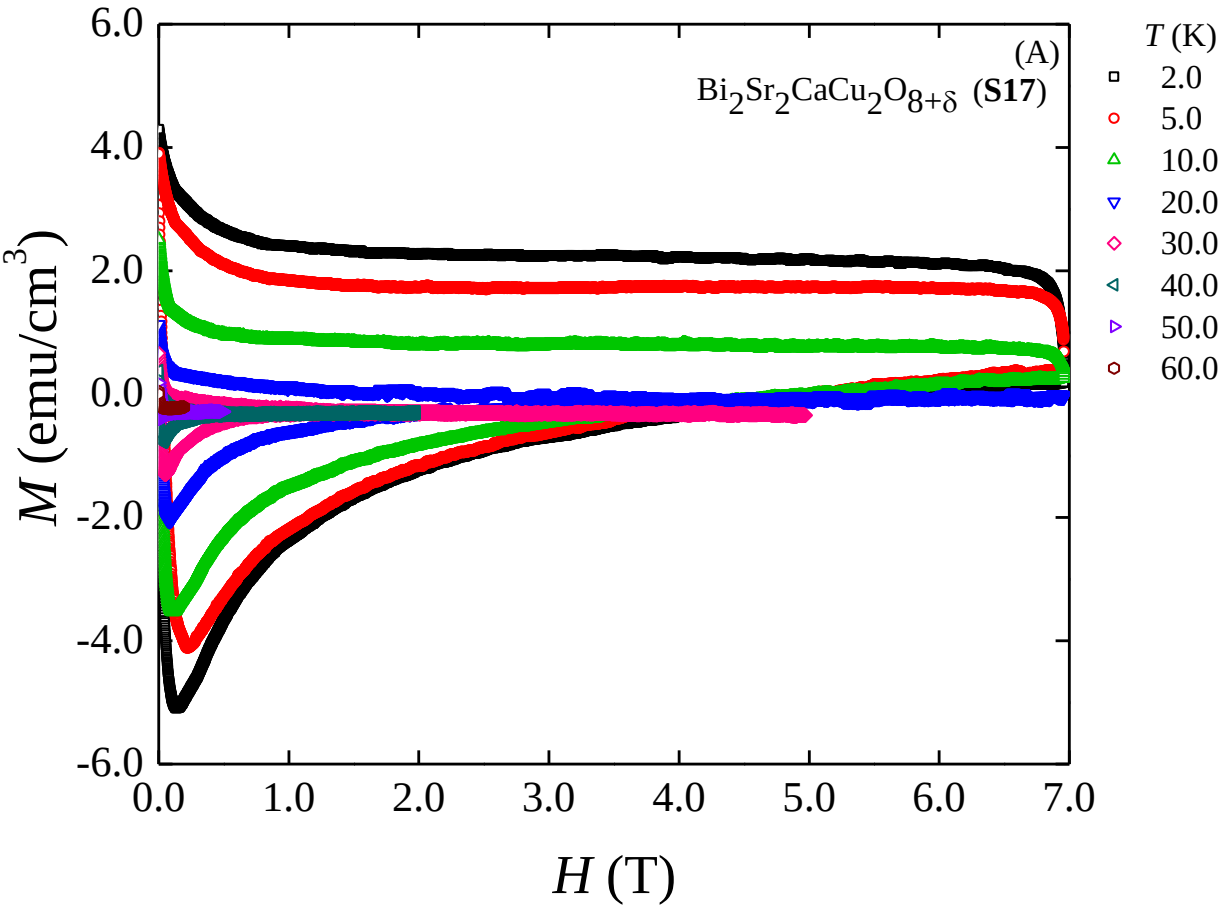

Figure 6.1(A): $M(H)$ at several temperatures below T_c in $Bi_2Sr_2CaCu_2O_{8+\delta}$ (**S17**).

We have shown $M(H)$ of Zn-doped Bi-2212 at T = 2.0, and 45.0 K in **Figure 6.2(A**). At 2.0 K, the $M_+(H)$ curve exhibits a dip at H = 0.12 T and therefore the vortex state exists in the range of 0.12 T $\leq H \leq$ 7.0 T at 2.0 K. $M(H)$ curve at the highest T = 45.0 K exhibits that the vortex state exists in the range of 0.019 T $\leq H \leq$ 7.0 T. In **Figure 6.2(B)** we have plotted $\Delta M(H)$ at several T of Zn-doped Bi-2212. Clearly, we have observed that at the lowest temperature of 2.0 K, ΔM varies strongly with H indicating that collective vortex pinning is dominating the lower field regime at ~ 2.0 K **[28]**. As we increase the field to 7.0 T the variation

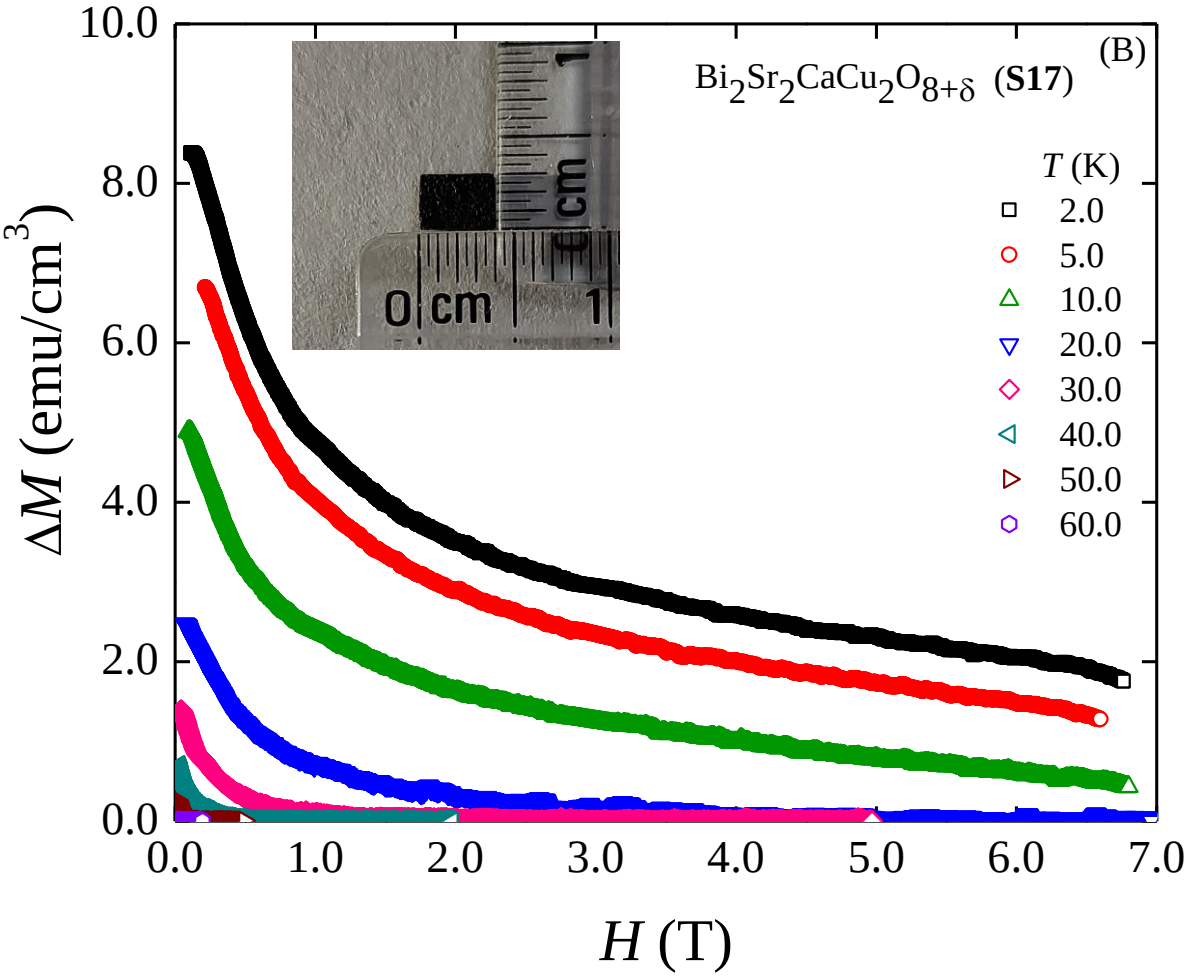

Figure 6.1(B): $\Delta M(H)$ of the pure Bi-2212 (**S17**) superconductor at several temperatures. In the inset the measured bar-shaped samples is shown.

$\Delta M(H)$ exhibits a tendency of almost saturation which is consistent with a single vortex regime. However, the rate of change of ΔM with H is highly enhanced in the Zn-doped superconductors at the range of the lower field particularly indicating that the collective pinning is highly affected at the lower (H, T) regime of the phase diagram.

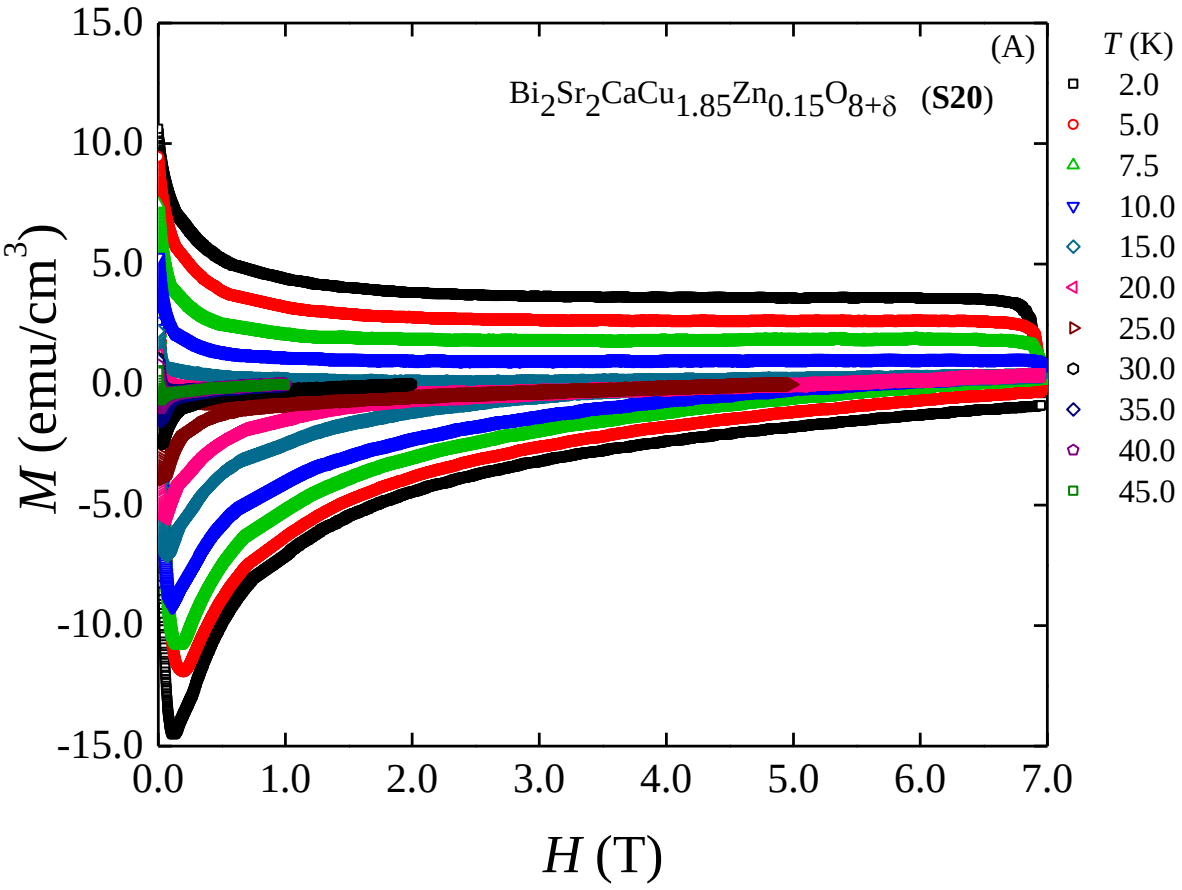

Figure 6.2(A): $M(H)$ at several temperatures below T_c in $Bi_2Sr_2CaCu_{1.85}Zn_{0.15}O_{8+\delta}$ (**S20**).

We have used the criterion ΔM = constant to form the *H-T* phase diagram to understand change in the nature of pinning in both samples **[28]**. In **Figure 6.3(A,B)**, we have shown two *H-T* diagrams corresponding to the pure and Zn-doped Bi-2212 superconductors. In the pure Bi-2212, the curvature of all *H-T* curves as observed in **Figure 6.3(A)** are found to be upward as well as similar **[29]**. It indicates that the nature of pinning is collective vortex pinning corresponding to the lower part (both *T* and *H* low) *H-T* diagram with a possible crossover to single vortex pinning at upper part with higher *H* and *T* **[30]**.

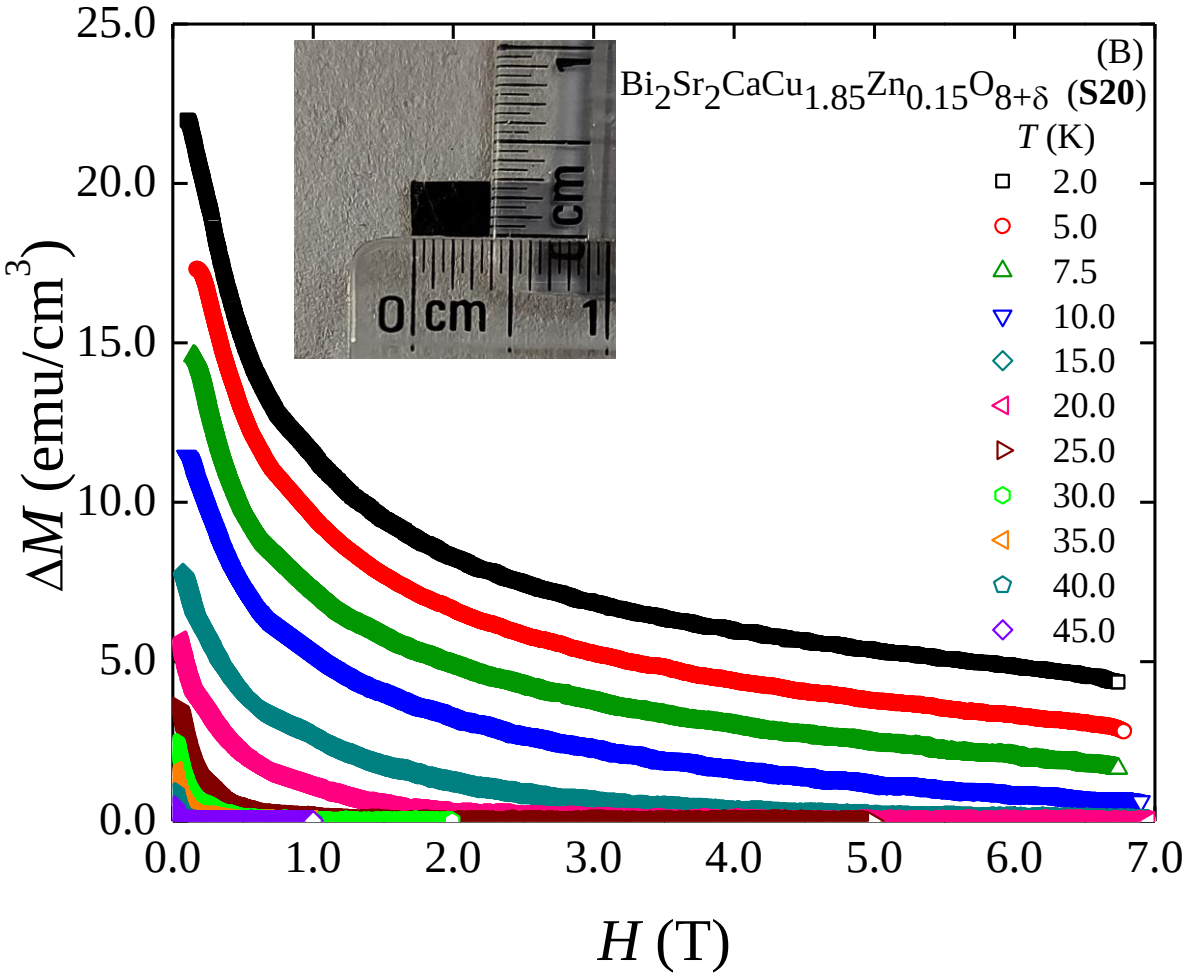

Figure 6.2(B): $\Delta M(H)$ of the Zn-doped Bi-2212 (**S20**) superconductor at several temperatures. In the inset the measured bar-shaped samples is shown.

Therefore, in presence of the lower thermal fluctuations and relatively lower field having relatively higher inter vortex spacing, $a_0 = (\phi_0/H)^{1/2}$, the collective pancake vortex description is observed to be dominating in the highly anisotropic pure Bi-2212. With the increase in thermal fluctuations (for example 60.0 K) and higher field (~ 6-7 T), there is a possibility to single vortex pinning regime. As shown in **Figure 6.3(B)**, the *H*-T diagrams corresponding to the Zn-doped Bi-2212 sample

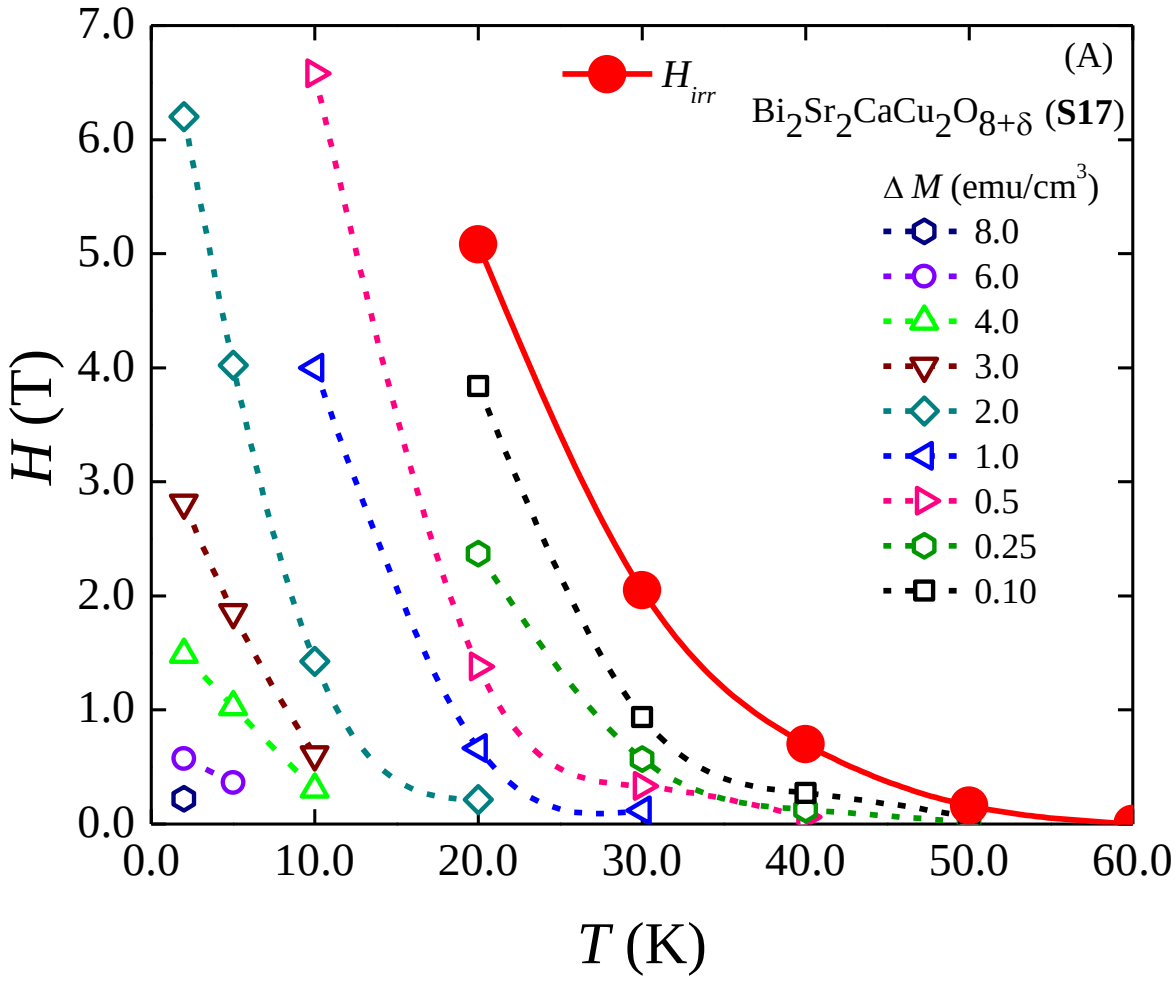

Figure 6.3(A): Variation of *H-T* determined by using a criterion of ΔM = constant for Bi-2212 (**S17**). Irreversibility lines (IL) is shown in the panel as well.

exhibit that the curvatures remain upward in the entire range of the phase diagram. However, each *H-T* curve indicates that both the collective vortex pinning as well as the possibility of the crossover are strongly affected as a result of the Zn substitution in Cu sites **[31]**.

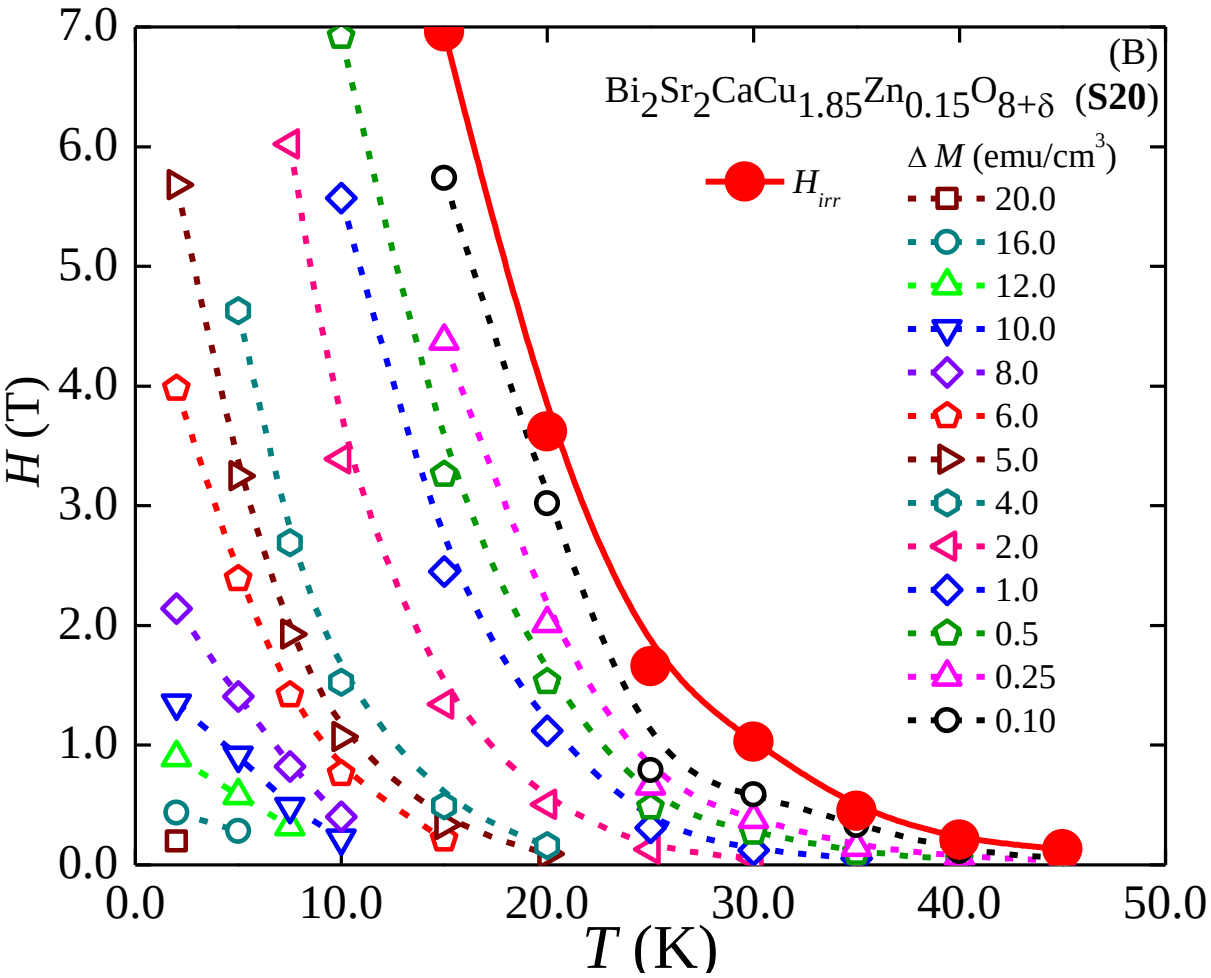

Figure 6.3(B): Variation of *H*-*T* determined by using a criterion of ΔM = constant for **S20**. Irreversibility lines (IL) is shown in the panel as well.

Using the magnetic field corresponding to the converging point of M_+ and M_- we have determined the irreversibility field, H_{irr}, at each T for both samples. In the *H*-*T* diagrams, we have shown irreversibility lines (IL) as H_{irr}-T curves. Upward curvature of IL is observed in the pure Bi-2212 earlier as well by other experiments **[29, 32]**. Clearly the IL is shifted strongly by the nonmagnetic Zn dopants. A comparison of H_{irr}-T of both samples has also been shown in the inset of **Figure 6.6**. Therefore, expanding the irreversible region in $M(H)$ curve corresponding to the observed IL in Bi-2212 superconductor may not be possible by Zn which is observed in other studies **[33]**.

Figure 6.4(A): SEM of the pure Bi-2212 (**S17**) superconductor.

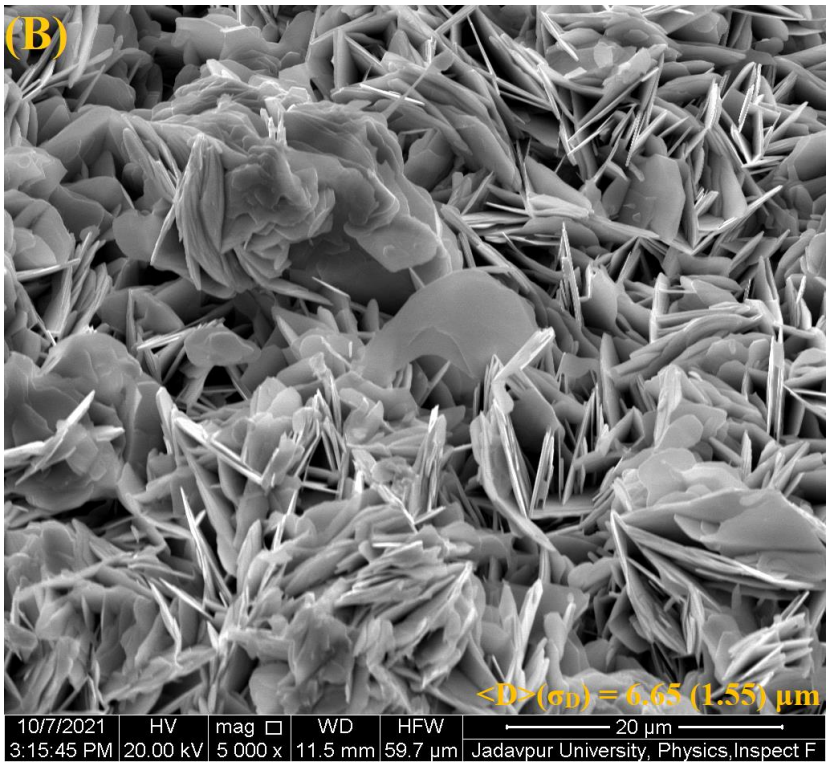

Figure 6.4(B): SEM of Zn-doped Bi-2212 (**S20**) superconductor.

In **Figure 6.4(A)** and **Figure 6.4(B)**, we have shown SEM of two samples. Clearly the distribution of the size of the grains and shapes remains almost unaffected in Zn-substituted Bi-2212 with respect to that of the pure Bi-2212 sample. Typical average individual grain dimensions are found to be ~ 6.65μm and 6.85 μm corresponding to the pure and doped Bi-2212 respectively. Therefore, it may be reasonable to attribute any change in the $M(H)$ and associated curve solely to the doping in the Cu sites.

In the inset of **Figure 6.5**, we have shown two $M(T)$ curves measured around the phase transition region in the field cooling (FC) mode at 100.0 Oe. It reveals that the critical temperatures are 81.0 K and 71.0 K corresponding to the pure and Zn-doped Bi-2212 respectively. Therefore, the suppression of T_c is strong enough even as a doping of nonmagnetic Zn which is consistent with other studies **[33]**. We have calculated the J_{cm} as a function of H by using the $\Delta M(H)$ **[34, 35]** with help of the equation

$$J_{cm} \propto \Delta M(H) \qquad (\mathbf{6.1})$$

Following the sample dimensions as shown in the inset of **Figure 6.1(B)** and **Figure 6.2(B)** the proportionality constants are found for (i) the pure Bi-2212 and (ii) Zn-doped Bi-2212 respectively. In **Figure 6.5**, we have shown J_{cm} as a function of H for several T in the range of 2.0 K - 60.0 K. For the pure Bi-2212, at 2.0 K the highest $J_{cm} \sim 1.5\times10^4$ A/cm^2 is found at $H \sim 0.11$ T. In **Figure 6.6**,

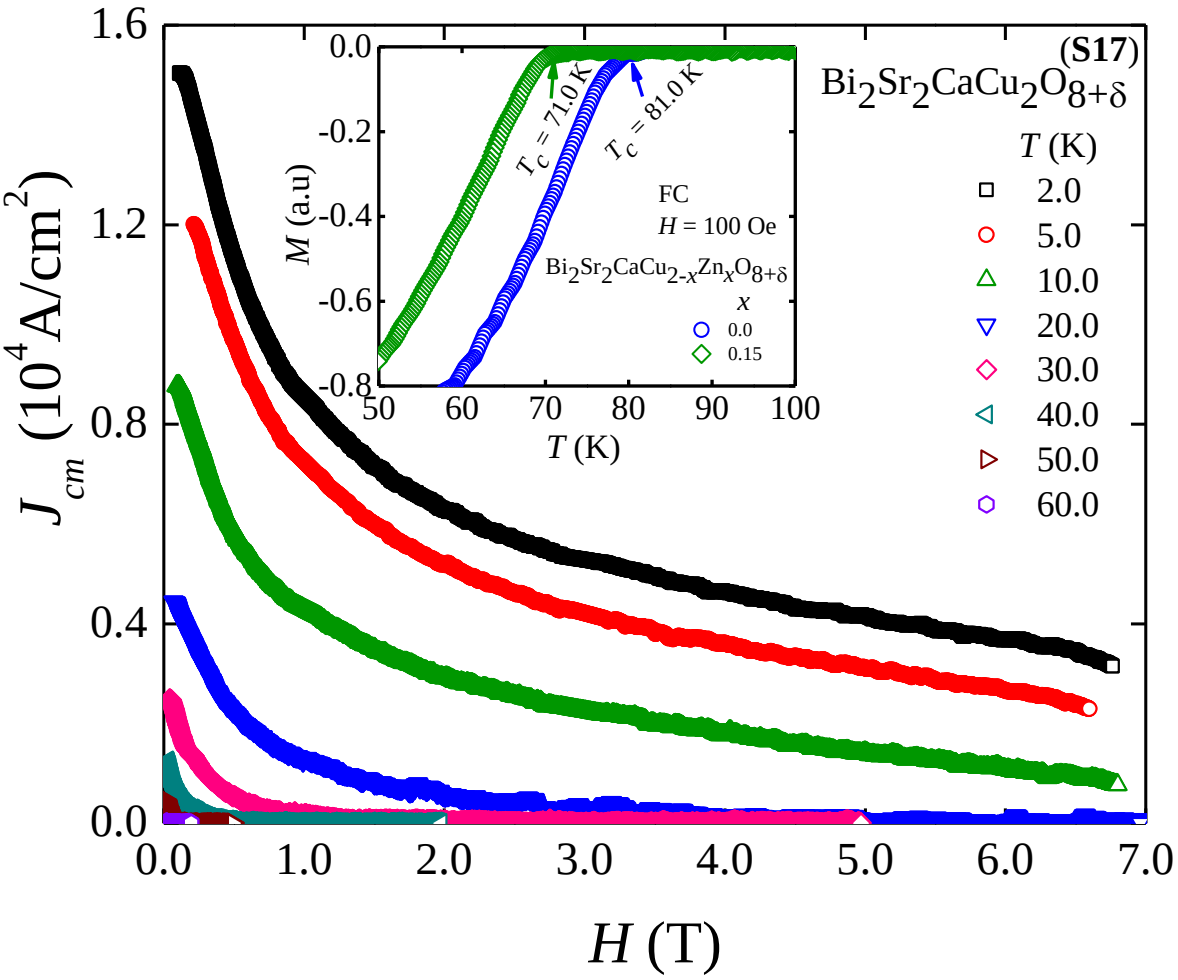

Figure 6.5: Variations of $J_{cm}(H)$ for the pure Bi-2212 (**S17**) at several T.

we have plotted $J_{cm}(H)$ of Zn-doped Bi-2212 at several T in the range of 2.0 K – 45.0 K. The highest J_{cm} is found to be ~ 4.0×10^4 A/cm^2 at 2.0 K and H = 0.10 T. Clearly at 2.0 K, the maximum J_{cm} is enhanced by a factor of ~ 2.6. Enhancement of critical current density is reported in several doped Bi-2212 including heavily Pb doped Bi-2212 **[36]**. Magnetic critical current density obtained from the $M(H)$ measurement in Bi-2212 wire at 4.2 K and 5.0 T is reported to be ~ 45.0 $\times 10^4$ A/cm^2 which is clearly much higher than observed J_{cm} (5.0K, 5T) ~ 0.40 $\times 10^4$ A/cm^2 in a bulk sample **[37]**. Clearly granular networks in the bulk Bi-2212

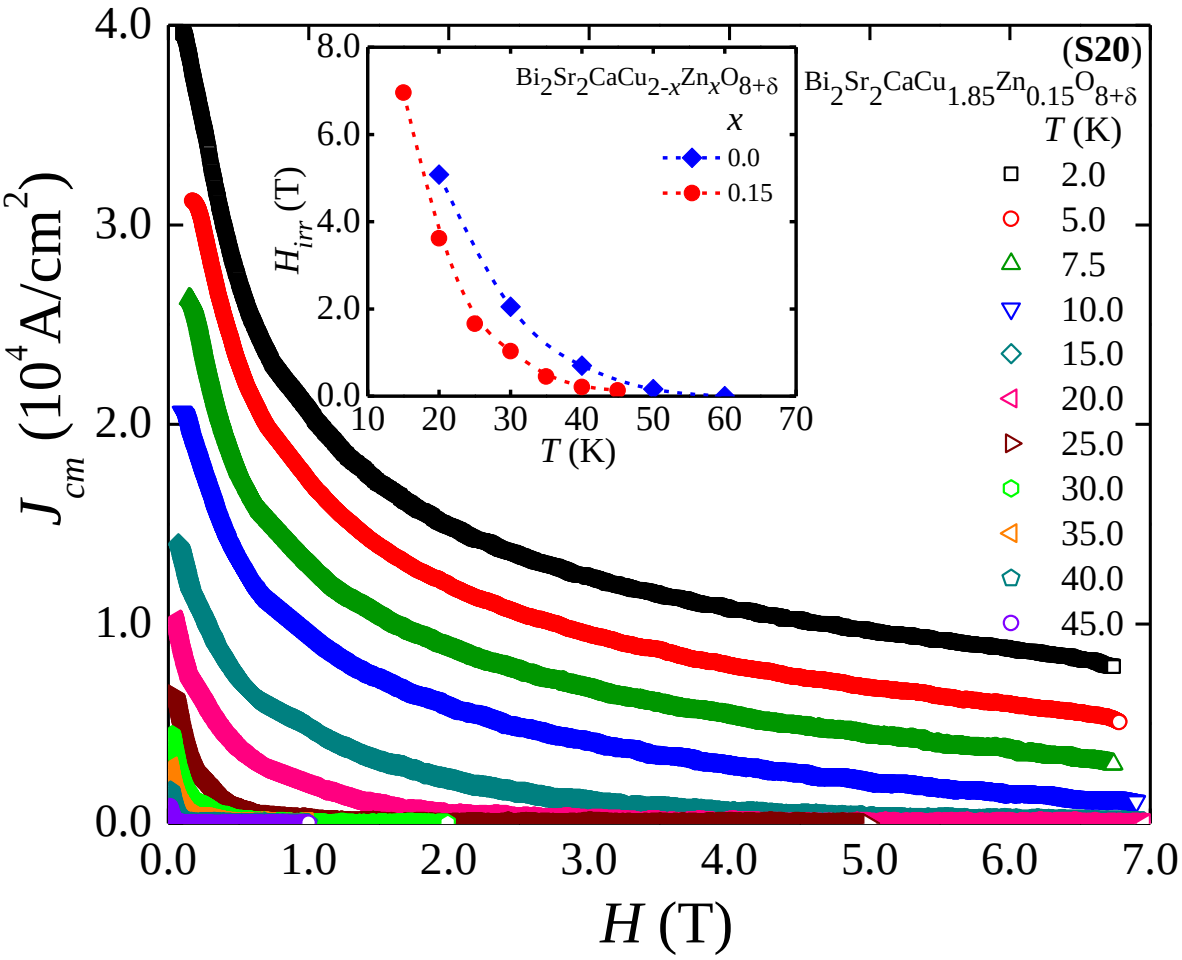

Figure 6.6: Variations of $J_{cm}(H)$ at several T in the Zn-doped Bi-2212 (**S20**).

sample decrease critical current density strongly. In the Zn-doped Bi-2212 superconductor, the increase in J_{cm} in order of magnitude reveals that the strengths of both collective pinning and single vortex pinning increases. Now question remains how the pinning strength is increased by nonmagnetic doping in Cu site. Several studies are there how nonmagnetic dopants affect in the superconducting planes of Bi-2212 **[38]**. One of the major findings is that a localised magnetic moment is generated by a nonmagnetic dopant. Therefore, it is reasonable to correlate that there may be a dominating role of the localised moment in enhanced critical current density in Zn-doped Bi-2212.

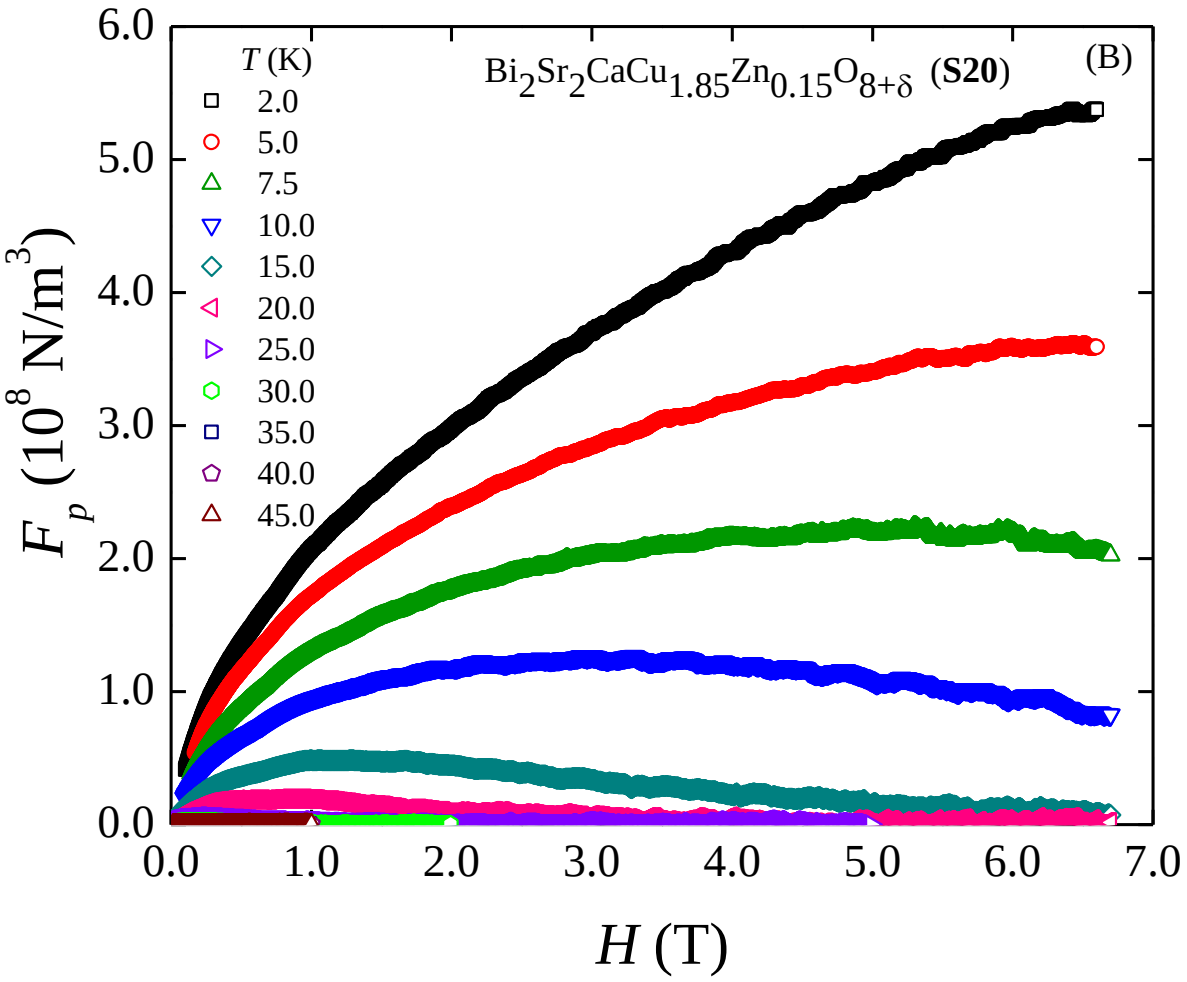

Figure 6.7(A): F_p as a function of H at several T in Bi-2212 (**S17**).

The pinning force density, F_p has also been extracted **[39]** using an equation

$$F_p = J_{cm} \times H \qquad \textbf{(6.2)}$$

In **Figure 6.7(A)** and **Figure 6.7(B)**, we have shown pinning force density as a function of the applied magnetic field (up to 7.0 T) at several T for the pure and doped Bi-2212 respectively. The pinning force densities corresponding to the highest J_{cm} which are observed at 2.0 K are found to be ~ 1.7×10^7 and 4.1×10^7 N/m^3 corresponding to undoped and doped Bi-2212 respectively. Since the single

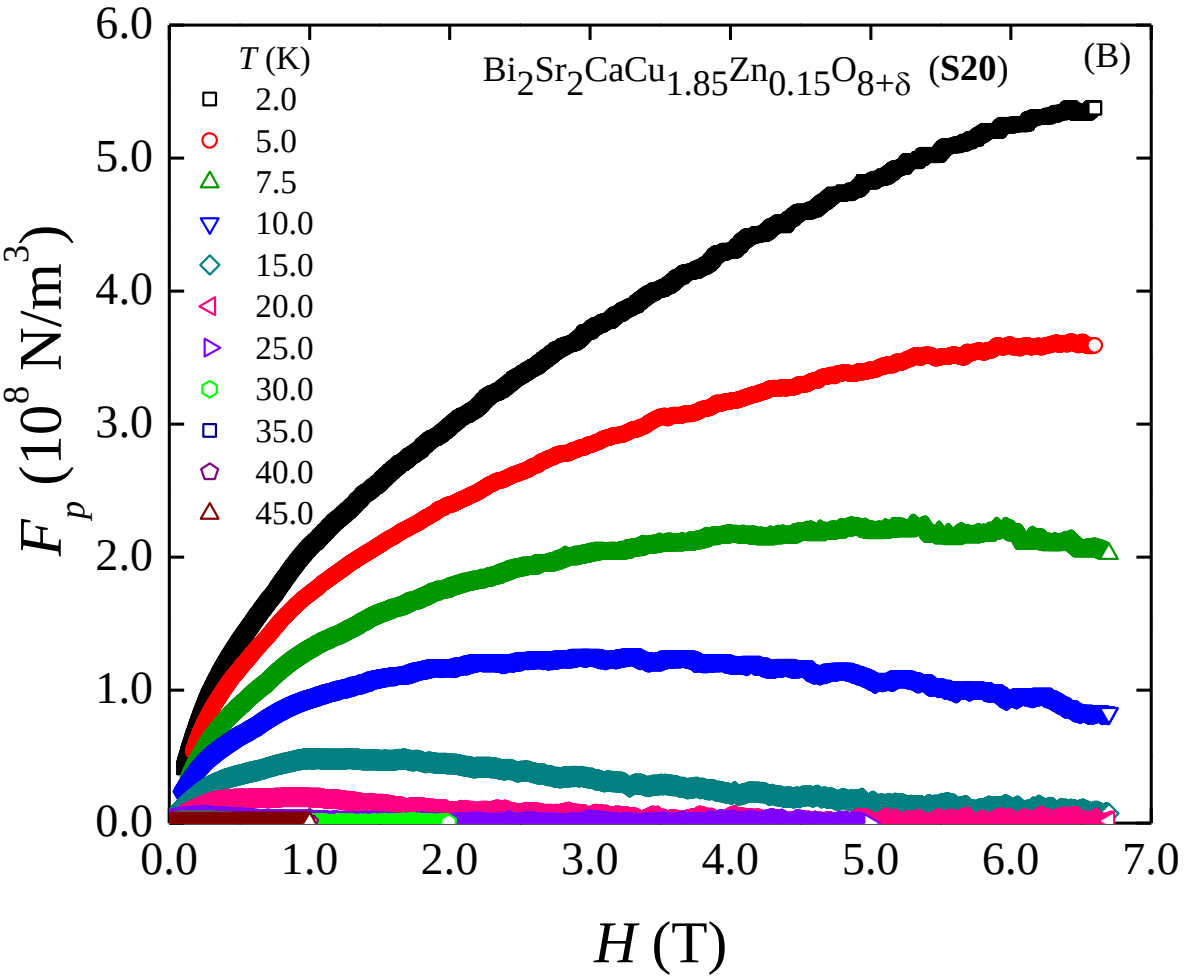

Figure 6.7(B): F_p as a function of H at several T in Zn-doped Bi-2212 (**S20**) superconductors.

vortex pinning is the mechanism in both samples with different pinning force density and J_{cm} it would be important to understand the change. Several nonmagnetic doping elements including Zn in CuO_2 planes in cuprate superconductors generate localized magnetic moment ~ 1.9 μ_B theoretically through the hybridization **[40].** The localised magnetic moment in Bi-2212 affects the vortex pinning strongly which is responsible for the enhancement of J_{cm} **[18, 41]**.

6.4 Summary

Nonmagnetic Zn-doped in Bi-2212 superconductor causes an enormous enhancement in $\Delta M(H)$. Magnetization loops below T_c are used to understand the *H-T* phase diagrams of the pure and Zn-doped Bi-2212. $M(H)$ curves are used to determine *H-T* diagram including the irreversibility line (H_{irr}-T). $J_{cm}(H)$ extracted from the $M(H)$ loops is found to be very sensitive to the doping of the nonmagnetic element in the superconducting planes of Bi-2212. The observed maximum critical current increases by an order of magnitude of 2.6 in Zn-doped Bi-2212. Even though the collective pinning regime is mostly observed there is a possibility of a single vortex pinning regime as we approach to higher filed regime. Also, the strength of pinning is highly changed by the localized magnetic moment in Bi-2212 in the collective pinning regime and results an increase in the $J_{cm}(H)$.

6.5 References

[1] A. E. Koshelev, V. M. Vinokur, Phys. Rev. B **73** (1994) 3580.

[2] G. Blatter, M. V. Feigel'man, V. B. Geshkenbein, A. I. Larkin, and V. M. Vinokur, Rev. Mod. Phys. **66** (1994) 1125.

[3] W. K. Kwok, U. Welp, A. Glatz, A. E. Koshelev, K. J. Kihlstrom, G. W Crabtree, Rep. Prog. Phys. **79** (2016) 116501.

[4] A. K. Ghosh, Y. Hiraoka, M. Tokunaga, T. Tamegai, Phys. Rev. B **68** (2003) 134503.

[5] A. Piriou, Y. Fasano, E. Giannini, Ø. Fischer, Phys. Rev. B **77** (2008) 184508.

[6] P Sunwong, J S Higgins, Y Tsui, M J Raine, D P Hampshire, Supercond. Sci. Technol. **26** (2013) 095006.

[7] N. Ayai, S. Kobayashi, M. Kikuchi, T. Ishida, J. Fujikami, K. Yamazaki, S. Yamade, K. Tatamidani, K. Hayashi, K. Sato, H. Kitaguchi, H. Kumakura, K. Osamura, J. Shimoyama, H. Kamijyo, Y. Fukumoto, Physica C **468** (2008) 1747.

[8] A. Leveratto, V. Zunino, I. Pallecchi, V. Braccini, C. Ferdeghini, A. Malagoli, IEEE Trans. Appl. Supercond. **27** (2017) 6400303.

[9] K. Itaka, H. Taoka, S. Ooi, T. Shibauchi, T. Tamegai, Phys. Rev. B **60** (1999) R9951.

[10] A. K. Ghosh, A. N. Basu, Physica C 3**61** (2001) 135.

[11] G. Wang, M. J Raine, D. P Hampshire, Supercond. Sci. Technol. **31** (2018) 024001.

[12] B. Kalisky, D. Giller, A. Shaulov, T. Tamegai, Y. Yeshurun, Phys. Rev. B **72** (2005) 014531.

[13] F. C. Klaassen, G. Doornbos, J. M. Huijbregtse, R. C. F. van der Geest, B. Dam, and R. Griessen, Phys. Rev. B **64** (2001) 184523; K. Matsumoto and P. Mele, Supercond. Sci. Technol. **23** (2010) 014001.

[14] W. Gerhäusr, G. Ries, H. W. Neumüller, W. Schmidt, O. Eibl, Saemann-Ischenko, S. Klaumünzer, Phys. Rev. Lett. **68** (1992) 879.

[15] N. Cheggour, D. P. Hampshire, Rev. Sci. Instrum. **71** (2000) 4521.

[16] M. Daeumling, J. M. Seuntjens, D. C. Larbalestier, Nature **346** (1990) 332.

[17] C. Reichhardt, C. J. Olson, Groth, S. Field, and F. Nori, Phys. Rev. B **52** (1995) 10441.

[18] M. Z. Cieplak, Z. Adamus, M. Konczykowski, L.Y. Zhu, X. M. Cheng, C. L. Chien Phys. Rev. B **87** (2013) 014519.

[19] M. Lange, M. J. Van Bael, V. V. Moshchalkov, Y. Bruynseraede, Appl. Phys. Lett. **81** (2002) 322.

[20] S. H. Pan, E. W. Hudson, K. M. Lang, H. Eisaki, S. Uchida, J. C. Davis Nature **403** (2000) 746.

[21] Y. Fukuzumi, K. Mizuhashi, K. Takenaka, S. Uchida, Phys. Rev. Lett. **76** (1996) 684.

[22] T. Sk, D. Rakshit, A. K. Ghosh, Phys. Scr. **97** (2022) 025704.

[23] S. Haldar, A. K. Ghosh, Solid State Commun. **347** (2022) 114716.

[24] P. Mandal, D. Rakshit, T. Sk, A. K. Ghsoh, J. Supercond. Nov. Magn. **35** (2022) 1079.

[25] D. Rakshit, T. Sk, P. Das, S. haldar, A. K. Ghosh, Physica C **588** (2021) 1353909.

[26] Y. Yeshurun, A. P. Malozemoff, A. Shaulov, Rev. Mod. Phys. **68** (1996) 911.

[27] E. H. Brandt, Rep. Prog. Phys. **58** (1995) 1465.

[28] L. Krusin-Elbaum, L. Civale, V. M. Vinokur, F. Holtzberg, Phys. Rev. Lett. **69** (1992) 2280.

[29] Y. Ando, G. S. Boebinger, A. Passner, L. F. Schneemeyer, T. Kimura, M. Okuya, S. Watauchi, J. Shimoyama, K. Kishio, K. Tamasaku, N. Ichikawa, S. Uchida, Phys. Rev. B **60** (1999) 12475.

[30] M. F. Goffman, J. A. Herbsommer, F. de la Cruz, T. W. Li, P. H. Kes, Phys. Rev. B **57** (1998) 3663.

[31] L. Civale, L. Krusin-Elbaum, J. R. Thompson, F. Holtzberg, Phys. Rev. B **50** (1994) 7188.

[32] X. R. Zhaoa, K. Kitazawaa, T. Hasegawa, Physica C **370** (2002) 44.

[33] A. Maeda, T. Yabe, S. Takebayashi, M. Hase, K. Uchinokura, Phys. Rev. B **41** (1990) 4112.

[34] C. P. Bean, Rev. Mod. Phys. **36** (1964) 31.

[35] S. Salem-Sugui, Jr., P. V. Lopes, M. P. Kern, S. Sundar, Z. Liu, S. Li, H. Luo, L. Ghivelder, Phys. Rev. B **102** (2020) 064509.

[36] I. Chong, Z. Hiroi, M. Izumi, J. Shimoyama Y. Nakayama, K. Kishio, T. Terashima, Y. Bando, M. Takano, Science **276** (1997), 770.

[37] A. Leveratto, A. Angrisani Armenio, A.Traverso, G. De Marzi, G. Celentano, A. Malagoli, Sci. Report **11** (2021) 11660.

[38] E. W. Hudson, K. M. Lang, V. Madhavan, S. H. Pan, H. Eisaki, S. Uchida, and J. C. Davis, Nature **411** (2001) 920; T. Machida, T. Kato, H. Nakamura, M. Fujimoto, T. Mochiku, S. Ooi, A. D. Thakur, H. Sakata, K. Hirata Phys. Rev. B **82** (2010) 180507(R).

[39] M. R. Koblischka and J. Sosnowski, Eur. Phys. J. B **44** (2005) 277.

[40] G. Xiao, M. Z. Cieplak, J. Q. Xiao, C. L. Chien, Phys. Rev. B **42** (1990) 8752.

[41] P. Mandal, D. Rakshit, I. Mukherjee, T. Sk, A. K. Ghosh, Phys. Lett. A **436** (2022) 128072.

Chapter 7

Effectiveness of two pinning profiles in controlling magnetic critical current density in YBCO + YCMO composites

7.1 Introduction

Enhancing pinning strength in YBCO superconductor is very important for the application purposes **[1, 2]**. There are several methods by which pinning strength of line vortices can be tuned. Changing the distribution of intrinsic point pinning centres and pinning landscapes **[3, 4]** and generation of columnar disorder by ion irradiation **[5-7]** are two efficient avenues in which this area of vortex pinning has improved critical current density by order of magnitude. Additions of several particles having different size and properties in several HTS including YBCO have become another popular method in which understanding of enhancing pinning strength needs more intensive research **[8, 9]**. In a bulk YBCO system, the pinning scenario is very complex because the extension of the line vortices covers pinning centres residing both in lattice sites and in the inter-granular region **[10]**. Therefore, the term representing the interaction between the pinning

centres and line vortices of YBCO have two contributions – (i) interaction between point pinning centres and part of line vortex and (ii) interaction between pinning centres in the form of inter-granular particles and remaining part of the line vortex. Even though experimentally it is challenging to understand the impact of multiple types of pinning arising in a well separated region of space in bulk YBCO, mixing of different pinning centres has been attempted to understand vortex pinning mechanism and its several consequences **[11, 12]**.

Magnetic nanoparticles are known to be efficient pinning centres in type-II bulk superconductors. The interaction between the Abrikosov vortices (AV) with magnetic nanoparticles and magnetic dots are used to improve the irreversible magnetization in several hybrid superconducting systems **[13, 14]**. However, in all such magnetic inclusions, more than one pinning landscape is active in vortex pinning. An enhancement of magnetic critical current density needs optimization of pinning by intrinsic pinning landscape and externally included magnetic particles in superconductors. However, intensive research to understand the pinning vortices by mixed landscapes is necessary.

We have generated two different co-existing pinning profiles in bulk YBCO superconductors by (i) varying δ and hence oxygen point disorder and (ii) distribution of added magnetic Y_2CoMnO_6 (YCMO) particles in the inter-granular region of YBCO. Samples with a constant density of magnetic pinning

centres have three different $\delta = 0, 0.1$ and 0.3. It means for a constant inter-granular magnetic pinning profile we have used three intra-granular pinning profiles. We have studied magnetization as a function of temperature (T) and magnetic field (H) at several temperatures below the critical temperature. Irreversible magnetization (ΔM) and J_{cm} have been extracted. Enormous change in J_{cm} in presence of two different pinning profiles has been studied. Impact of coexisting pinning profiles on the J_{cm} is discussed with the help of several pinning parameters.

7.2 Experimental

We have synthesized a series of bulk $YBa_2Cu_3O_{7-\delta}$ superconducting samples by using the standard solid state reaction method **[15-18]**. The details of the synthesis route and sample description are described in **Chapter 2** and **Chapter 4**. One pure sample **S11** ($\delta = 0.3$) and three mixed samples **S13** ($\delta = 0$), **S14** ($\delta = 0.1$), **S15** ($\delta = 0.3$) have been included in the present Chapter. A VSM has been used for measurements of M as a function of the applied magnetic field at constant T. The details of magnetic measurement have been discussed in experimental **Chapter 2**. $M(T)$ has been measured at 50 Oe in the usual zero field cooled (ZFC) mode.

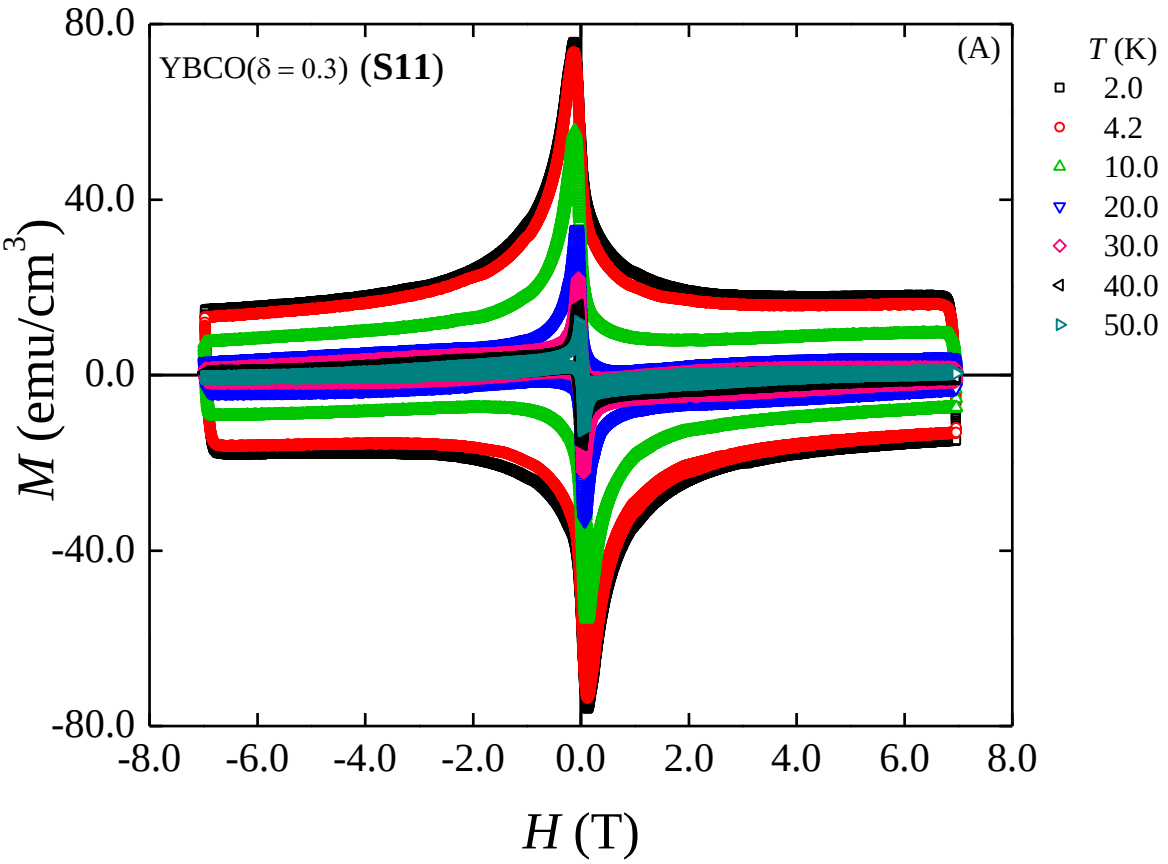

Figure 7.1(A): $M(H)$ at several temperatures below T_c in pure $YBa_2Cu_3O_{7-\delta}$ (YBCO, $\delta = 0.3$) (**S11**).

7.3 Results and discussions

In **Figure 7.1(A)** magnetization as a function of the applied magnetic field are shown for the pure $YBa_2Cu_3O_{7-\delta}$ ($\delta = 0.3$) (**S11**) superconductor at several temperatures in the range of 2.0 K through 50.0 K. At 2.0 K, $M \equiv M_+(H)$ in the range of 0.183 T < H < 7.0 T is the magnetization of the vortex states obtained during the increasing H from 0 to 7.0 T. $M \equiv M_-(H)$ obtained during the decreasing of H from +7.0 T to 0 T is also shown in **Figure 7.1(A)**. At T = 2.0 K, the

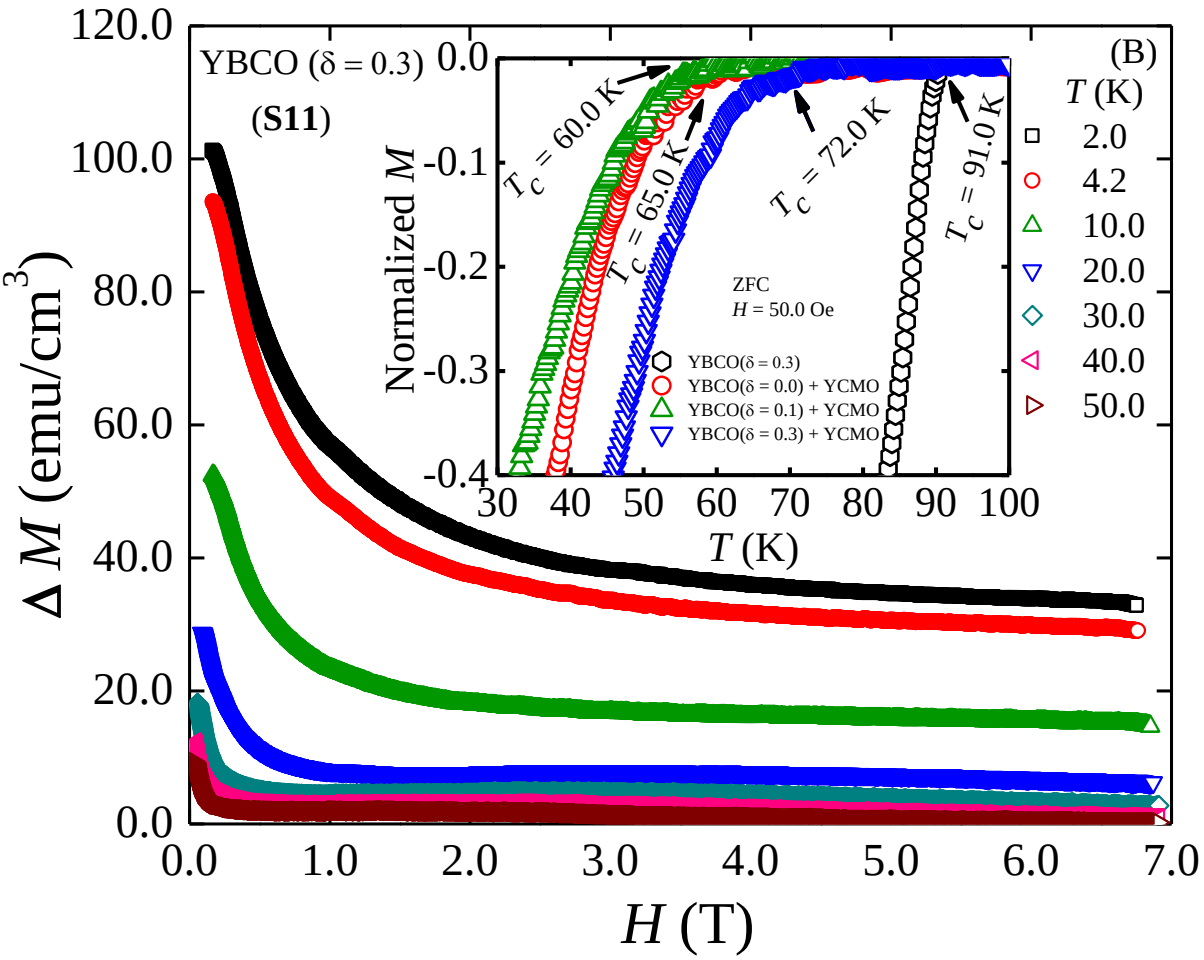

Figure 7.1(B) $\Delta M(H)$ of the pure YBCO ($\delta = 0.3$) (**S11**) superconductor at several temperatures. In the inset, normalised M as a function of T is shown for all samples in which transition temperatures are shown by arrows.

maximum and minimum M are found to be 36.8 emu/cm^3 at $H \sim 0.16$ T and 17.7 emu/cm^3 at $H \sim 6.75$ T respectively. As T is increased to 50.0 K, the vortex state is observed for $H \geq 0.036$ T. The width of the magnetization curve, $\Delta M = M_{-}(H) - M_{+}(H)$ varies strongly with H and it is shown in **Figure 7.1(B)**. Within the measured range of field, the maximum $\Delta M \sim 101.33$ emu/cm^3 is observed at 2.0 K and 0.16 T. The irreversible magnetization in YBCO ($\delta = 0.3$) without any

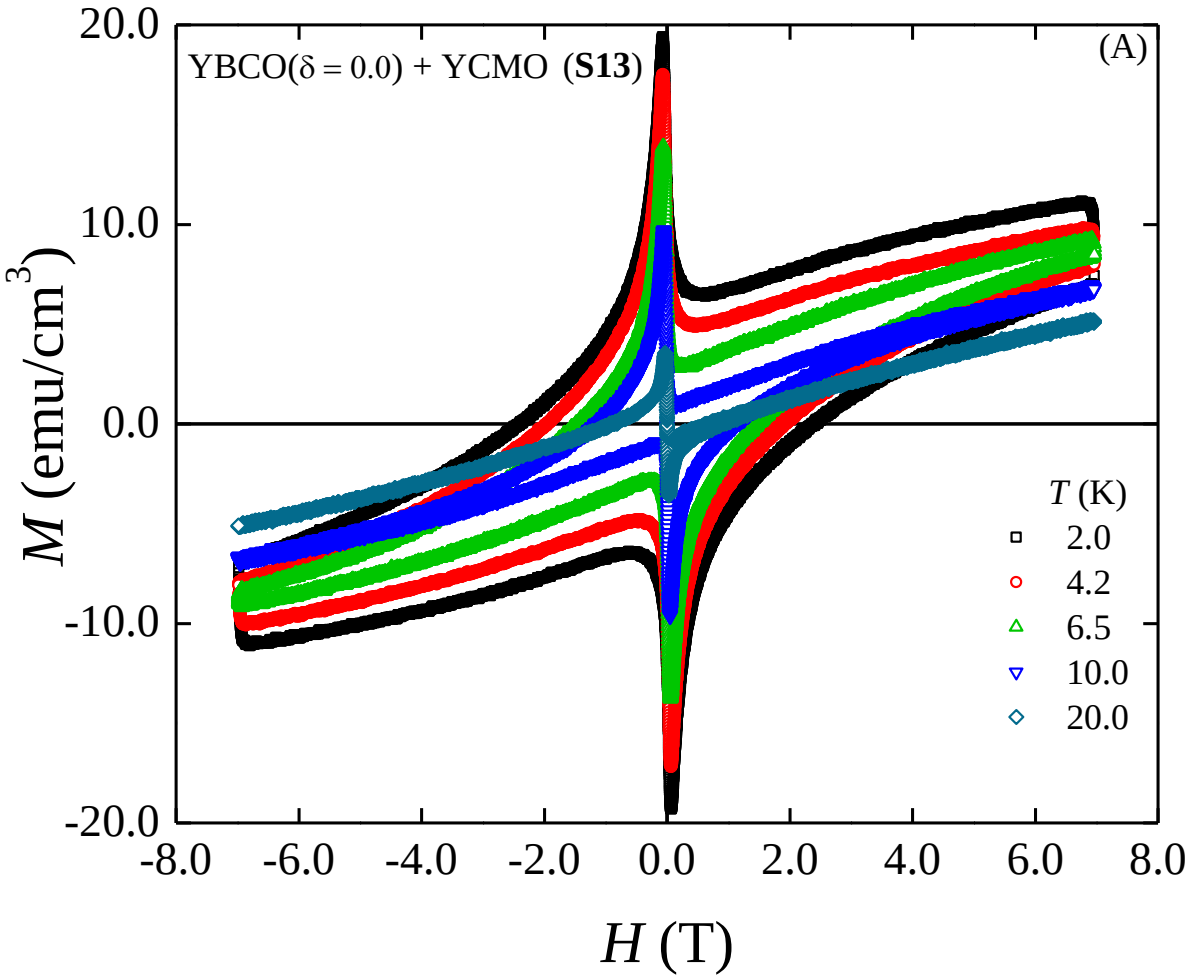

Figure 7.2(A): $M(H)$ at several temperatures below T_c in composite sample YBCO ($\delta = 0$) + 5%YCMO (**S13**).

YCMO is mostly the result of interaction between intrinsic point pinning centres originating from oxygen vacancies in the lattice sites and vortex lines. In addition, the variation of $\Delta M(H)$ is a measure of how solely oxygen vacancy related point pinning profile affects the irreversible magnetization with H in **S11**.

In the inset of **Figure 7.1(B)**, we have shown $M(T)$ curves near the critical temperatures. We observed onset T_c = 91.0 K, 65.0 K, 60.0 K and 72.0 K

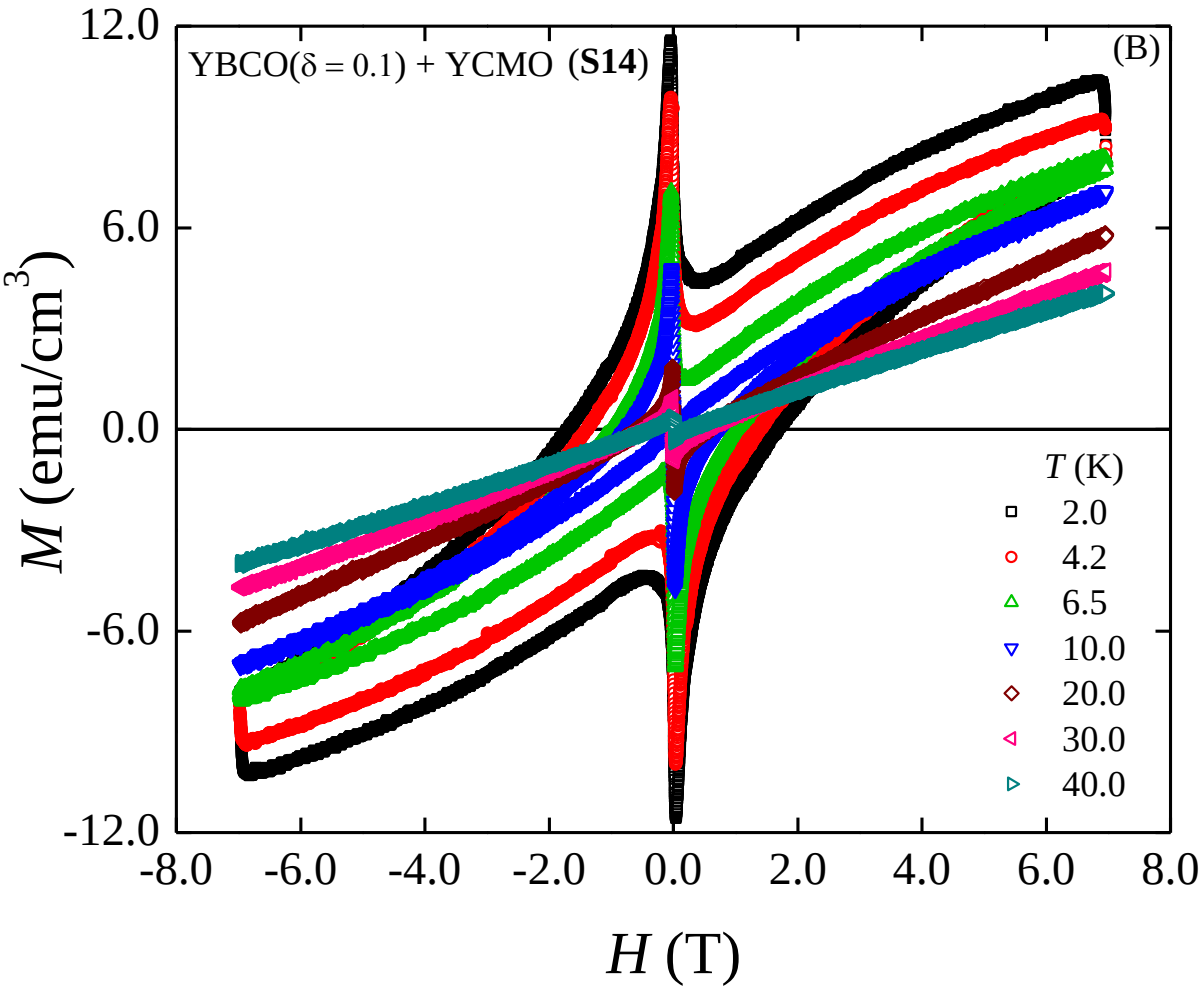

Figure 7.2(B): $M(H)$ at several temperatures below T_c in composite sample YBCO ($\delta = 0.1$) + 5% YCMO (**S14**).

corresponding to **S11**, **S13**, **S14** and **S15** samples respectively **[19]**. Below T_c we have studied $M(H)$ of all samples to understand the effects of two different pinning landscapes on irreversible magnetization, irreversible field and J_{cm}. We have shown $M(H)$ in composite systems consisting of YBCO with 5% YCMO (**S13**, **S14** and **S15**) in **Figure 7.2 (A-C)**. Following $M_+(H)$ curves at 2.0 K it is observed that vortex states exist (i) 0.09 T $\leq H \leq$ 7.0 T in **S13**, (ii) 0.06 T $\leq H \leq$ 7.0 T in **S14** and (iii) 0.07 T $\leq H \leq$ 7.0 T in **S15**. There is a dip in all $M_+(H)$

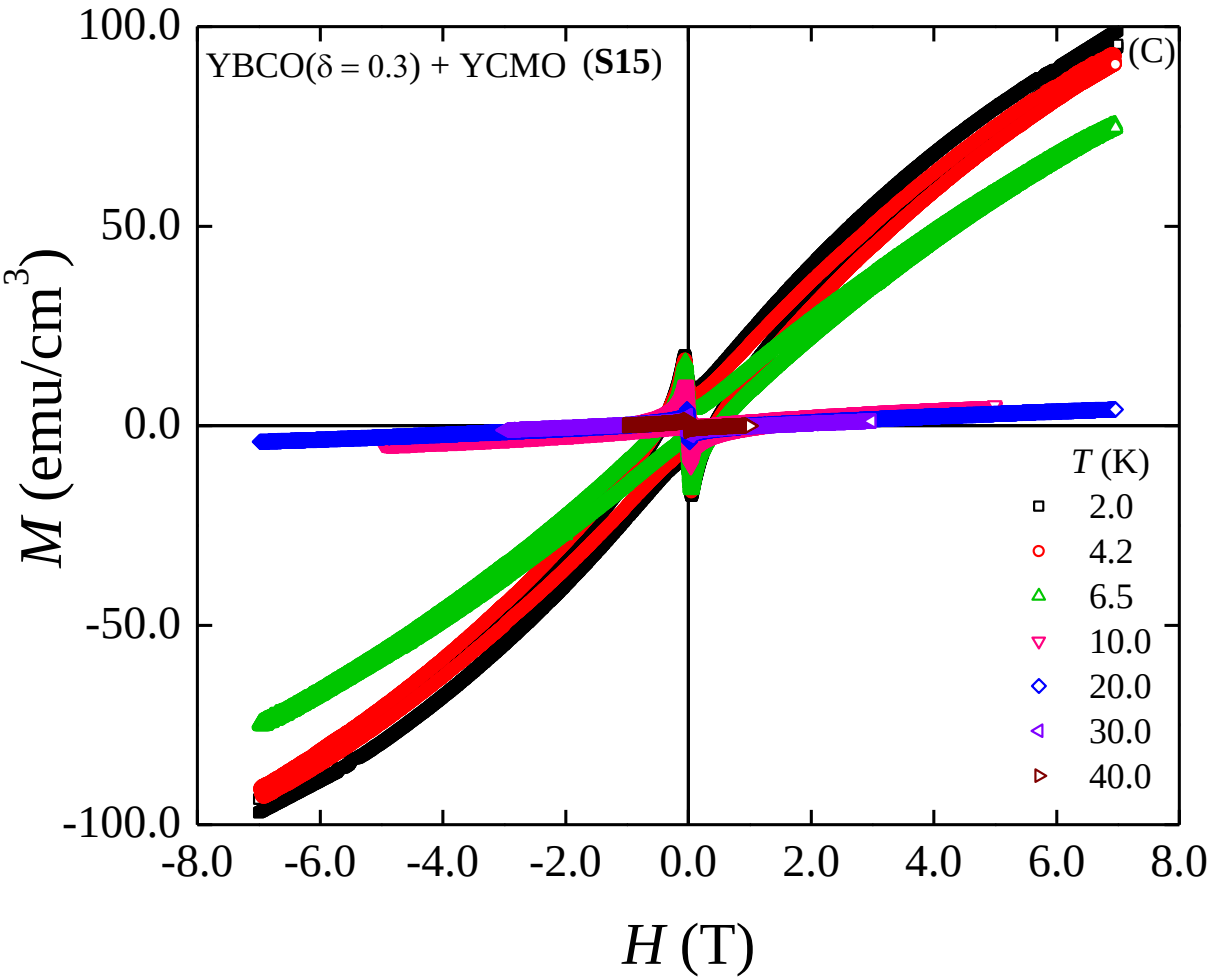

Figure 7.2(C): *M*(*H*)at several temperatures below T_c in composite sample YBCO (δ = 0.3) + 5% YCMO (**S15**).

curves which is shifted with the increase in *T*. We have observed from $M_-(H)$ curve at 2.0 K that M ~ 8.64 emu/cm^3, 5.64 emu/cm^3 and 8.99 emu/cm^3 corresponding to **S13**, **S14** and **S15** respectively at fields corresponding to the observed dip (close to the respective lower critical fields) in $M_+(H)$. Therefore, distributed YCMO related pinning centres reduces the maximum *M* of the mixed state of the YBCO. The pinning profile formed from the distribution of the YCMO is therefore an effective in controlling vortex state magnetic properties.

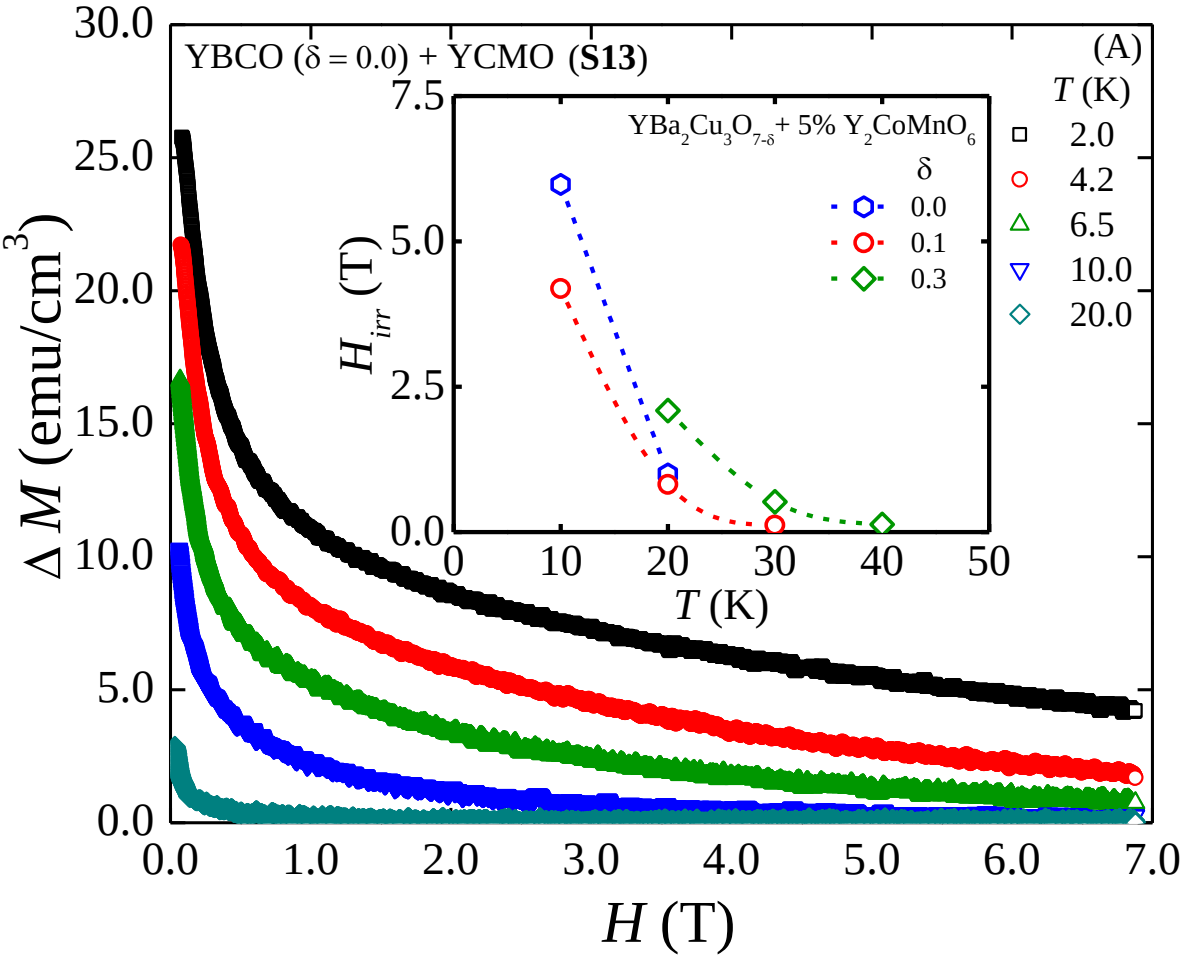

Figure 7.3(A): $\Delta M(H)$ of composite sample YBCO ($\delta = 0.0$) + 5% YCMO (**S13**).

For sample **S15**, neglecting a small mismatch in H an effective maximum magnetic moment contributed by YCMO pinning landscape is ~ (8.99 - 36.8) emu/cm^3 = - 27.8 emu/cm^3. A small variation ~ 3.0 emu/cm^3 in M is originated from the increase in oxygen vacancy (induced via δ) related pinning profile.

Moreover, with the increase in H, magnetic YCMO particles will tend to exhibit the saturation moments. At a higher field limit, $M = M_s$(2.0 K, 6.75 T) are found

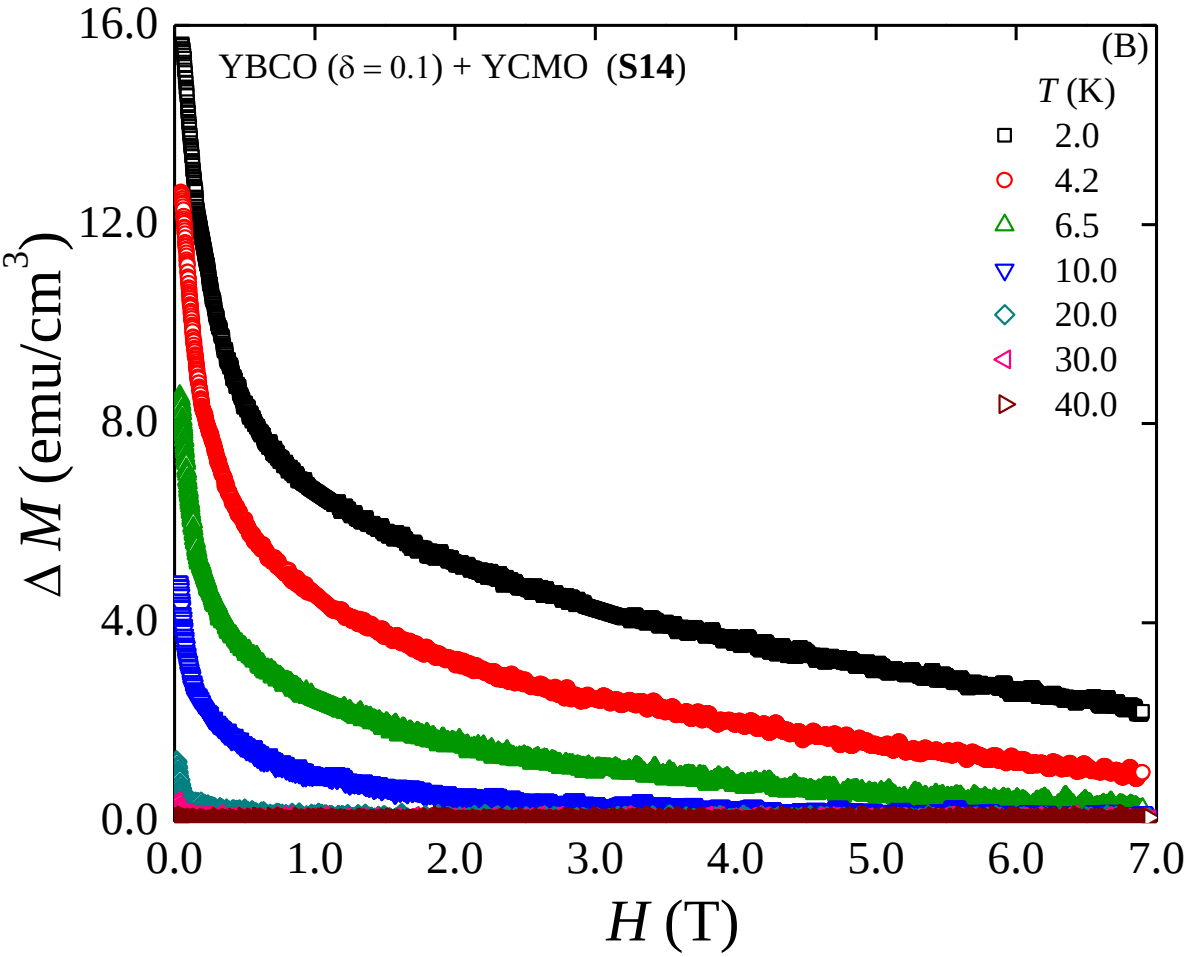

Figure 7.3(B): $\Delta M(H)$ of composite sample YBCO ($\delta = 0.1$) + 5% YCMO (**S14**).

to be ~ 17.71 emu/cm^3 and 96.75 emu/cm^3 corresponding to **S11** and **S15** respectively. Hence at low temperature (2.0 K) and high field (6.75 T) limit magnetic particles related pinning profile contributes an additional moment of ~ (96.79 – 17.71) emu/cm^3 = 79.08 emu/cm^3. It reveals that at low T and higher field limits magnetic pinning profile becomes more dominating than the other pinning landscape of the oxygen disorders.

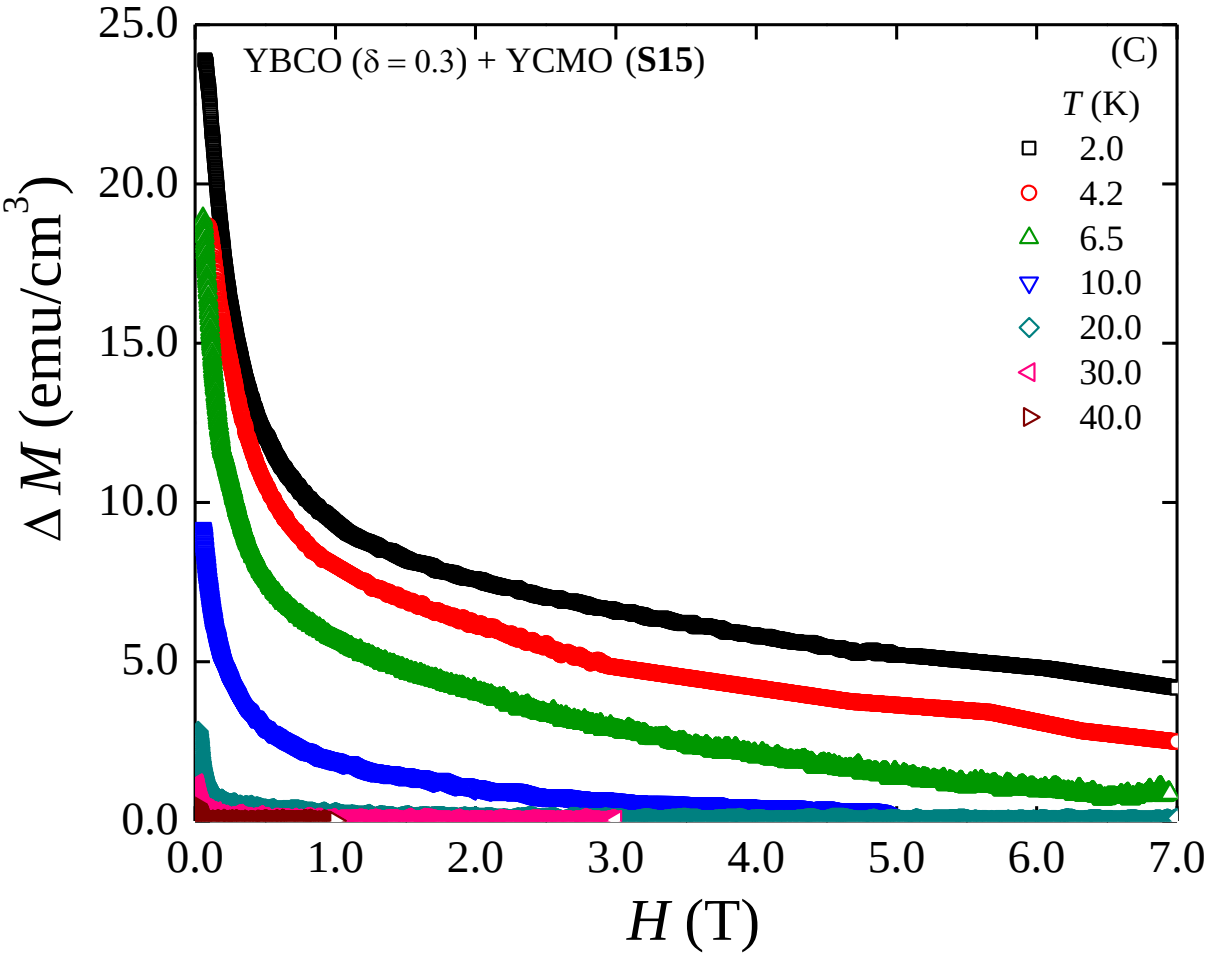

Figure 7.3(C): $\Delta M(H)$ of composite sample YBCO (δ = 0.3) + 5% YCMO (**S15**).

In **Figure 7.3(A-C)** we have plotted $\Delta M(H)$ at several T for three composite samples. In the vortex state, the maximum ΔM at low field limit at 2.0 K are 25.77 emu/cm^3, 15.62 emu/cm^3 and 23.90 emu/cm^3 corresponding to **S13**, **S14** and **S15** respectively. Both the oxygen vacancy landscape and magnetic particle landscape are both responsible for the lower limit of H. Because of the constant control of pinning by the magnetic profile, the actual pinning strength of the oxygen disorder profile is found to be oscillatory. Because the maximum ΔM of the pure

YBCO is 101.33 emu/cm^3 in the low field limit, for **S15** the difference (23.90 – 101.33) emu/cm^3 = – 77.43 emu/cm^3 is contributed by the magnetic pinning landscape solely. With the increasing field for H = 6.75 T the difference is (4.34 – 32.87) emu/cm^3 = – 28.53 emu/cm^3 reflecting the effect of the magnetic profile is changed by an order of magnitude.

In the inset of **Figure 7.3(A)** we have shown the irreversibility field, H_{irr} as a function of T for **S13**, **S14** and **S15** samples with YCMO. Clearly $H_{irr}(T)$ is sensitive to oxygen deficiency in presence of YCMO. However, $H_{irr}(T)$ shifts maximum for the highest oxygen disorder level (**S15**). A nonlinear variation of $H_{irr}(T)$ is visible in all three bulk samples as is observed for several other superconductors having mixed pinning landscapes. BZO added YBCO exhibits a similar change in $H_{irr}(T)$ in presence of two pinning landscapes **[3]**.

The J_{cm} is calculated as a function of H by using $\Delta M(H)$ and lateral dimensions **[20, 21]**. In **Figure 7.4(A-D)**, we have shown J_{cm} as a function of H in for several T for the pure YBCO (**S11**) and composite samples (**S13**, **S14** and **S15**) respectively. At low T = 2.0 K and low H ~ 0.16 T, J_{cm} ~ 1.8 × 10^5 A/cm^2 is found to be the highest for **S11**. Addition of YCMO in YBCO (**S15**) results in a strong suppression in the maximum J_{cm} in the low field and low T limit. The maximum J_{cm} observed in **S15** is ~ 4.1 × 10^4 A/cm^2 at 2.0 K and 0.1 T. Approximately, a 4.4 fold reduction in J_{cm} at the low H and T is observed. At low

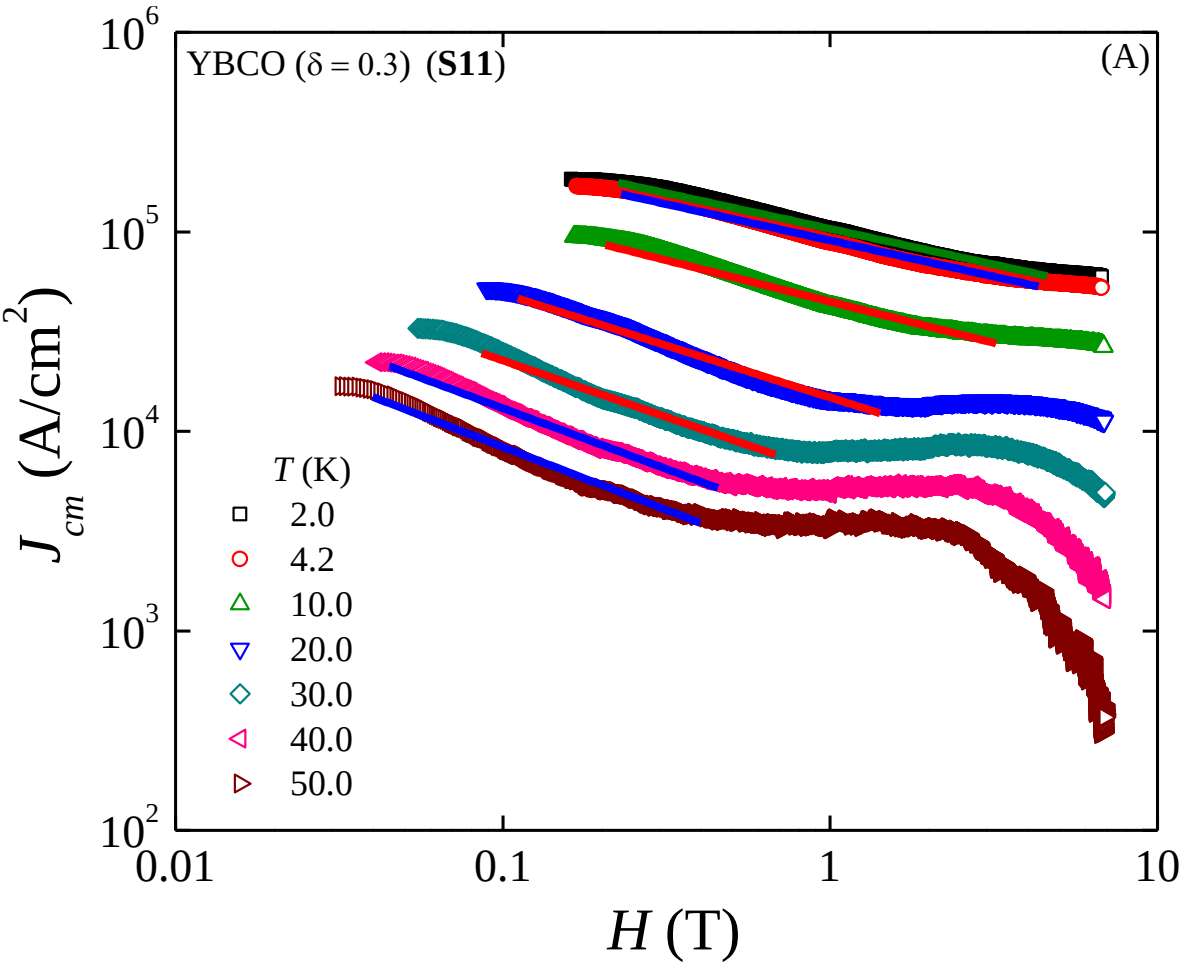

Figure 7.4 (A): Variations of $J_{cm}(H)$ in *log-log* scale at several T. Solid lines are fitting in the intermediate ranges of field. Slopes of the fitting lines in the form of eqn **7.1**.

T (2.0 K) and high field (~ 6.75 T) limit the reduction is found to be ~ 8.0 fold. The reduction in J_{cm} in **S15** sample in comparison to that of **S11** is caused by the addition of YCMO. Therefore, the reduction is associated with the weakening of pinning by the magnetic pinning landscape. With the increase in field the magnetic pinning profile becomes more effective in reducing the J_{cm}. On the contrary, in presence of nonmagnetic and non-superconducting nanoparticles, the

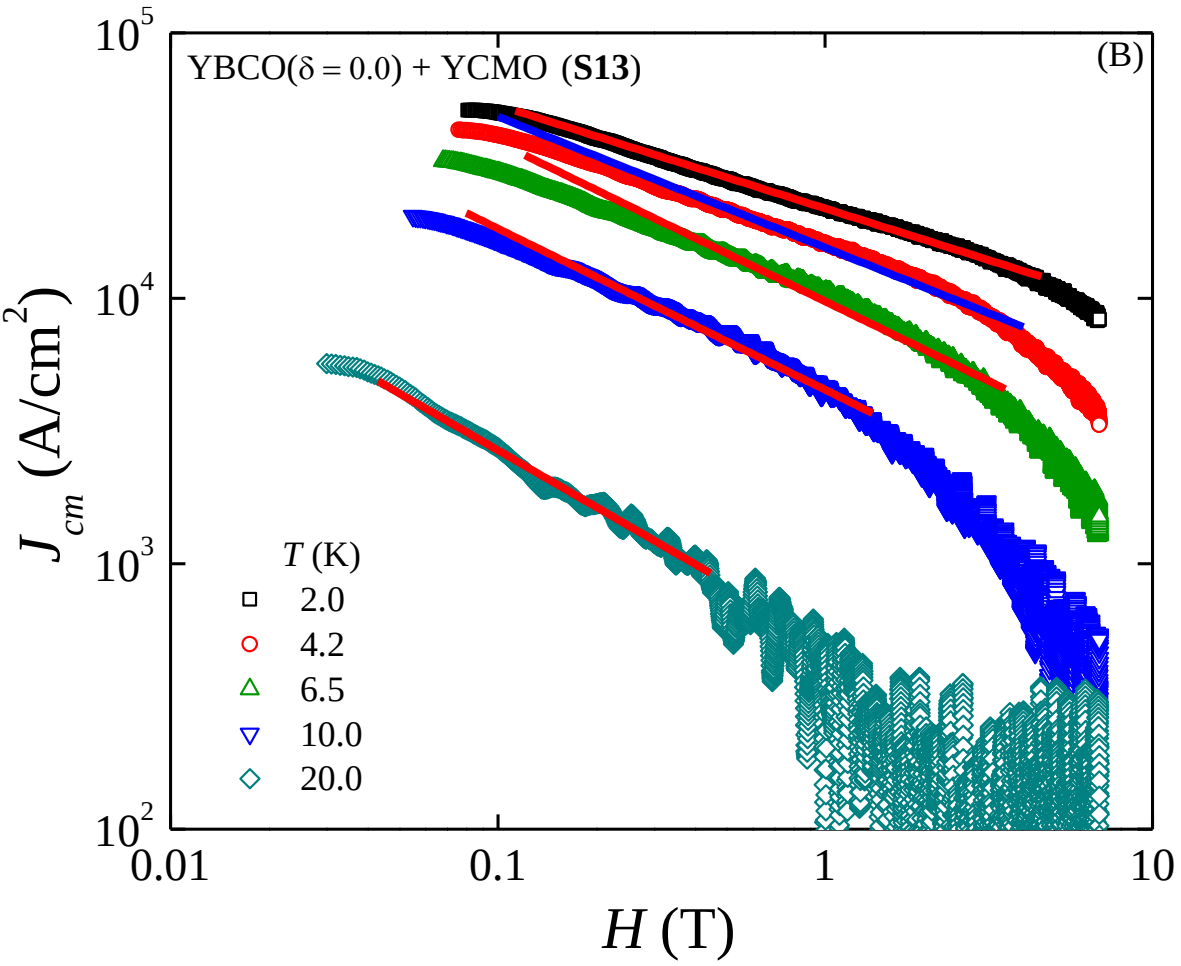

Figure 7.4 (B): Variations of $J_{cm}(H)$ in *log-log* scale at several T. Solid lines are fitting in the intermediate ranges of field. Slopes of the fitting lines in the form of eqn **7.1**.

enhancement of transport critical current density in YBCO thin film has also been observed at a high field at 77.0 K **[22]**.

Comparing J_{cm} of **S13**, **S14** and **S15** at (i) low T and low field and (ii) low T and high field we have made an attempt to quantify how oxygen disorder induced pinning profile acts as a pinning landscape (for fixed magnetic pinning

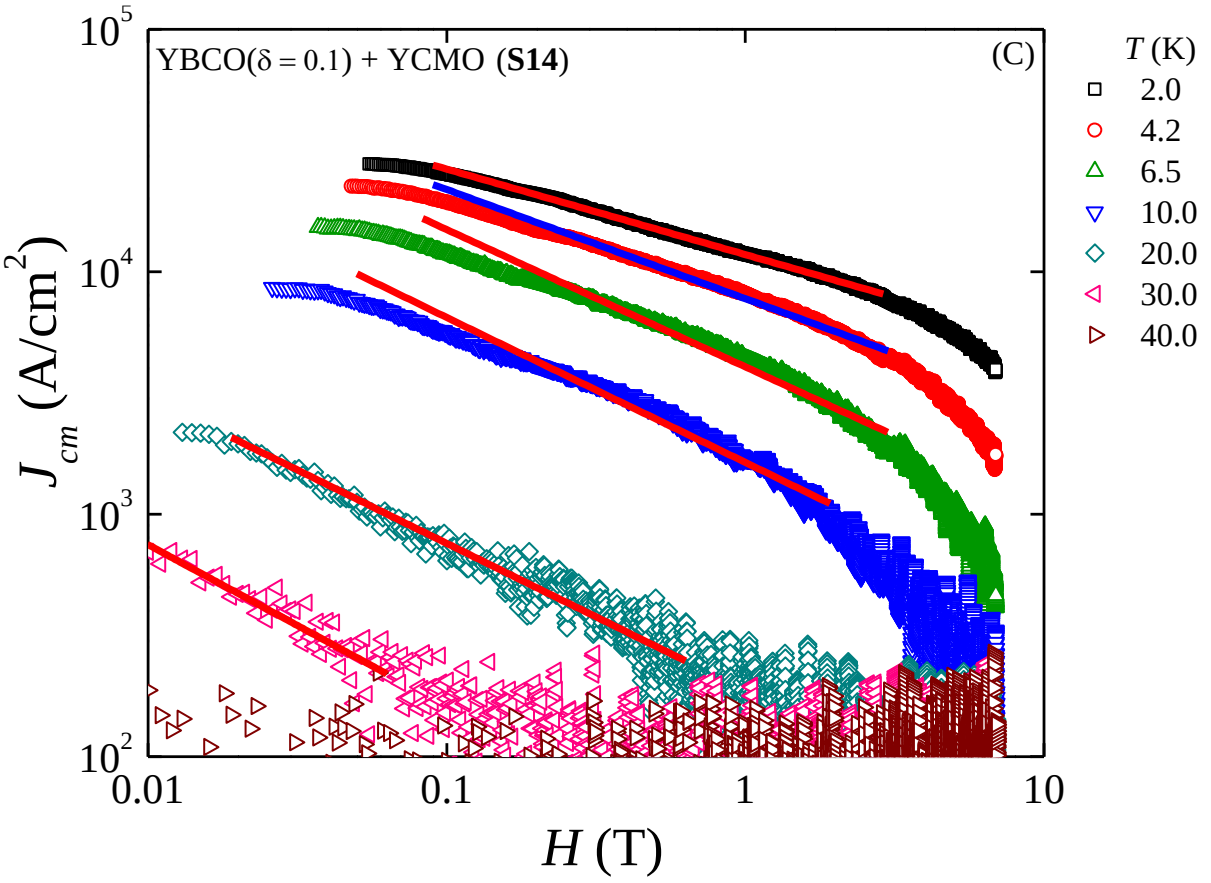

Figure 7.4 (C): Variations of $J_{cm}(H)$ in *log-log* scale at several T. Solid lines are fitting in the intermediate ranges of field. Slopes of the fitting lines in the form of eqn **7.1**.

landscape). At low T = 2.0 K and low field limit maximum J_{cm}s are 5.1 × 10^4 A/cm^2, 2.78 × 10^4 A/cm^2 and 4.13 × 10^4 A/cm^2 for **S13**, **S14** and **S15** respectively. As H is increased at 2.0 K, the high field (6.75 T) J_{cm}s are found to be 8.65 × 10^3 A/cm^2, 4.12 × 10^3 A/cm^2 and 7.5 × 10^3 A/cm^2 for **S13**, **S14** and **S15** respectively. Clearly, with the increase in oxygen vacancy level, J_{cm} exhibits an oscillatory behaviour. In oxygen deficient YBCO film, a reduction of critical current density indicates clearly weakening of pinning by oxygen disorders **[23]**. Therefore, the

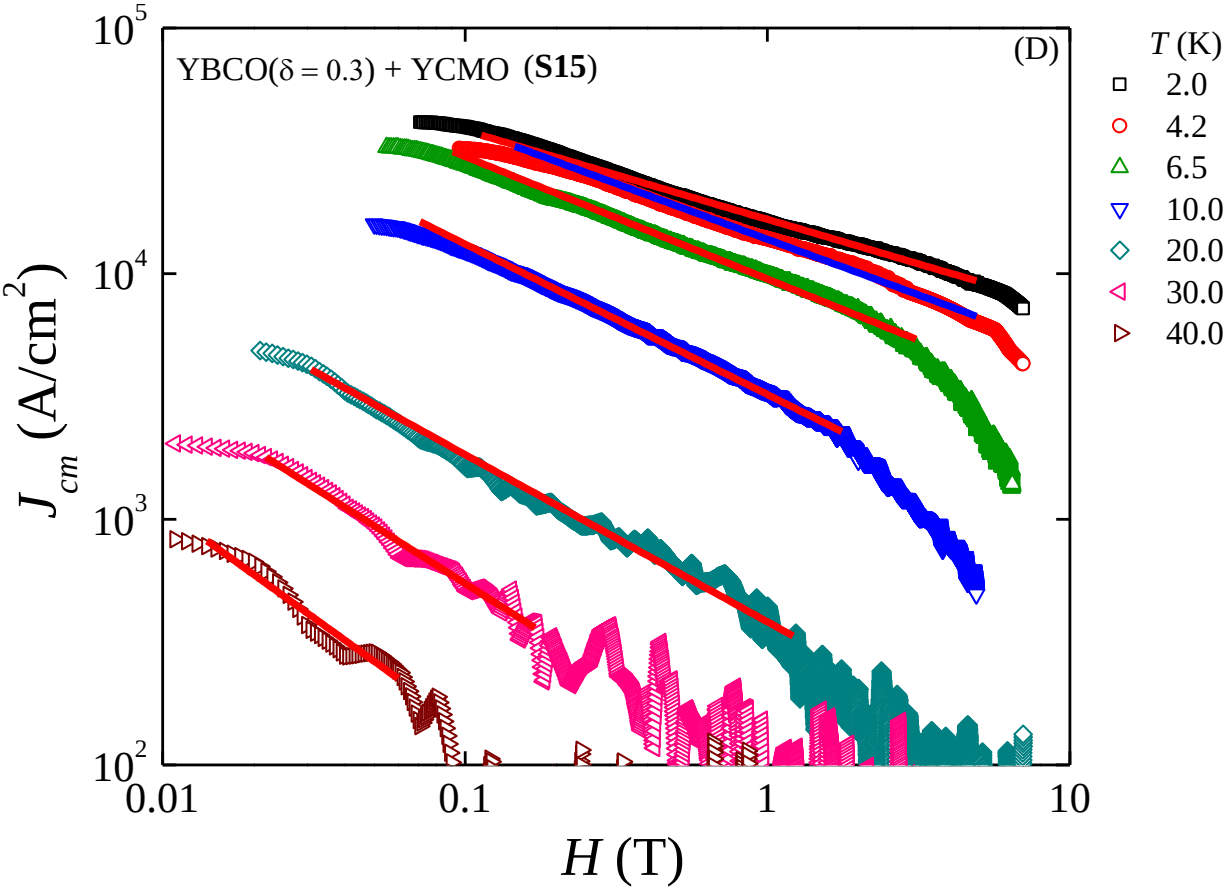

Figure 7.4 (D): Variations of $J_{cm}(H)$ in *log-log* scale at several T. Solid lines are fitting in the intermediate ranges of field. Slopes of the fitting lines in the form of eqn **7.1**.

pinning landscape induced by the distribution and level of oxygen vacancy may both increase or decrease depending on the nature of formed landscape at a particular external experimental condition.

Following a power law equation

$$J_{cm} \propto H^{-\alpha,} \qquad \textbf{(7.1)}$$

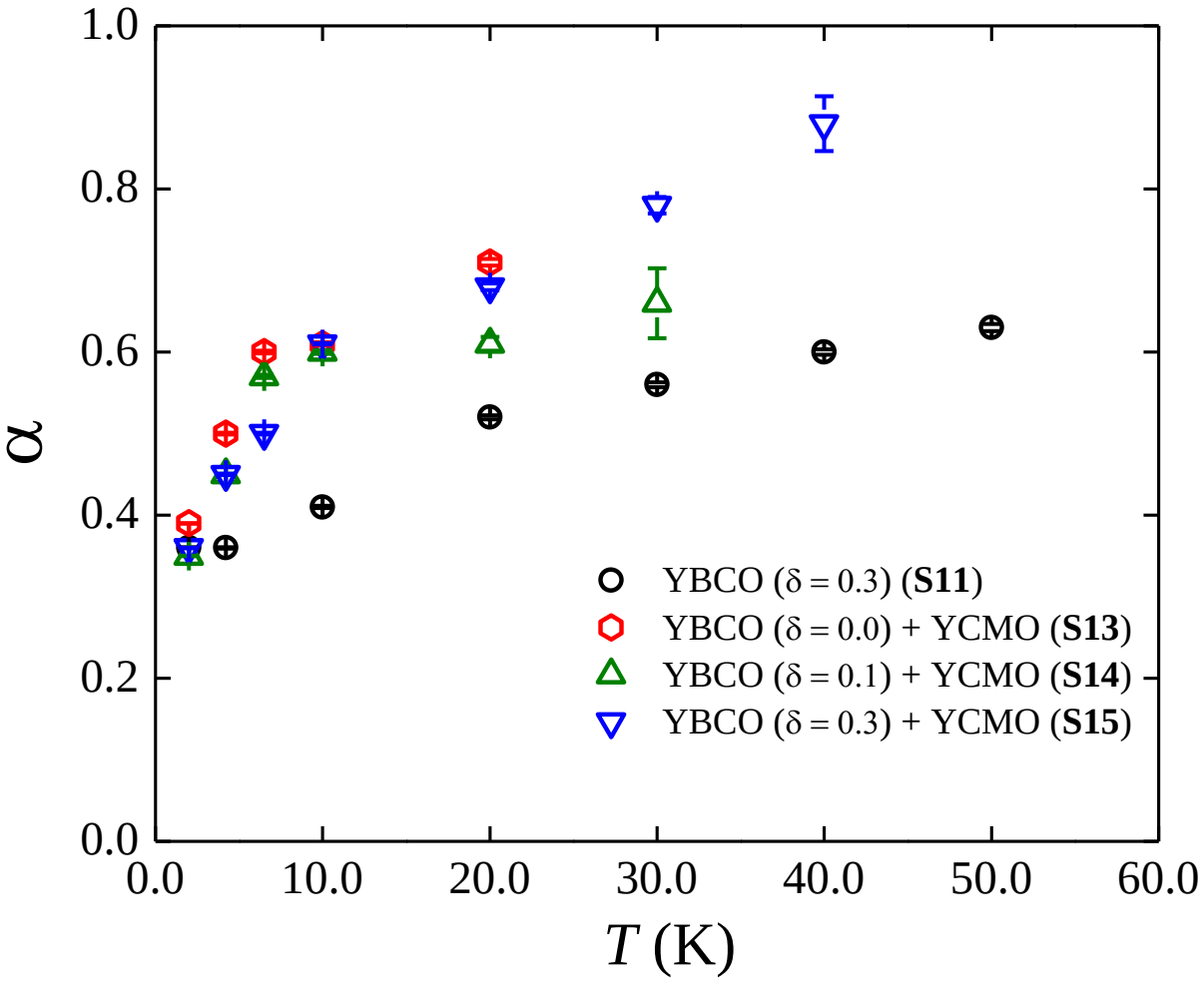

Figure 7.5: Variations of exponent, α as a function of *T* for **S11**, **S13**, **S14** and **S15**.

we have plotted $J_{cm}(H)$ in *log-log* scale and fitted to extract the exponent, α, as a function of *T*. In **Figure 7.5**, we have shown variation of α(*T*) for all samples. For the **S11**, α varies within a range of ~ 0.35 to 0.60 whereas, for other samples, **S13** and **S14**, α increase weakly with respect to that of the **S11**. However, with the increase in the level of oxygen disorder (δ) no systematic change α (*T*) has been observed. Interestingly we have observed that α = 0.9 at 40.0 K for **S15**. An

increase in α by the magnetic pinning landscape has been observed (**S15** and **S11**). It reveals that YCMO pinning landscape induces an enhanced rate of decrease in J_{cm} with H in the pure YBCO. In YBCO thin film, it is reported that with the increase in the natural linear defects, the exponent increases and remains in the range ~ 0.8 to 1.1 **[24]**. Therefore, the role of the line defects in controlling pinning is comparable to that induced by the magnetic pinning profile induced by YCMO in the intermediate range of the applied H.

7.4 Summary

Pinning landscapes generated by (i) oxygen vacancies and (ii) distribution of magnetic particles are not effective additively in controlling vortex pinning in YBCO. At low temperature limits the magnetic pinning profile strongly reduces the magnetic critical current density of YBCO in both low and high field limits but unevenly. However, the oxygen disorder induced pinning landscape may increase or decrease J_{cm} moderately depending on the level and distribution of the disorder in all fields at low T. An increase in the exponent by magnetic pinning landscape has been observed.

From the *IV* studies, we have shown a drastic change (shown in **Figure 4.6(B)**) in the SPS as a result of the inclusion of YCMO as discussed in **Chapter 4**. J_{cm} as discussed in **Chapter 7** also exhibits a strong reduction (shown in **Figure**

7.4(A-D)) in YCMO added YBCO. It indicates that the magnetic structure of the inclusion affects both the SPS and J_{cm}. However, more such systems will be necessary to understand how optimisation of the SPS is necessary in addition to the pinning landscape in YBCO for maximising $J_{cm.}$ Also, the behaviour of the SPS is the magnetic field will be an important aspect because we need to maximise J_{cm} in the high magnetic field.

7.5 Possible future directions

IV characteristics at zero magnetic field are very efficient to detect the BKT vortices. Controlling the distribution of the vortex-antivortex pairs from either by (i) carrier concentration or (ii) granularity can be an important starting point to find avenues for maximising vortex pinning and critical current density in the high magnetic field. A suitable relation between the SPS and J_{cm} may be possible after following the studies carried out in this thesis. It will be necessary to select several representative combinations of superconducting samples and pinning particles in different sites for which nonlinear *IV* down to very low temperature becomes prominent. Extension of *IV* measurements in magnetic field and $M(H)$ of such hybrid systems will be helpful in developing a suitable relation between the SPS and J_{cm} in future. Also, a generalization of the pinning of different vortex states in such systems will be another future direction based on this thesis.

7.6 References

[1] A. Koshelev, A. B. Kolton, Phys. Rev. B **84** (2011) 104528.

[2] G. Blatter, M. V. Feigel'man, V. B. Geshkenbein, A. I. Larkin, V. M. Vinokur, Rev. Mod. Phys. **66** (1994) 1125.

[3] M. Miura, B. Maiorov, S. A. Baily, N. Haberkorn, J. O. Willis, K. Marken, T. Izumi, Y. Shiohara, L. Civale, Phys. Rev. B **83** (2011) 184519.

[4] N. Haberkorn, M. Miura, J. Baca, B. Maiorov, I. Usov, P. Dowden, S. R. Foltyn, T. G. Holesinger, J. O. Willis, K. R. Marken, T. Izumi, Y. Shiohara, L. Civale, Phys. Rev. B **85** (2012) 174504.

[5] L. Civale, A. D. Marwick, T. K. Worthington, M. A. Kirk, J. R. Thompson, L. Krusin-Elbaum, Y. Sun, J. R. Clem, F. Holtzberg, Phys. Rev. Lett. **67** (1991) 648.

[6] Th. Schuster, M. R. Koblischka, H. Kuhn, H. Kronmüller, M. Leghissa, W. Gerhäuser, G. Saemann-Ischenko, H. W. Neumüller, S. Klaumünzer, Phys. Rev. B **46** (1992) 8496.

[7] E. Mezzetti, S. Colombo, R. Gerbaldo, G. Ghigo, L. Gozzelino, B. Minetti, R. Cherubini, Phys. Rev. B **54** (1996) 3633.

[8] A. E. Koshelev, I. A. Sadovskyy, C. L. Phillips, A. Glatz, Phys. Rev. B **93** (2016) 060508(R).

[9] M. G. Blamire, R. B. Dinner, S. C. Wimbush, J. L. MacManus-Driscoll, Supercond. Sci. Technol. **22** (2009) 025017.

[10] W. K. Kwok, U. Welp, A. Glatz, A. E. Koshelev, K. J. Kihlstrom, G. W Crabtree, Rep. Prog. Phys. **79** (2016) 116501.

[11] B. Maiorov, S. A. Baily, H. Zhou, O. Ugurlu, J. A. Kennison, P. C. Dowden, T. G. Holesinger, S. R. Foltyn, L. Civale, Nat. Mater. **8** (2009) 398.

[12] B. Maiorov, T. Katase, I. O. Usov, M. Weigand, L. Civale, H. Hiramatsu, H. Hosono, Phy. Rev. B **86** (2012) 094513.

[13] M. M. Doria, A. R. De C. Romaguera, M. V. Milošević , F. M. Peeters, Euro Phys. Lett. **79** (2007) 47006.

[14] A. Snezhko, T. Prozorov, R. Prozorov, Phys. Rev. B **71** (2005) 024527.

[15] T. Sk, D. Rakshit, A. K. Ghosh, Phys. Scr. **97** (2022) 025704.

[16] S. Haldar, A. K. Ghosh, Solid State Commun. **347** (2022) 114716.

[17] P. Mandal, D. Rakshit, T. Sk, A. K. Ghosh, J. Supercond. Nov. Magn. **35** (2022) 1079.

[18] D. Rakshit, T. Sk, P. Das, S. Haldar, A. K. Ghosh, Physica C **588** (2021) 1353909.

[19] T. Sk, A. K. Ghosh, J. Low Temp. Phys. **198** (2020) 224.

[20] C. P. Bean, Rev. Mod. Phys. **36** (1964) 31.

[21] S. Salem-Sugui, Jr., P. V. Lopes, M. P. Kern, S. Sundar, Z. Liu, S. Li, H. Luo, L. Ghivelder, Phys. Rev. B **102** (2020) 064509.

[22] T. Haugan, P. N. Barnes, R. Wheeler, F. Meisenkothen, M. Sumption, Nature **430** (2004) 869.

[23] R. Feenstra, D. K. Christen, C. E. Klabunde, J. D. Budai, Phys. Rev. B **45** (1992) 7555.

[24] F. C. Klaassen, G. Doornbos, J. M. Huijbregtse, R. C. F. van der Geest, B. Dam, R. Griessen, Phys. Rev. B **64** (2001) 184523.